Assessment of Windows on Noise Intrusion, Energy Efficiency, and Indoor Air Quality for Residential Buildings near Airports

PARTNER Project 26 Final Report

prepared by
Kai Ming Li, J Stuart Bolton, Qingyan Chen

June 2012

Assessment of Windows on Noise Intrusion, Energy Efficiency, and Indoor Air Quality for Residential Buildings near Airports

PARTNER Project 26 Final Report

Kai Ming Li, J Stuart Bolton, and Qingyan Chen

PARTNER-COE-2012-004

June 2012

Any opinions, findings, and conclusions or recommendations expressed in this material are those of the authors and do not necessarily reflect the views of the FAA, NASA, Transport Canada, the U.S. Department of Defense, or the U.S. Environmental Protection Agency

The Partnership for AiR Transportation Noise and Emissions Reduction — PARTNER — is a cooperative aviation research organization, and an FAA/NASA/Transport Canada-sponsored Center of Excellence. PARTNER fosters breakthrough technological, operational, policy, and workforce advances for the betterment of mobility, economy, national security, and the environment. The organization's operational headquarters is at the Massachusetts Institute of Technology.

The Partnership for AiR Transportation Noise and Emissions Reduction
Massachusetts Institute of Technology, 77 Massachusetts Avenue, 37-395
Cambridge, MA 02139 USA
http://www.partner.aero

Assessment of Windows on Noise Intrusion, Energy Efficiency, and Indoor Air Quality for Residential Buildings near Airports

Co-Principal Investigators:

Kai Ming Li, J Stuart Bolton and Qingyan Chen

Ray W. Herrick Laboratories, School of Mechanical Engineering

Purdue University, 140 South Martin Jischke Drive, IN 47907-2031

June 2012

1

Table of Contents

List of Figures

2.5 is used here.

different thicknessess of airspace.

List of Tables

Acknowledgments

Executive Summary

Two themes are explored in the current study. Theme I, which has three parts, is a study of various issues of noise ingression through windows in residential buildings. Theme II consists of two parts. It focuses on the energy efficiency and the associated effect on indoor air quality (IAQ) as a result of using sound-insulating windows.

Part 1 of Theme I discusses a study on the transmission of low-frequency noise (LFN) through an elastic structure—a single-pane window. An accurate numerical model was developed to study the structural responses due to LFN below 200 Hz. There is a distinct advantage to developing a precise prediction model because it allows relevant studies to be conducted numerically, avoiding the need to perform tedious and expensive experimental measurements. Parametric studies were carried out to examine the effects of natural frequencies, fluid loading, and dimensions of elastic structures on the transmission of LFN. The results of numerical simulations suggested that the effects of fluid loading and elastic mounting conditions are important for computing the transmission of airborne excitations through windows, particularly for frequencies below 125 Hz.

Part 2 of Theme I is presented in Chapter 3. It is noted that windows typically comprise the weakest link in sound insulation among all the components of a building façade, thus making them suitable paths for transmission of LFN. Numerical and experimental investigations were conducted to examine a possible solution for reducing the ingress of LFN. The effect on sound transmission due to adding non-periodic stiffening elements to single-pane windows was explored. The contribution of elastic mounting to low-frequency noise transmission was also considered in the numerical model. The variable positioning of beam elements as a part of a stiffened panel configuration was investigated numerically. The numerical results showed that

the transmission loss (TL) of sound below 150 Hz can be increased by several dB through the careful use of stiffening elements, while resilient mounting generally decreases the TL of low-frequency sound through windows. In addition, experimental testing on elastically mounted panels showed that sound transmission at non-resonant frequencies was not dependent on mounting stiffness. However, the resonance modes of the vibration plate caused low TL in the resonance regions of the frequency spectrum.

Part 3 of Theme I describes the development of a numerical model for predicting the transmission of LFN through a double-pane window. This study was motivated by the need to develop a platform for the future development of an effective numerical scheme to assess the acoustic performance of dual-airflow windows. The numerical model was validated by comparison with published experimental data and numerical results obtained from other computation-intensive schemes. Parametric studies were carried out to examine the acoustic performance of double-pane windows. It was highlighted that the phenomenon of mass-air-mass resonance of a double-pane window can reduce sound transmission in the resonance region. There is a general increase in the TL of LFN for frequencies outside the resonance region. It was also confirmed numerically that a configuration of two windowpanes of identical thickness is to be avoided in a double-pane window because of the coincidence of the resonant frequencies of these panels, which can cause significant degradation of the acoustic performance. Use of a higher density fluid (e.g., carbon dioxide) in the sealed airspace of a double-pane window can reduce the TL for LFN, i.e. improve its acoustic performance.

Theme II deals with the potential use of dual-airflow windows for sound insulation, leading to energy conservation and improved IAQ. Ventilated windows hold great promise for conserving energy in buildings owing to their suitability for energy exchange. They also improve

IAQ because fresh outdoor air is introduced indoors by a supply fan, and indoor contaminants are expelled outdoors via a separate exhaust fan. The development of a network model based on the EnergyPlus program is discussed in Part 1 of Theme II. The network model, which evaluates heat transfer in a two-dimensional system, enables the calculation of the energy efficiency of airflow windows. Experiments were conducted to confirm that the modified EnergyPlus program can provide accurate predictions of the energy demand in a building with airflow windows. Using the program, numerical simulations were conducted in seven selected cities in the U.S. for the energy efficiency of dual-airflow windows. Each of these selected cities represented a different climate zone in the U.S. The results showed that the dual-airflow windows performed better in cold or very cold climate zones and that the potential for energy saving in hot and humid climate zones was limited.

Most residential buildings use infiltration to dilute contaminants in indoor spaces in order to minimize energy use. However, infiltration is inconsistent in terms of performance and may not be sufficient to maintain IAQ at an acceptable level. Mechanical ventilation is usually needed to meet the requirements of good IAQ and is commonly used in commercial construction. Part 2 of Theme II presents a study on a multi-zone airflow network model known as CONTAM. The model enabled the assessment of IAQ in residences using CO_2 concentration as an indicator. Infiltration, ventilation by bathroom/kitchen exhaust fans, ventilation through a supply-airflow window, and ventilation through a dual-airflow window were used in the numerical simulations. Measurement results showed that Infiltration and ventilation through an exhaust fan could not maintain acceptable IAQ. In contrast, ventilation using supply-airflow windows or dual-airflow windows was shown to achieve acceptable IAQ. Dual-airflow windows were more versatile than supply-airflow windows in terms of energy conservation and improved IAQ.

Finally, Fig. 1.1 shows a flow chart summarizing the themes described above. Their details, conclusions and suggestion of future work will be separately addressed in the following chapters.
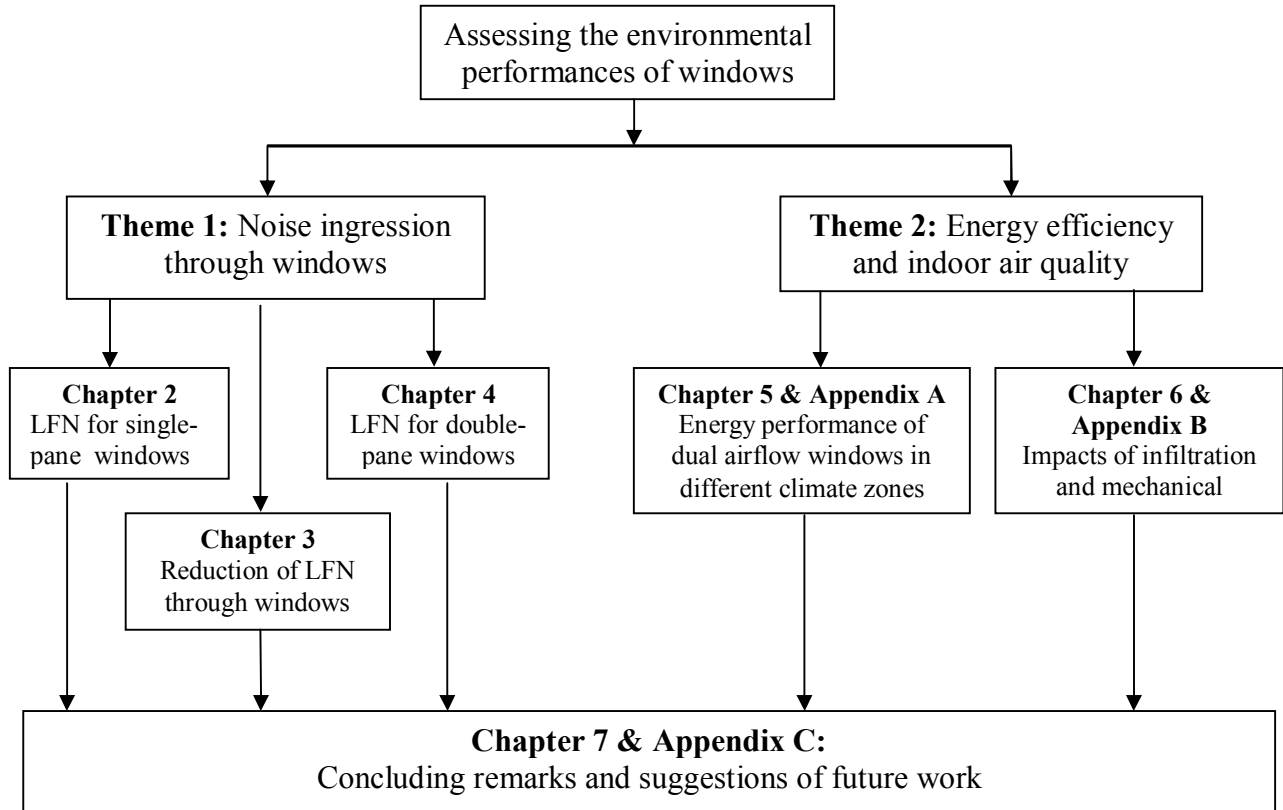
Fig. 1.1: Flow chart for the themes in the current study.

1. Background

The continuing increase in air traffic has implications for the preservation of our common resources and causes global and micro-environmental pollution. This pollution affects public health and causes damage to the prospects of future generations, particularly in residential communities near airports. Although the timely provision of resources and environmental mitigation measures could resolve some of these issues, others may require the fundamental re-consideration of the long-term sustainability of airport expansion plans. The benefits of sustainable development and its implementation in the design of residential buildings are important for the long-term growth of airports since a sustainable approach will reduce the adverse impact of aviation noise and emissions.

To reduce the adverse impact of noise intrusion into buildings near airports, the traditional approach has been to provide sound insulation, which effectively seals building envelopes. However, this method has a side effect, in that it degrades indoor air quality (IAQ), because most of these residential buildings obtain their fresh air by infiltration. With reduced infiltration, contaminant concentration and humidity within the buildings become higher. High humidity leads to a higher risk of condensation that can lead to other IAQ problems such as the growth of mold and bacteria. Although IAQ problems may be mitigated by using a mechanical ventilation system, such an action increases construction costs and subsequent energy use. However, increased sound insulation in buildings generally also improves thermal insulation and lowers the energy demand. Currently, many airport authorities have implemented a sound insulation program for residences located within the Community Noise Equivalent Level contour of 65 dBA.

Indeed, installing sound insulation in residential buildings impacted by airport noise is

one of the methods to implement Federal Aviation Administration (FAA)-approved noise compatibility programs. The FAA has published guidelines for carrying out noise insulation projects in the *Airport Improvement Program* (AIP) *Handbook* (U. S. Department of Transport, 2005) and its associated advisory circulars that provide periodic updates. In addition to the *AIP Handbook*, FAA provides further guidance in a document (DOT/FAA/PP-92-5) entitled "Guidelines for Sound Insulation of Residences Exposed to Aircraft Operations" (U.S. Department of Transport, 1992). This document was originally published in 1992 and was subsequently updated in 2005 by the US Navy for application at military airports (Ehrlich et al, 2005). An Airport Cooperative Research Program (ACRP) study was funded in 2010 to provide updates on the guidelines for FAA-approved noise insulation projects (Transportation Research Board, 2012). The focus of these documents is sound insulation and installation issues for the sound insulation of buildings near airports. Thermal and energy efficiency are not mentioned at all in these documents. On the other hand, IAQ is mentioned briefly in the context of being a concern. It is because sound insulation treatments will be compromised if windows and doors are opened.

The main goal of residential noise insulation programs is to reduce the impact of aircraft noise. Understandably, the treatments and products used in them reflect this primary goal of noise reduction, and the energy efficiency and IAQ of residential buildings are treated as secondary concerns. The problems of increased energy use and degraded IAQ resulting from noise reduction treatments are often left to program consultants to resolve in cooperation with local building officials. No further guidelines are provided for the important issues of IAQ and energy efficiency. The heavy emphasis on sound insulation and the secondary consideration of energy and IAQ have led to design solutions that are segmented and poorly integrated. The most

obvious example of this situation is that many FAA-funded noise insulation projects recommend the use of ducted air conditioning systems as the preferred method for insuring that the indoor environment remains comfortable for residents and occupants while doors and windows are kept closed, thus increasing energy use.

The problems with this approach are significant. First, ducted air ventilation systems are expensive to install, especially in retrofit situations. The quantity of resources required for these installations is often extensive. The costs of these ventilation systems typically represent 35%–50% of the total project expenditures for sound insulation treatments (Payne, 2010). Second, energy use after installing these ducted air ventilation systems is usually greater than the energy used prior to the installation of the sound insulation treatments. This situation becomes even more severe when air conditioning systems are installed in buildings where none previously existed. Third, since air conditioning is the preferred solution to the IAQ issue, there is often inadequate design consideration given to alternative solutions that may be less energy intensive and resource dependent.

The incompatibility of this solution is apparent when one considers that the windows and doors used in the program need to meet increasingly rigorous energy code requirements. The irony of insuring energy efficiency for one component of the sound insulation treatments (the windows) while creating increased energy usage for another component of the treatments (air quality) is striking, and it underscores the need for more holistic solutions to sound insulation.

It is of interest to note that the study of sound insulation for mid- to high-frequency noise in residential buildings has been studied widely (U.S. Department of Transportation, 1992). However, noise spectra from aircraft have substantial components below 150 Hz. Consequently, the responses to low-frequency noise (LFN) around windows are considered in the present study.

The impact of LFN is of particular concern owing to its pervasiveness, efficient propagation, and the low efficacy of many building components (e.g., walls) in its attenuation when compared with higher-frequency noise. In fact, LFN has many negative effects on health, behavior, sleep, task performance, and social attitudes (Broner, 1978). For these reasons, it is necessary to understand how windows respond to low-frequency sound. This is because, among many other structures, windows are usually a major transmission path for noise, particularly near their low-frequency resonances.

Two parallel themes are presented in the present study. Theme I is devoted to theoretical and experimental studies for the structural transmission of low-frequency noise through single- and double-pane windows. The issues of energy efficiency and IAQ from the installation of air-flow windows in residential buildings are addressed in the second theme. The AIP guidelines provide recommendations on current best practices for improving IAQ and reducing energy use while maintaining sufficient noise level reductions for the comfort of the occupants in residential buildings near airports. The outcomes of these studies will set a direction for providing additional information to complement the existing AIP guidelines.

This report includes three chapters dedicated to Theme I. Chapter 2 presents a study of the transmission of LFN through a single-pane window. The study describes a numerical formulation that combines the advantages of FEM with boundary integral formulation to allow the direct computation of sound fields behind an elastic plate mounted with different types of elastic supports. The numerical results were validated by comparison with published experimental data. A series of parametric studies was conducted to investigate the effects, on sound transmission through a single-pane window, caused by (a) fluid loadings, (b) the elastic support of the window frames, (c) the aspect ratio of the windows, and (d) the effect of damping.

The transmission of a broad band LFN was explored. Chapter 3 is the second part of Theme I in which a method is proposed to reduce the transmission of LFN through windows. Experiments were conducted in a reverberant chamber for the validation of the numerical predictions. The last part of Theme I is presented in Chapter 4, in which a theoretical model for predicting the transmission of LFN through a double-pane window was developed. This chapter aims to provide a platform for further studies examining the use double-pane and even triple-pane windows for reducing the ingress of aircraft noise into residential buildings near airports.

Theme II is divided into two parts, which are described in Chapters 5 and 6. Chapter 5 discusses a numerical model based on a modified EnergyPlus program. The numerical model was used to assess the energy efficiency of different windows installed in two typical residential buildings in different climate zones in the U.S. The second part of Theme II was dedicated to the study of IAQ in comparable residential buildings located in the same climate zones using infiltration and mechanical ventilation schemes. A simulation tool developed by the National Institute of Standards and Technology (NIST) was used to investigate the impact of infiltration and mechanical ventilation on IAQ. The effectiveness of infiltration for reducing indoor containment concentrations was addressed. The effects of supply-airflow windows and dual-airflow windows on IAQ were analyzed.

We reiterate that the aim of the present study is to investigate the environmental performance of windows because the windows in a residential building are often considered to be the weakest link in the sound insulation program. Our current efforts represent a step to achieve a holistic solution for providing sound insulation for residential buildings near airports. Chapter 7 offers some concluding remarks and suggestions for future work.

References

N. Broner, 1978. "The effects of low frequency noise on people-a review." *Journal of Sound and Vibration* **58**, 483-500.

G. Ehrlich, M. Burns, C. Morrow and A Stefanlw, 2005. "Guideline for sound insulation of residences exposed to aircraft operations," prepared for Department of Navy, U. S., by Wyle Research & Consulting, 2001 Jefferson Davis Highway, Suite 701, Arlington, VA 22202.

M. K. Payne, 2010. Private Communication. The Jones and Payne Group, Inc., 123 North Washington Street, Boston, MA 02114.

U. S. Department of Transport, 1992. "Guideline for sound insulation of residences exposed to aircraft operations," U.S. Department of Transport, DOT/FAA/PP-92-5.

U. S. Department of Transport, 2005. "Airport Improvement Program Handbook," Ch. 8, U.S. Department of Transport, Order 5100.38C.

2. The effects of fluid loading and elastic supports on the transmission of low-frequency noise through a single-pane window

2.1 Introduction

Generally speaking, the effects of wall mounting conditions are too significant to be neglected in the investigation of most structural acoustic problems. This is particularly the case for the study of the transmission loss (TL) of a finite panel at low frequencies as evidenced in the classical plot of the TL spectrum (Wilson, 1994) for the stiffness and resonance controlled regimes. Unfortunately, most of current theoretical models either simplify considerably the wall mounting conditions or neglect their effects altogether. Such an energy-based global method as the statistical energy analysis (SEA) is a notable exception in which complex mounting conditions can be incorporated in the model but SEA is only suitable for high frequency analyses (Craik, 1996).

In the past forty years, there are sustained interests in studying the response of an elastic structure subject to low-frequency acoustic excitations in a compressible fluid medium (Zienkiewciz et al, 1997; Wilton, 1978; Matthews, 1986; Everstine and Henderson, 1990; Jeans and Matthew, 1990; Kopuz et al, 1996; Wu, 2001; Li and Zhao, 2004). Thin plates of arbitrary shapes were often formulated in many previous works although there were some studies addressing the interaction of the fluid medium with a thin rectangular plate. For instance, Wu and Dandapani (1994) developed a multi-domain BEM to model the transmission of sound through thin elastic panels but the boundary supports were not included in their studies. Berry et al (1990) and Chiello et al (1999; 2003) considered the response of a baffled rectangular plate with arbitrary elastic boundary conditions but they assumed that the fluid loading due to air was

negligibly small.

By ignoring the effect of fluid loading, the excitation force due to incoming airborne sound waves and the vibration of the rectangular panel can be computed separately. The displacement of the elastic panel can be used to evaluate the radiated sound fields using the Rayleigh integral. The TL of the panel can then be calculated from the incoming sound waves and the radiated sound field. However, this assumption will be inadequate in the case when the acoustic excitations resonate with the vibrating panel coupled with the air loading. In such cases, the dynamics of the elastic structure and the acoustic pressure in the fluid medium must be solved simultaneously (Atalla and Bernhard, 1994).

Sgard et al (1994) presented a coupled FEM/BEM model to study the effects of mean flow on the response of a planar structure but they did not consider the influence of the elastic boundary mountings on the radiated sound fields in the fluid medium. Chiello et al (2000) investigated the effects of the elastic joints on the transmission of LFN in enclosures but the effect of fluid loadings was ignored in their analysis.

The aim of this chapter is to investigate the sound transmission behavior of low frequency noise (LFN) through a window. It is of particular interest to examine the acoustic excitations at frequencies below 125 Hz. It is because the response of a window depends on various physical parameters such as the fluid loading and the characteristics of mounting conditions, which are two important factors for the transmission of LFN through the windows. There is a need to examine the simultaneous effects of fluid loadings and elastic boundary conditions in the numerical analyses. To achieve these objectives, a classical method of combining a finite element (FEM) scheme with a boundary element (BEM) formulation is used. A component mode synthesis (CMS) technique (Atalla and Bernhard, 1994; Sgard et al 1994;

Craig, 1977) will be applied to include the elastic boundary conditions in the numerical model. This fully coupled FEM/BEM model provides an efficient model to evaluate the transmission of LFN through an elastic plate with visco-elastic supports.

The layout of the chapter is as follows. A brief outline of the numerical formulation is given in Sec. 2.2. Sec. 2.3 shows the validation of our numerical scheme by comparing the predicted results with those computed by a standard FEM scheme available commercially (ANSYS, 1992). In Sec. 2.4, a parametric study is presented which examines the effects of fluid loading, mounting conditions, dimensions, and damping of the elastic panel on the TL in the low frequency region. The effect of elastic boundary supports on the transmission of broadband LFN through a window has been exploited. In Sec. 2.5, the proposed numerical model is validated by comparing its predictions with published experimental data (Quirt, 1982). Finally, concluding remarks of this chapter are offered in Sec. 2.6.

2.2 Formulation of the problem

Suppose a rectangular window, which has a size of L_x by L_y and a uniform thickness of h, is mounted on an infinite rigid baffle, S as shown in Fig. 2.1. The baffled window is immersed in a light fluid medium and is subject to an acoustic excitation due a point source (or an incident plane wave) in the source medium V_1. The receiver is located at the receiver medium V_2 of an otherwise quiescence environment. A Cartesian coordinate system (x, y, z) is chosen such that the surface S separate V_1 from V_2 at the $z = 0$ plane. We denote the upper surface in contact with V_1 as S_1 and the lower surface S_2 which associates with V_2.
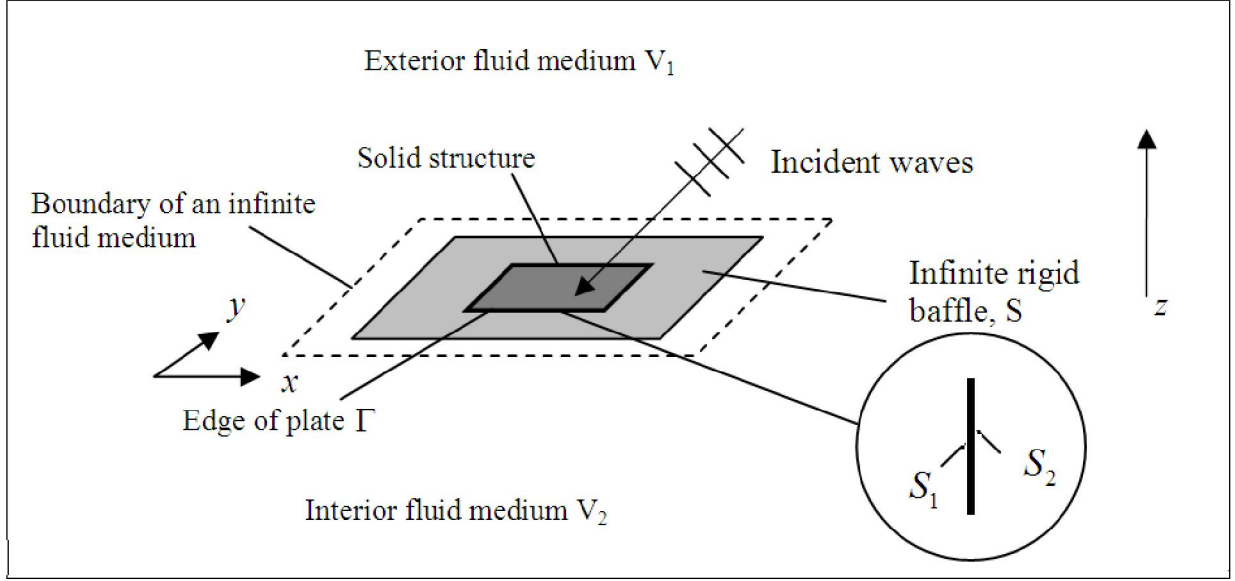
Fig. 2.1. Geometrical configuration of the problem.

The window is subjected to a low-frequency harmonic excitation of angular frequency, ω. We further assume that the window can be treated as an elastic plate with classical thin plate theory. The shear behavior of the window is ignored and not considered in the present study, i.e. the airborne sound waves only induce pure bending vibrations.

The window is now discretized into a number of rectangular elements with the number of divisions of M and N along x and y directions, respectively. We designate the nodes as the connections between adjacent elements of the rectangular plate: each element has 4 nodes. Hence, there are $M \times N$ pieces of identical rectangular elements in bending and $(M + 1) \times (N + 1)$ nodes joining all elements together. Each small finite element has a size $a \times b$ where

$$a = L_x/M \quad \text{and} \quad b = L_y/N .$$ (2.1)

The dimensions for a and b are chosen such that they are less than one-tenth of the wavelength of the highest frequency used in the numerical analysis. For instance, 16×16 elements are used in

our numerical analysis to calculate the transmission loss of a 1 m × 1 m square panel for an incident wave with the maximum frequency of about 500 Hz. A total of 256 elements is used in the numerical computation where each element has a size of 6.25 cm × 6.25 cm.

In order to apply the technique of the component mode synthesis for a FEM formulation, the window is decomposed into plate substructures and the edges with elastic supports. The plate substructures are characterized by the stiffness, mass and damping matrices $\mathbf{K}$, $\bar{\mathbf{M}}$ and $\mathbf{D}$. Each of the elastic supports is characterized by a *null* mass matrix, a *null* damping matrix and a stiffness matrix $\mathbf{S}$ at the nodal points along the edges, Γ.

The stiffness matrix for each elastic support at Γ can be expressed in terms of a diagonal matrix as follows:

$$\mathbf{S} = \begin{bmatrix} \alpha S_t & 0 & 0 \\ 0 & \alpha S_\theta & 0 \\ 0 & 0 & \alpha S_\phi \end{bmatrix}, \tag{2.2}$$

where S_t is the total translational stiffness along edges of the window (with unit dimension of N m^{-1}). The variables, S_θ and S_ϕ, are the total stiffness along edges of the window (with unit dimension of N m rad^{-1}) that resist rotational motions in the *x*- and *y*-directions respectively. For simplicity, we assume that the translational and rotational restrains along the edges are uniform, i.e.

$$\alpha = \begin{cases} a/l & \text{for elements in the horizontal edges} \\ b/l & \text{for elements in the vertical edges} \end{cases}. \tag{2.3}$$

where l [$= 2 (L_x + L_y)$], is the total length of the supporting edges.

Applying *Hamilton's principle* (see, for example, Sodel 1993), it is possible to obtain a global matrix equation for the deflection of all elastic elements in the window structure,

$$\{\mathbf{d}\}^{\mathrm{T}} = (ab) \times \{\mathfrak{R}\}\big[\{\mathbf{C}\} + \{\mathbf{S}\}\big]^{-1} \times \{\mathbf{T}\} \times \{\mathbf{\Delta P}\}^{\mathrm{T}} . \tag{2.4}$$

where the global matrix $\{\mathbf{d}\}$ is its central displacement vector, the superscript T represent the transpose of a matrix, $\{\mathbf{\Delta P}\}$ is the vector for the difference in the pressures acting centrally on all elements of S_1 and S_2, $\{\mathfrak{R}\}$ is a global transformation matrix converting the nodal displacement vectors to the corresponding central displacement vectors, and $\{\mathbf{T}\}$ is a global transformation matrix converting centrally loaded pressure forces to the corresponding nodal forces. In Eq. (2.4), the matrices $\{\mathbf{C}\}$ and $\{\mathbf{S}\}$ are given, respectively, by

$$\{\mathbf{C}\} = -\omega^2 \{\overline{\mathbf{M}}\} + i\omega \{\mathbf{D}\} + \{\mathbf{K}\} , \tag{2.5}$$

and

$$\{\mathbf{S}\} = \begin{bmatrix} \mathbf{S_1} & 0 & \cdots & 0 \\ 0 & \mathbf{S_2} & \cdots & 0 \\ \vdots & \vdots & \cdots & \vdots \\ 0 & 0 & \cdots & \mathbf{S_L} \end{bmatrix} , \tag{2.6}$$

where the diagonal element, $\mathbf{S_i}$, is given by Eq. (2.2) if the nodal points coincide with the edges of the window, otherwise, $\mathbf{S_i} = 0$ for all other nodal points not in contact with the edges of the window. The global matrix $\{\mathbf{S}\}$ is used to characterize the elastic supports at Γ. In Eq. (2.4), $\{\overline{\mathbf{M}}\}$, $\{\mathbf{D}\}$, and $\{\mathbf{K}\}$ denote the respective global matrices for the mass, damping, and stiffness of the rectangular plate element (Przemieniecki, 1985). The damping factor can be written in terms of the stiffness of the plate as

$$\{\mathbf{D}\} = (2\eta / B)\{\mathbf{K}\} , \tag{2.7}$$

where B and η are the bending stiffness and damping ratio of the plate respectively. Unless

stated otherwise, η is set as zero in the following numerical simulations.

The FEM formulation can be used conveniently for treating structural problems as described above. In the case of calculating the pressure field in an unbounded medium, the BEM formulation is preferred because it satisfies the Sommerfeld radiation condition naturally without the need of introducing an artificial boundary that is required by the FEM formulation.

Discretization of the boundary S_1 or S_2 means dividing it into smaller pieces of the *boundary elements*. A small rectangular panel is used to represent each element and the panels employed in the boundary integral equations coincide with that used in the finite element equations. In the present study, a weakly singular representation (Koo et al 1996) of the pressure field is used to eliminate the discontinuity of pressure in the vicinity of rectangular panels. The pressure radiating from the vibration of the window can then be written in terms of the global displacement and pressure matrices as follows:

$$\{\mathbf{P}_1\}^{\mathrm{T}} = \{\mathbf{P}_0\}^{\mathrm{T}} + \{\mathbf{A}\}\{\mathbf{d}\}^{\mathrm{T}}, \tag{2.8a}$$

$$\{\mathbf{P}_2\}^{\mathrm{T}} = -\{\mathbf{A}\}\{\mathbf{d}\}^{\mathrm{T}}, \tag{2.8b}$$

where $\{\mathbf{P}_1\}$ and $\{\mathbf{P}_2\}$ are the pressure vectors on the surfaces, S_1 or S_2, respectively, the vector $\{\mathbf{P}_0\}$ is the pressure acting at the center of the element due to the point source or plane waves.

In Eqs. (2.8a) and (2.8b), $\{\mathbf{A}\}$ is a square matrix which is formed by the process of collocation. The mutual interaction between central points of all elements on the upper (or lower) surface of the window can be determined according to

$$\mathbf{A}(l,m) := (1/Q_0)\rho_0\omega^2 \int_S G(\mathbf{x}_l|\xi_m)\mathrm{d}S, \tag{2.9}$$

where $\mathbf{A}(l,m)$ is referred as the lth *collocation point* on the center of the mth element of the plate

in $\{\mathbf{A}\}$, the parameter, Q_0, which can be treated as the source strength of the incoming sound waves, can be set as 1 N m^{-1} for convenience. The corresponding Green's function $G\left(\mathbf{x}_l\middle|\xi_m\right)$, is given by (Seybert and Wu, 1989)

$$G\left(\mathbf{x}_l\middle|\xi_m\right) = \frac{e^{ikR_1}}{4\pi R_1} + \frac{e^{ikR_2}}{4\pi R_2} \quad , \tag{2.10}$$

where R_1 and R_2 are the respective distances from the sound source and its imaginary source to the receiver, see Fig. 2.2 for the schematic diagram. There is an apparent singularity in $G\left(\mathbf{x}_l\middle|\xi_m\right)$ when $\mathbf{x}_l = \xi_m$. However, this singularity can be removed straightforwardly by using the method suggested by Hwang (1997).
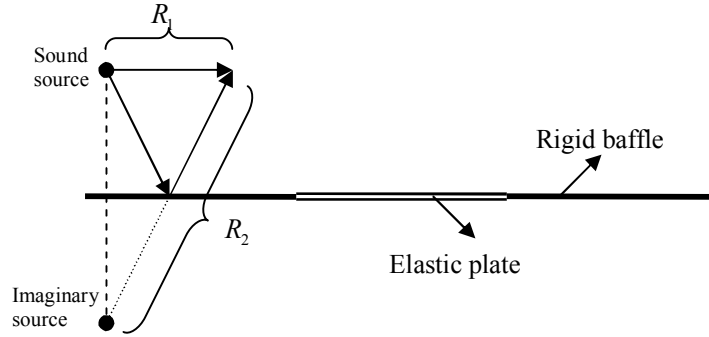
Fig. 2.2. The mirror effect of the baffle.

Combining Eqs. (2.8a) and (2.8b), we can obtain another set of matrix equations relating the net pressure, $\{\Delta \mathbf{P}\}$, with the displacement vectors on the window as follows:

$$\{\Delta\mathbf{P}\}^{\mathrm{T}} = \{\mathbf{P}_1\}^{\mathrm{T}} - \{\mathbf{P}_2\}^{\mathrm{T}} = \{\mathbf{P}_0\}^{T} + 2\{\mathbf{A}\}\{\mathbf{d}\}^{\mathrm{T}} \quad . \tag{2.11}$$

Expressions (2.4) and (2.11) are the coupled matrix equations that can be solved simultaneously for $\{\mathbf{d}\}$ and $\{\Delta\mathbf{P}\}$. We could eliminate $\{\mathbf{d}\}$ in favor of $\{\Delta\mathbf{P}\}$ that lead to the so-called fluid variable methodology (Wilton, 1978; Matthews, 1986). In this paper, the structural variable

methodology (Zienkiewciz et al, 1997; Matthews, 1986) is used by substituting Eq. (2.11) into Eq. (2.4). This leads to a matrix solution for $\{\mathbf{d}\}$ as follows:

$$\{\mathbf{d}\}^T = \left[\mathbf{I} - 2\{\mathbf{H}\}\{\mathbf{A}\}\right]^{-1} \times \{\mathbf{H}\}\{\mathbf{P}_0\}^T,$$ (2.12)

where

$$\{\mathbf{H}\} = (ab) \times \{\mathfrak{R}\}\left[\{\mathbf{C}\} + \{\mathbf{S}\}\right]^{-1} \times \{\mathbf{T}\}.$$ (2.13)

The displacement vector, $\{\mathbf{d}\}$, can then be used in Eqs. (2.9) and (2.10) to calculate the respective pressures, $\{\mathbf{P}_1\}$ and $\{\mathbf{P}_2\}$ on the surfaces, S_1 and S_2, of the window.

From the system of equations described above, the sound fields in front of and behind a window can be determined. With knowledge of the sound pressure at every element, it is possible to evaluate the sound power on both sides of a window. The sound power of the incident waves on the window can be calculated by

$$W_I = (ab) \times \sum_{q=1}^{M \times N} \left(\left[\mathbf{P}_0(\mathbf{x}_q)\right]^2 \Big/ 2\rho_0 c_0\right),$$ (2.14)

where c_0 is the sound speed of the fluid medium. The sound power, W_T, radiated from the vibrating window at the lower surface can be estimated by

$$W_T = (ab) \times \sum_{q=1}^{M \times N} \mathrm{Re}\left\{\mathbf{P}_2(\mathbf{x}_q)\left[-i\omega\, \mathbf{d}(\mathbf{x}_q)\right]^*\right\},$$ (2.15)

where the superscript * represents the conjugate of the complex parameter. The sound transmission loss (TL) of the window at a single frequency can then be calculated by using the following definition (Kinsler et al; 2000),

$$\mathrm{TL} = 10\log_{10}\left(\frac{W_I}{W_T}\right).$$ (2.16a)

Equation 2.16a shows that the overall transmission loss of the window for a given frequency range is defined as the ratio of the total incident sound power to the total radiated sound power where the total sound power is calculated by summing the contribution from all bands lying between the frequency range of interest.

Use of the coupled FEM/BEM model described above, it is possible to include the effect of fluid loadings on the prediction of the overall transmission loss of the window. The accuracy of our numerical model will be confirmed by comparing the numerical predictions with (i) those obtained by other numerical schemes, and, (ii) other published experimental data.

2.3 Validation of the coupled FEM/BEM model

The coupled FEM/BEM model developed in section 2.2 has been used to develop a set of MATLAB programs for calculating the sound TL of windows. To confirm the validity of the model, we compare the MATLAB numerical predictions with that predicted by a FEM model based on ANSYS (1992). We are primarily interested in the transmission of low frequency noise well below the co-incidence frequency. As a result, it is sufficient to consider the transmission loss of plane wave normally incident on the baffled elastic panel for the validation of our numerical scheme. In the numerical simulations presented, the Young's modulus, density and Poisson's ratio of the window are taken as 70.3 GPa, 2700 kg m^{-3} and 0.35 respectively which is standard for glass. The sound speed and density of air are taken as 344 m s^{-1} and 1.21 kg m^{-3} respectively which is standard for dry air at 20°C. Unless stated otherwise, the 5 mm thick window of dimensions 1 m $\times$ 1 m is used in the numerical simulations.

To set up an appropriate FEM model using ANSYS, the following points are noted. Since the pressures on both faces of the window are different, the use of a single layer of shell elements

with fluid structure interfaces on both sides is not recommended. If a single layer of shell elements is used, then each nodal point will have the same pressure on either side of the shell. An alternative is to define two separate layers of shells that coincide with each other. The degrees of freedom in the displacement of the two shells are coupled and the material properties of the shells are adjusted appropriately to represent a baffled window mounted on a rigid plane. The size of each element used in ANSYS and the coupled FEM/BEM model is the same: it is chosen to be at least one-tenth of the wavelength of the incident sound wave.

The three-dimensional acoustic fluid elements are used to model the fluid medium. The fluid-structure interfaces are flagged by surface loads at the fluid elements adjacent to the solid structures. The spring elements are used to model the condition of an elastic boundary. As discussed before, we have to introduce an artificial boundary that is required by the FEM modeling when we use acoustic fluid elements to model the fluid medium. The fluid media in front of and behind the window (V_1 and V_2) can be modeled as two large cavities filled with fluid. The cavities should be as large as possible. In the present study, the cavity volume of 10 m $\times$ 10 m $\times$ 10 m is found to be adequate to give accurate results. The sound fields at infinity can be simulated by setting the boundary surfaces of the specified cavity (10 m $\times$ 10 m $\times$ 10 m) as the perfectly absorptive materials, i.e the absorption coefficients of these surfaces are set as 1.

Figure 2.3 shows a comparison of the predicted results according to the coupled FEM/BEM model and FEM scheme. The frequency used in this and subsequent numerical simulations varies between one third octave bands of 9 and 560 Hz. A step of 1 Hz is used for the analysis of narrow band frequency and a linear interpolation is simply used to connect adjacent bands. Numerical results for one-third octave bands are obtained by integrating the corresponding results obtained from the narrow band analyses.

31
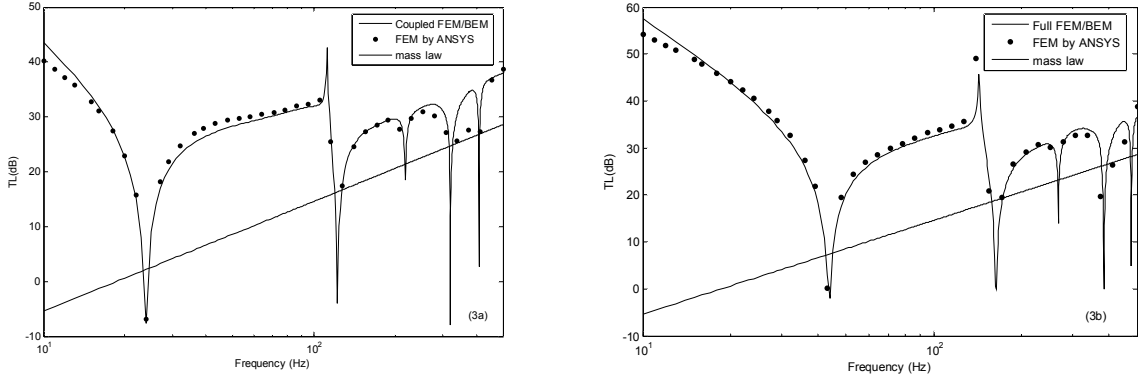
Fig. 2.3. Comparison of the transmission loss computed by the coupled FEM/BEM MATLAB model (–), numerical simulations based on FEM by ANSYS (•) and the mass law (- -) for (a) simply-supported boundary condition; and (b) clamped boundary condition.

The physical properties of the elastic supports include the translational stiffness S_t and rotational stiffness S_r where we set $S_\theta = S_\phi = S_r$ for simplicity. A large parametric value of the order of 10^{15} is used for S_t or S_r if negligible translational or rotational displacements are considered in the numerical simulations. Predicted results for two types of edge-mounting supports are presented: the simply supported ($S_t = \infty$ and $S_r = 0$) and clamped support ($S_t = \infty$, and $S_r = \infty$) are shown in Figs. 2.3(a) and 2.3(b) respectively.

The numerical predictions according to the FEM and coupled FEM/BEM models show very good agreements with each other for the 1 Hz bands ranging from 9 Hz to 560 Hz. We have also compared numerical results for other types of supports and other sizes of windows. The results are similar to those presented in Figs. 2.3(a) and 2.3(b) and are therefore not shown here.

By comparing with the numerical results obtained from other computational scheme, it is enlightening to confirm the coupled FEM/BEM model is a good alternative method to FEM model and is sufficiently accurate to predict the transmission of LFN through windows with elastic boundary conditions. The coupled FEM/BEM model will be used in the following parametric studies.

32

2.4. Parametric studies

In the following sub-sections, we shall use the coupled FEM/BEM to compute the TL for various elastic boundary conditions and aspect ratios of the window pane. Again, unless stated otherwise, we consider a 1 m × 1 m × 5 mm (thickness) rectangular glass pane with the Young's modulus, density and Poisson's ratio taken as 70.3 GPa, 2700 kg m^{-3} and 0.35 respectively.

The physical properties of the elastic support of the window pane are characterized by adjusting S_t and S_r to vary from 0 (no constrain) to ∞ (rigidly mounted). We simulate various mounting conditions of the window as in Table 2.1.

In the sub-section (A) below, we examine the effect the fluid loadings on the prediction of TL. We also explore an approximate scheme where the effect of fluid loading is ignored in the analysis. The sub-section (B) addresses the effect of elastic boundary supports on the TL of window panes. We discuss the effect of aspect ratios and damping of a window pane on the predicted TL in sub-sections (C) and (D) respectively. Finally, the effect of boundary supports and the damping of window panes on the overall TL due to a broadband noise source is explored in sub-section (E).

The current section only addresses the TL of a baffled window that can be treated as a limiting case for a window installed in a finite wall of a typical residential building. Pan and Bies showed theoretically (1990a) and experimentally (1990b) that the radiation of sound (and hence the TL) by a boundary structure can be large if the cavity mode of the enclosures matches the resonance mode of the vibrating panel. Using the theoretical model of Pan and Bies (1990a), Venkatesham et al. (2008) developed a numerical model to predict the breakout noise from a rectangular cavity through an elastic wall. In principle, these numerical models can predict the ingress of LFN indoors. However, the sound fields are dependent on (i) the shape and size of a

33

room in a residential building, (ii) the amount of absorption by materials installed in the enclosure, and (iii) the location of the receiver, which make it impossible to generalize the predictions of noise ingression in a typical indoor space. Nevertheless, the numerical results presented below serve to provide sufficient information to assess the acoustic effectiveness of windowpanes.

(A)   The effect of fluid loadings

In Sec. 2.2, a fully coupled FEM/BEM was used to calculate the TL of a baffled window due to incoming acoustic excitations. A useful approximation of the numerical scheme, which is often used to de-couple the FEM from the BEM formulation, is to assume that the fluid loading due to the radiation of sound is negligibly small compared with the incoming pressure, i.e. $\{\mathbf{P}_0\} \gg \{\mathbf{A}\}\{\mathbf{d}\}^{\mathrm{T}}$. From Eqs. (2.8a) and (2.8b), the pressure on the upper surface of the window can then be approximated by:

$$\{\mathbf{P}_1\}^{\mathrm{T}} \approx \{\mathbf{P}_0\}^{\mathrm{T}}. \tag{2.17}$$

The pressure difference between the upper and lower surfaces of the window can be simplified to

$$\{\Delta\mathbf{P}\}^{\mathrm{T}} = \{\mathbf{P}_1\}^{\mathrm{T}} - \{\mathbf{P}_2\}^{\mathrm{T}} \approx \{\mathbf{P}_0\}^{\mathrm{T}}. \tag{2.18}$$

Hence, the FEM is de-coupled from the BEM formulation. The deflection of each element on the window's surface can be approximated by substituting Eq. (2.18) into Eq. (2.12) to yield:

$$\{\mathbf{d}\}^{\mathrm{T}} \approx \{\mathbf{H}\}\{\mathbf{P}_0\}^{T} \tag{2.19}$$

where $\{\mathbf{H}\}$ is given by Eq. (2.13). Substitution of Eq. (2.19) into Eq. (2.8b) leads to an approximate expression for the pressure on the lower surface of the window:

$$\{\mathbf{P}_2\}^\mathrm{T} = 2\{\mathbf{A}\}\{\mathbf{H}\}\{\mathbf{P}_0\}^T \tag{2.20}$$

substituting Eqs. (2.17) and (2.20) into Eqs. (2.14) – (2.16), we can compute an approximate transmission loss of the elastic panel. Here, we shall refer this scheme as the uncoupled FEM/BEM scheme.

We can examine the effect of fluid loadings in the TL computations by using the coupled and uncoupled FEM/BEM formulations for different boundary conditions. For a free or guided support, the panel admits vibrations due to rigid modes in addition to elastic modes (Berry et al 1990). The rigid modes have the fundamental resonant frequency equal to zero. They are identified as the piston motion (mode 0) plus two rigid rotations about the x and y axes (modes 1 and 2) in the free support case but there is only the piston motion (mode 0) in the guided support case.

Figure 2.4(a) shows the predictions of TL with (coupled FEM/BEM scheme; solid line) and without (uncoupled FEM/BEM scheme; dashed line) the inclusion of fluid loadings in the formulation for a guided support panel. The numerical simulation for a freely supported panel is not shown because it is similar to those for guided edges. Because of the piston motion of the panel at low frequencies, there is no apparent 'dip' in the TL spectrum in one-third octave frequency bands. The predicted TL is relatively small at low frequencies because of the rigid motion of the window. In both cases, the effect of fluid loadings is generally small.

In Figs. 2.4(b) and 2.4(c), we show the numerical results for simply supported and clamped windows. Again, TL spectra in one-third octave frequency bands are presented with the predictions calculated according to the coupled and uncoupled FEM/BEM schemes. It can be seen from Fig. 2.4(b) and 2.4(c) that the effect of fluid loading is generally small for all frequencies except at the region close to resonant frequencies. It is evident from the predictions

that the fluid loading effect is an important factor near the resonant frequency even for such a light fluid medium as air. It is crucial to use the full (coupled) FEM/BEM scheme to calculate the transmission of LFN through windows. In the following sections, the coupled FEM/BEM scheme will be used in all simulations.
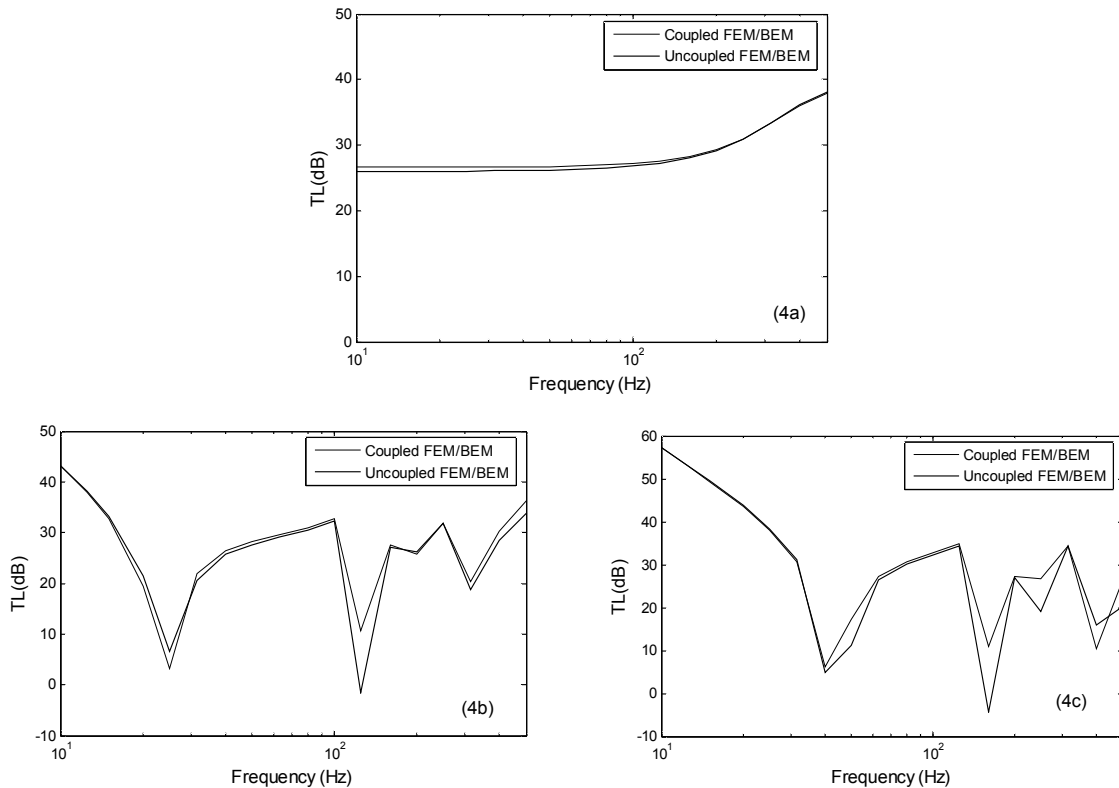
Fig. 2.4. Comparison of 'coupled FEM/BEM' (−) and 'uncoupled FEM/BEM' (- -) in one-third octave frequency bands. (4a) Guided, (4b) Simply supported, (4c) Clamped.

(B) The effects of the elastic support at the boundary

At the low frequency region below the fundamental resonant frequency, it is well known that the TL is controlled by the stiffness of the panel. This region is often referred as the stiffness controlled region of an elastic panel (Quirt, 1982). In this region, TL decreases as the frequency of LFN excitation increases until it reaches its minimum at the first fundamental resonant frequency of the window with an elastic support. When the excitation frequency increases above

the fundamental resonant frequency, the shape of the TL spectrum is dominated by the higher order resonant frequencies of the system. The dips in the TL spectrum also occur at some other resonant frequencies. Typically, the TL for the fundamental resonant frequency is the lowest. After the resonance controlled region and before the coincidence controlled region, it is usually referred as the mass controlled region (Quirt, 1982).
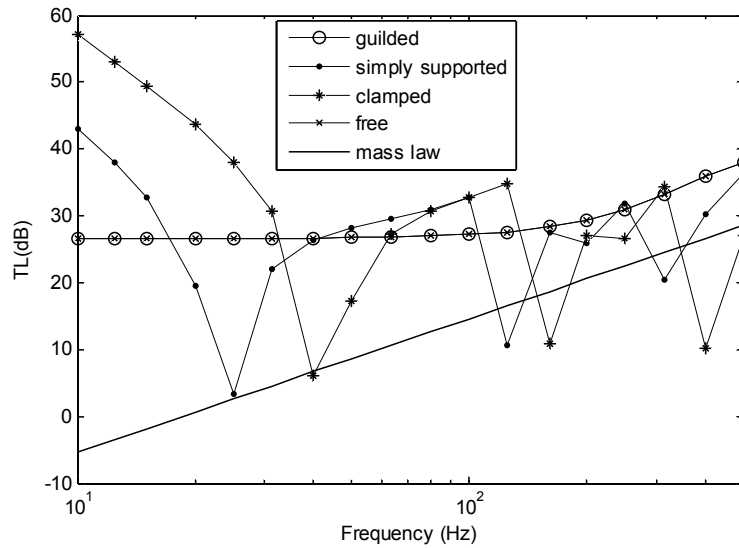
Fig. 2.5. Transmission loss spectra for windows with different boundary conditions. In the numerical simulations, the glass pane has dimensions of 1 m × 1 m × 5 mm (thickness) with the Young's modulus, density and Poisson's ratio taken as 70.3 GPa, 2700 kg m^{-3} and 0.35 respectively.

In Fig. 2.5, we display the predicted one-third octave TL spectra for a window pane in the order of increasing system stiffness for the free, guided, simply supported and clamped edges. As a benchmark, we also show the predicted TL spectra according to the mass law. The predictions for a window pane with free and guided supports at all its edges show similar results. As shown in the plots and noted by Chiello et al (2003), there is no apparent dip in the TL spectrum, i.e. no resonant frequency, for the window pane with very small boundary translational stiffness. The predicted TL at 10 Hz is about 31 dB higher than the prediction according to the mass law. The

37

predicted TL increases with the frequency but the difference between these two predictions gradually reduces as the frequency increases.

At 10 Hz, the predicted TL of the window pane is 57 dB for the clamped support and 43 dB for the simply supported. Both predicted values are significantly higher than the mass law prediction, see Fig. 2.5. However, as shown in Fig. 2.5, the predictions have shown clear 'dips' in the TL spectra at the respective resonant frequencies for the window pane with simply-supported and clamped edges. At the regions in the vicinity of the resonant frequencies, the TL is lower than that predicted by the mass law. As the frequency increases, the general trend of the calculated TL agrees reasonably well with that predicted by the mass law.

Case	S_t	S_r	Boundary conditions
1	∞	$0 \sim \infty$	Simply-supported ~ clamped
2	$0 \sim \infty$	0	Free ~ simply-supported
3	$0 \sim \infty$	∞	Guided ~ clamped

Table 2.1. Typical mounting conditions of windows for the transmission of sound.

In addition to the above supports, Table 2.1 lists three other typical mounting conditions for the window that will be used in the numerical simulations presented in this section. They can be summarized as follows. For Case 1, the window pane changes from clamped to simply supported edges with $S_t \rightarrow \infty$ and $S_r = (0, \infty)$. Case 2 represents the situation where the window support changing from simply supported to free edges where $S_r = 0$ and $S_t = (0, \infty)$. Finally, Case 3 is chosen with $S_r \rightarrow \infty$ and $S_t = (0, \infty)$ which simulates the situation where the window support varies from guided to clamped edges.

To highlight the effect of elastic boundary supports, we show in Fig. 2.6 a series of the TL spectra for Case 1 listed in Table 2.1. We can see that the resonant frequency increases as S_r

increases. The fundamental resonant frequency increases from about 25 Hz for the simply supported edges to about 45 Hz for the clamped edges. Below the fundamental resonant frequency of that for the simply supported window pane, the predicted TL increases with the increase of S_r. However, there are no general patterns for other frequencies because of the dips in the TL spectra generally shifted to higher frequencies for a higher system stiffness.
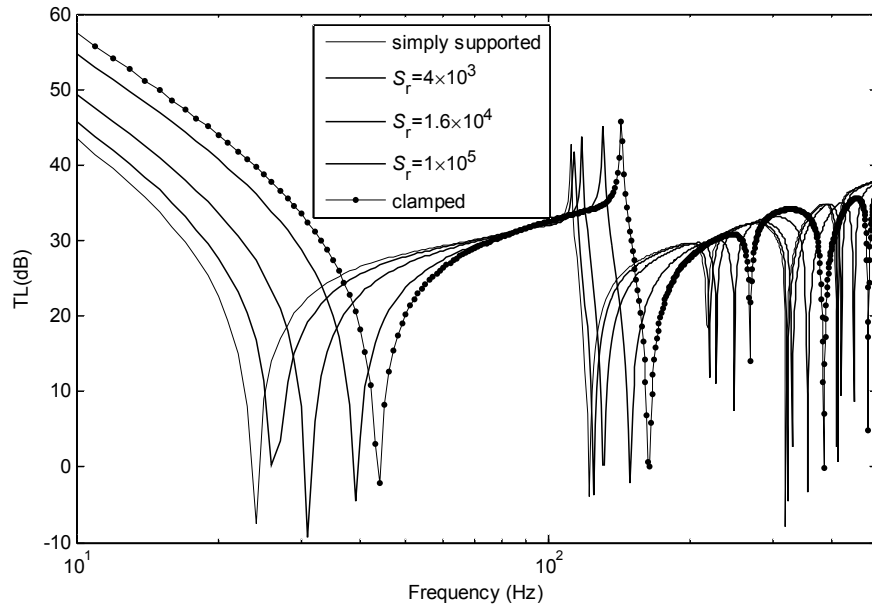
Fig. 2.6. Transmission loss spectra for windows with different parametric values of S_r with $S_t = \infty$. The same glass pane as Fig. 2.5 is used here.

Figure 2.7 displays different plots of TL versus S_r for different octave band frequencies ranging from 16 Hz to 500 Hz. For the 16 Hz and 125 Hz bands, TL increases with S_r. On the other hand, TL decreases with S_r for the 63 Hz, 250 Hz and 500 Hz bands. There is an interesting feature for the 31.5 Hz band: the predicted TL has a stationary point (a minimum value in TL for this case) as S_r varies. Combination of Figs. 2.6 and 2.7, we can see that the minimum value in 31.5 Hz band is at about $S_r = 1 \times 10^4$ Nm/rad.
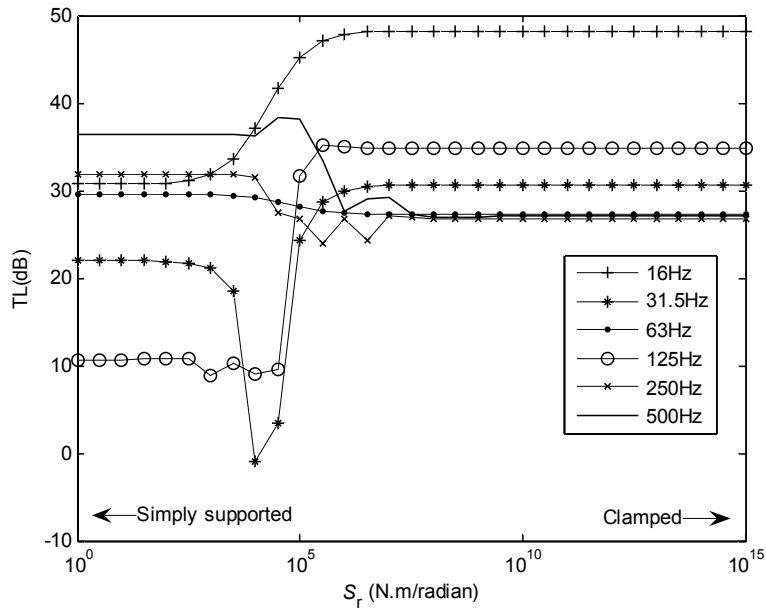
Fig. 2.7. Transmission loss versus S_r for octave band frequencies ranging from 16 Hz to 500 Hz. The same glass pane as Fig. 2.5 is used here.

Similar to rotational stiffness S_r, there are no general relationships between TL and S_t for different frequency bands: increase the total translational stiffness does not necessarily increase the TL at a particular one-third octave band. However, there is a notable aspect for varying S_t from 0 to infinity and keeping S_r unchanged in Cases 2 and 3. Their respective TL spectra are shown in Figs. 2.8 and 2.9 for illustration. When S_t tends to zero, there exists a rigid mode (mode 0) in the plate that has the fundamental resonant frequency equal to zero. Because of the piston motion at low frequencies, there will be no dips in the TL spectra for the fundamental resonant frequencies in these situations. The increase in S_t has led the replacement of the rigid mode with the elastic mode (1, 1). A dip in the fundamental resonant frequency can be observed for a threshold value dependent on the S_r. As shown in Figs. 2.8 and 2.9, dips in TL spectra are observable when $S_t > 3 \times 10^5$ N m^{-1}. The fundamental resonant frequencies are shifted to higher frequencies for higher S_t and S_r.

40
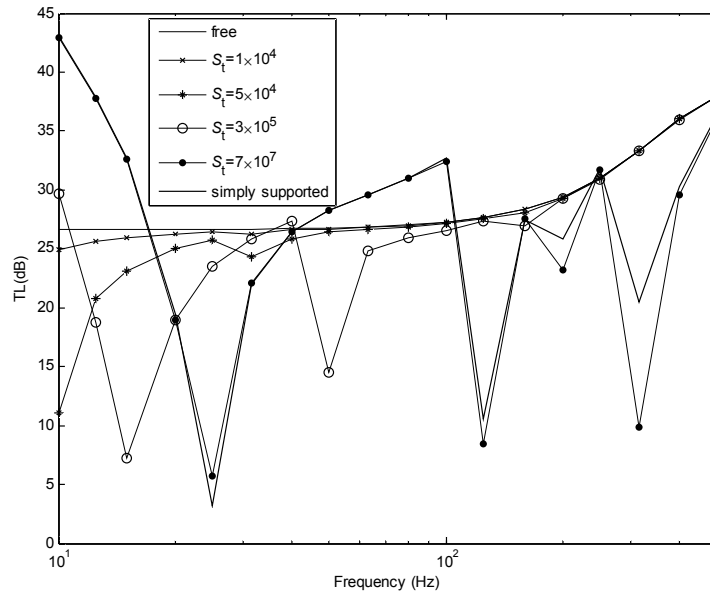
Fig 2.8. Transmission loss spectra for windows with different parametric values of S_t with $S_r = 0$. The same glass pane as Fig. 2.5 is used here.
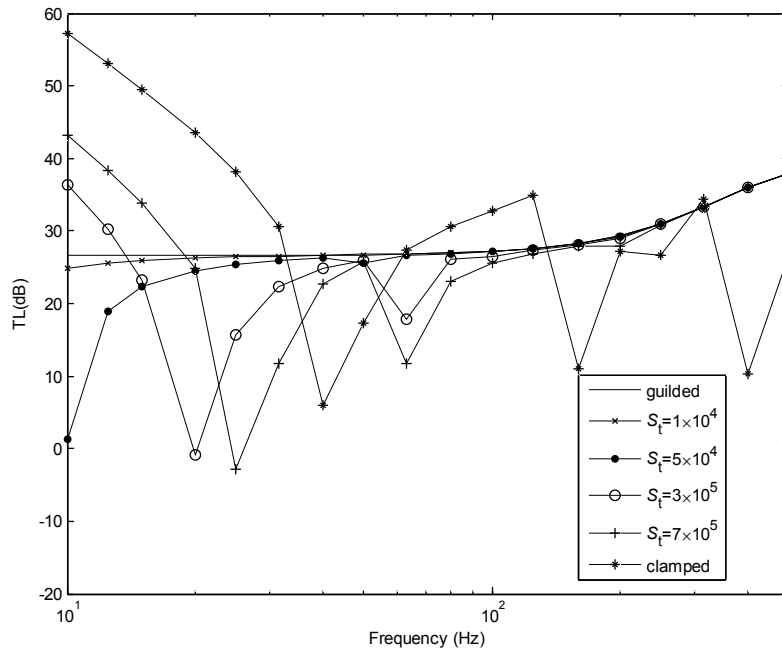
Fig. 2.9. Transmission loss spectra for windows with different parametric values of S_t with $S_r = 0$. The same glass pane as Fig. 2.5 is used here.

(C)   The effects of the window's aspect ratio

The aspect ratio of the window is defined by $r = L_x/L_y \geq 1$. Without the loss of generality, we can simply interchange L_x and L_y if $L_x < L_y$, which means interchanging L_x and L_y would result in the same TL results. Figure 2.10 shows the one-third octave TL spectra for different r with the area held constant at 1 m^2 within the stiffness controlled region. We only show the predicted results with the simply-supported boundary conditions. Similar results are found for other boundary conditions and they are not shown for succinctness.

As shown in Fig. 2.10, the 'dips' of the predicted TL spectra shift to the higher frequencies when aspect ratio r increases. Figure 2.10 also shows the predicted TL according to the mass law. It agrees reasonably well with those TL for different r predicted by the coupled FEM/BEM model.
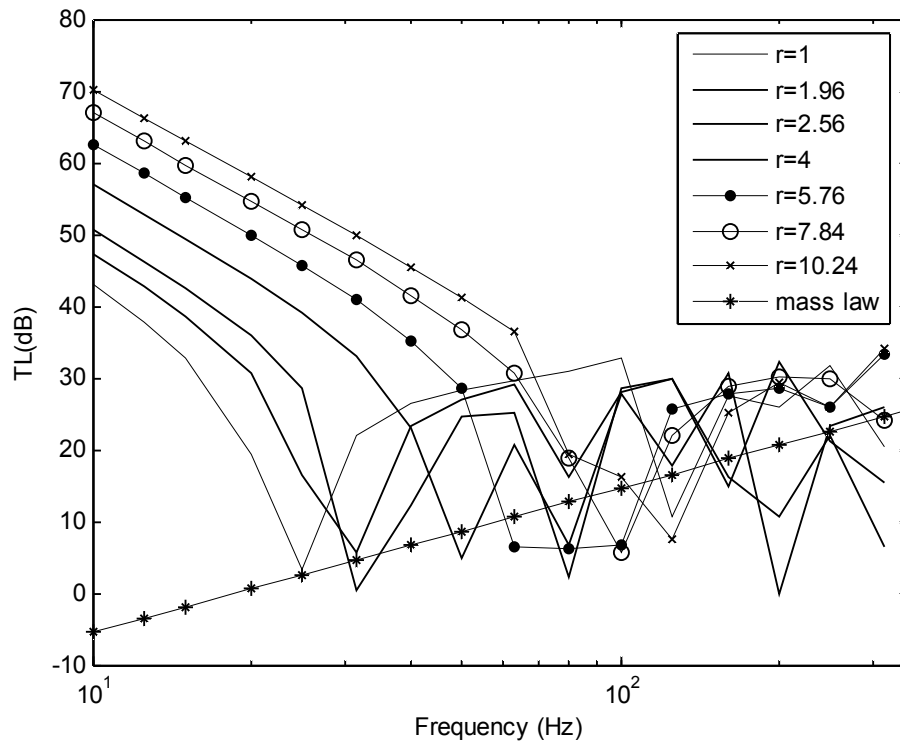
Fig. 2.10. Transmission loss spectra for windows with the same area but different aspect ratios within the stiffness controlled frequency regime. The same glass pane as Fig. 2.5 with the same area but different aspect ratios is used here.

42

Figures 2.11 and 2.12 show the predicted TL versus r for different one-third octave frequency bands in the stiffness- and resonance- controlled regions, respectively. As shown in Fig. 2.11 for the stiffness controlled region, the predicted TL show minimum values for $r = 1$, i.e. for a square window, and as r increases, the TL increases. However, this is not the case for the resonance controlled region, see Fig. 2.12. The predicted TL is dominated by the effect of panel resonant occurring at the fundamental frequency of the system.
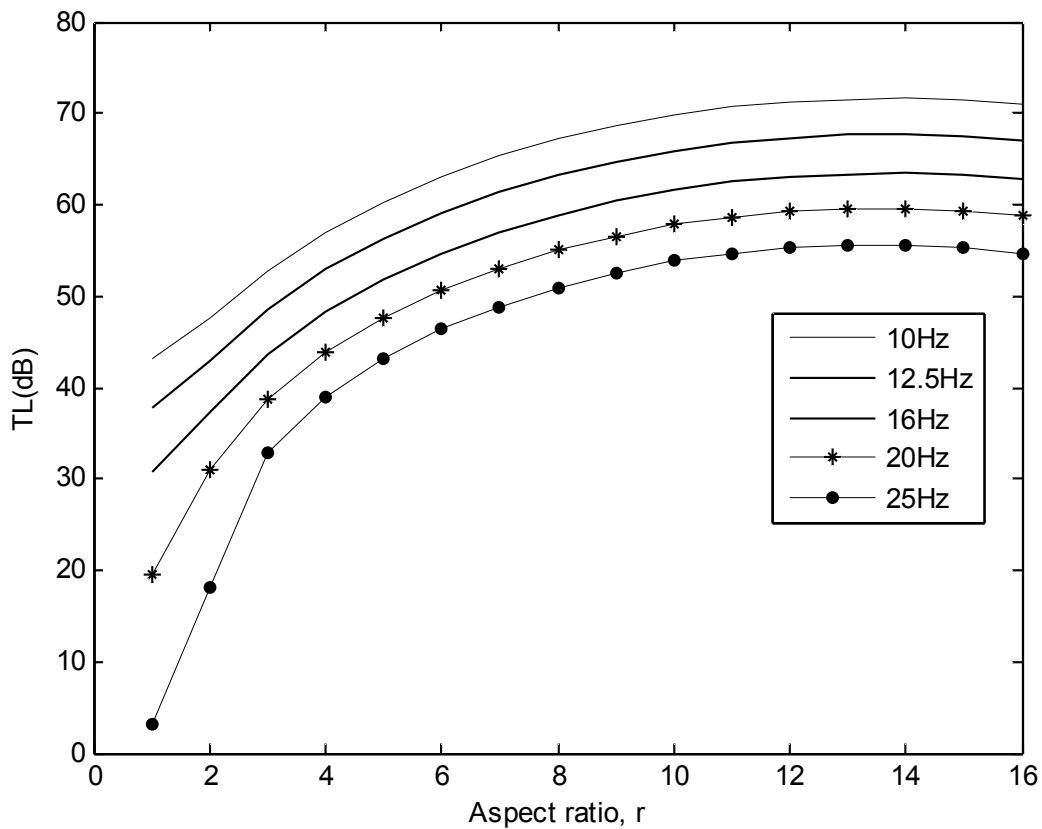
Fig 2.11. Transmission loss versus the aspect ratio of windows with the same area within the stiffness controlled frequency regime. The same glass pane as Fig. 2.5 is used here.
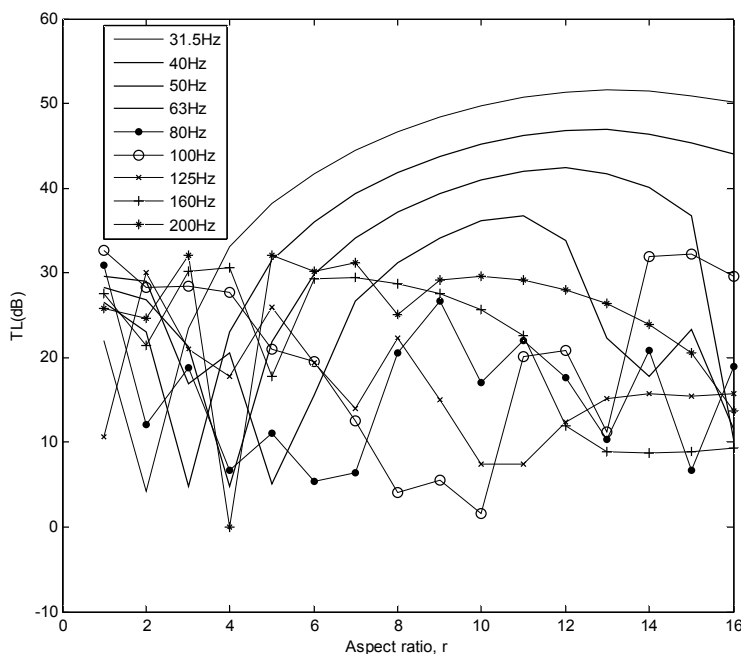
Fig. 2.12. Transmission loss versus the aspect ratio of windows with the same area within the resonance controlled regime. The same glass pane as Fig. 2.5 is used here.

(D)   The effects of damping of the windows
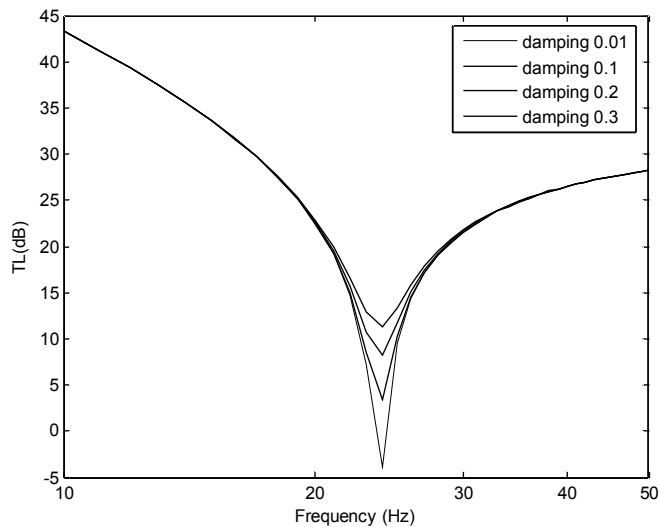
Fig. 2.13. Transmission loss spectra for windows with different damping ratios in 1-Hz frequency bands (10 ~ 50 Hz). The same glass pane as Fig. 2.5 is used here.

We examine the advantage of introducing damping at the window pane. Fig. 2.13 shows the TL

spectra in narrow frequency bands (1 Hz) for different damping ratios (0.01, 0.1, 0.2 and 0.3) of the windows with simply-supported edges. Below 50 Hz, the effect of damping is only observable at and around the fundamental resonant frequencies of the system and it is negligible at other non-resonant frequencies. The predicted resonant frequencies are very close for different damping ratios. Effectively, the resonant frequency can be treated as independent of the damping ratio of the window. Figure 2.14 shows the TL spectrum in one-third octave bands for different damping ratios of the windows. For frequencies below 80 Hz, we can see that the effect of damping is only significant near the resonant frequency. However, the effect of damping is more significant as the frequency increases.
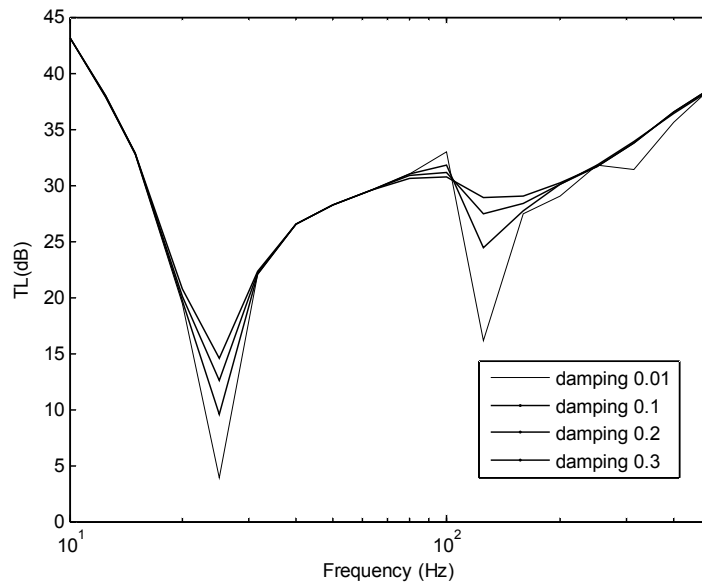
Fig. 2.14. Transmission loss spectra for windows with different damping ratios in one-third octave frequency bands (10 ~ 500 Hz bands). The same glass pane as Fig. 2.5 is used here.

(E)   Transmission of broadband LFN through a window pane

We can now assess the impact of a broadband LFN on the windows with different elastic boundary supports. For the purpose of illustration, we assume that the LFN has equal spectral levels for frequency ranging from 9 Hz to 112 Hz. The overall TL is defined as the equivalent

TL over the frequency band (9 Hz ~ 112 Hz). Figure 2.15 shows the variation of the overall TL for windows with the boundary supports of varying S_t but with negligible S_r (of the order of 0.01 N m rad^{-1}). In this plot, we consider a rectangular steel plate of 3 mm thick with dimensions 0.48 m × 0.4 m. The Young's modulus, density and Poisson ratio of the steel plate are set at 2×10^{11} Pa, 7800 kg m^{-3} and 0.3 respectively. For the damping ratio of 0.01, our numerical results are comparable with that shown in Fig. 2.11 of Chiello et al (1999). We also show further numerical simulations for three additional damping ratios of 0.05, 0.1 and 0.2 in Fig. 2.15. These numerical results will provide insight for reducing the transmission of broadband LFN through windows.
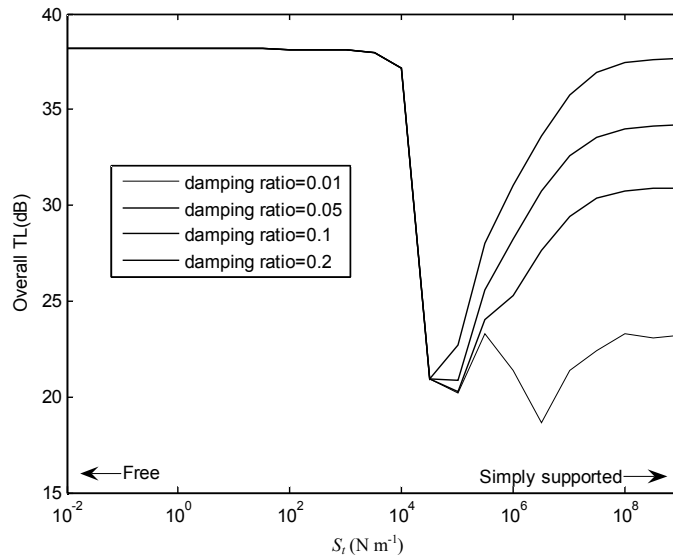
Fig. 2.15. Variation of the overall transmission loss due to a broadband LFN source with the boundary translational stiffness. The damping factors of 0.01, 0.05, 0.1 and 0.2 are used in the numerical simulations.

As mentioned earlier, the window has the freely supported boundaries when the translational stiffness is set as a small parameter less than 1 N m^{-1}. In this case, the rigid modes have the fundamental resonant frequency equal to zero. The dominant mode of vibration can be identified as the piston motion (mode 0) for an excitation frequency below 100 Hz. In the absence of the dip in the narrow band TL spectra [see Fig. 2.4(a)], the overall TL for a broadband LFN is maximized. The increase of S_t leads to a gradual introduction of a resonant dip

in the narrow band TL spectrum, see Fig. 2.5. With a small damping on the window, most of the sound energy will be transmitted through the window in the region close to the first resonant frequency. Hence, there is a sharp degradation of the acoustic performance of the window in terms of its overall TL when S_t increases from 1×10^4 to 3×10^4 N m^{-1}. A further increase in S_t does not cause a further degradation of the overall TL. The further increment in S_t only leads to a shift of the resonant frequencies to the higher end without a significant change in the 'narrow band' TL.

Hence, we can improve the acoustic performance of the overall TL for a broadband LFN by limiting the vibration level at the fundamental resonant frequency. This can be achieved by increasing the damping ratio of the window. As shown in Fig. 2.15, the overall TL is enhanced by increasing the damping ratio of the window when $S_t > 3\times10^4$N m^{-1}.

Next, we wish to examine the acoustic performance of the typical window examined earlier. See the caption of Fig. 2.5 for the parametrical values and dimensions of the window. Figure 2.16 shows contour plots for the overall transmission loss for different translational and rotational stiffness with four different damping ratios of 0.01, 0.05, 0,1 and 0.2 respectively. Again, the broadband noise has constant spectral levels with frequency ranging from 9 Hz to 112 Hz. Generally speaking, when S_t is less than about 1×10^4 N m^{-1}, the overall transmission loss is relatively insensitive to the change of S_r: changing the rotational stiffness does not affect the overall transmission loss (Chiello et, 2003). This is not the case when the S_t is higher than 1×10^5 N m^{-1}. As shown in Fig. 2.16, we can see a noticeable reduction in the overall TL as S_r increases. We also observe that the overall TL is highest at about 26 dB for all damping ratios when S_t is less than 1×10^4 N m^{-1}. For small damping conditions (0.01 or 0.05), the overall TL is lower for a clamped or simply supported window because of the dip at around the region of the resonant

47

frequency. Increase the level of damping of the window can generally improve its acoustic performance when S_t is greater than $1 \times 10^4 \, \text{N} \, \text{m}^{-1}$.

The numerical simulations in this section can be summarized as follows. We can improve the overall TL due to a source of broadband LFN by (1) reducing the translational stiffness, or (2) increasing the damping of the boundary support.
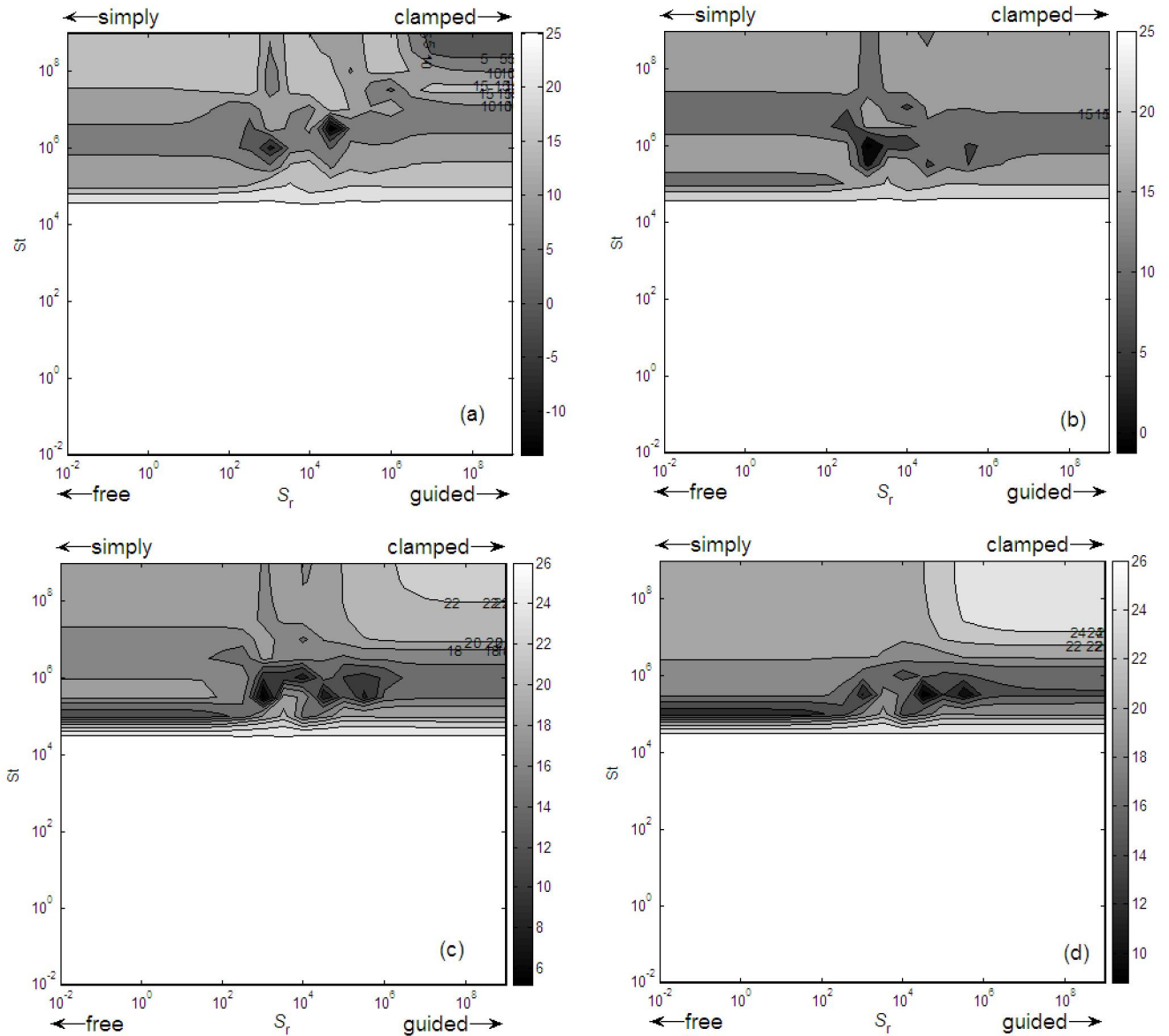
Fig. 2.16. The contours of the overall transmission loss of windows which is subjected to a broad-band noise between 9 Hz and 112 Hz. The same glass pane as Fig. 2.5 is used here. The damping ratio is (a) 0.01, (b) 0.05, (c) 0.1 (d) 0.2.

48

2.5. Comparisons with experimental results

In 1980's, Quirt (1982) conducted a series of experiments to measure the TL of simply-supported windows. More recently, Osipov *et* al (1997, 1999) presented experimental results for the transmission of LFN through a partition in buildings. Quirt used his experimental data to validate the theoretical models developed by Sewell (1970) and Nilsson (1972, 1974, 2000). Although the mounting condition of windows (i.e. the boundary condition) did not give much effect on the TL at the high frequency region, it is obvious from Quirt's experimental data that the boundary conditions affected the measured results at the resonance-controlled region.

Table 2.2. Parametric values of the translational stiffness (S_t) and rotational stiffness (S_r) used in the numerical simulations for comparison with the published experimental data (Quirt, 1982).

Windows	S_t (N m^{-1})	S_r (Nm/radian)
3-*mm*	10^5	10^2
4-*mm*	8×10^4	10^3
6-*mm*	10^6	10^5

As an application of our model, we show a comparison of the predicted results according to the fully coupled FEM/BEM model with experimental data published by Quirt (1982) for single pane windows of thickness 3, 4 and 6 mm. The size of these three sets of windows was the same with dimensions of 560 mm × 1680 mm but the glass panes used were different with the surface densities of 8.1, 10.4 and 14.4 kg m^{-3} respectively. The information provided in Quirt (1982) was not sufficient to estimate the numerical values of S_t and S_r in order to quantify the boundary support of the windows. As a result, we adjust S_t and S_r (and keep them the same at different frequencies) in our calculations until the predicted TL showed reasonable agreements with the experimental data. However, no attempt has been made to optimize S_t and S_r in order to give the best agreement with experimental data. The empirical parameters, S_t and S_r, used for

different windows are listed in Table 2.2 for information.
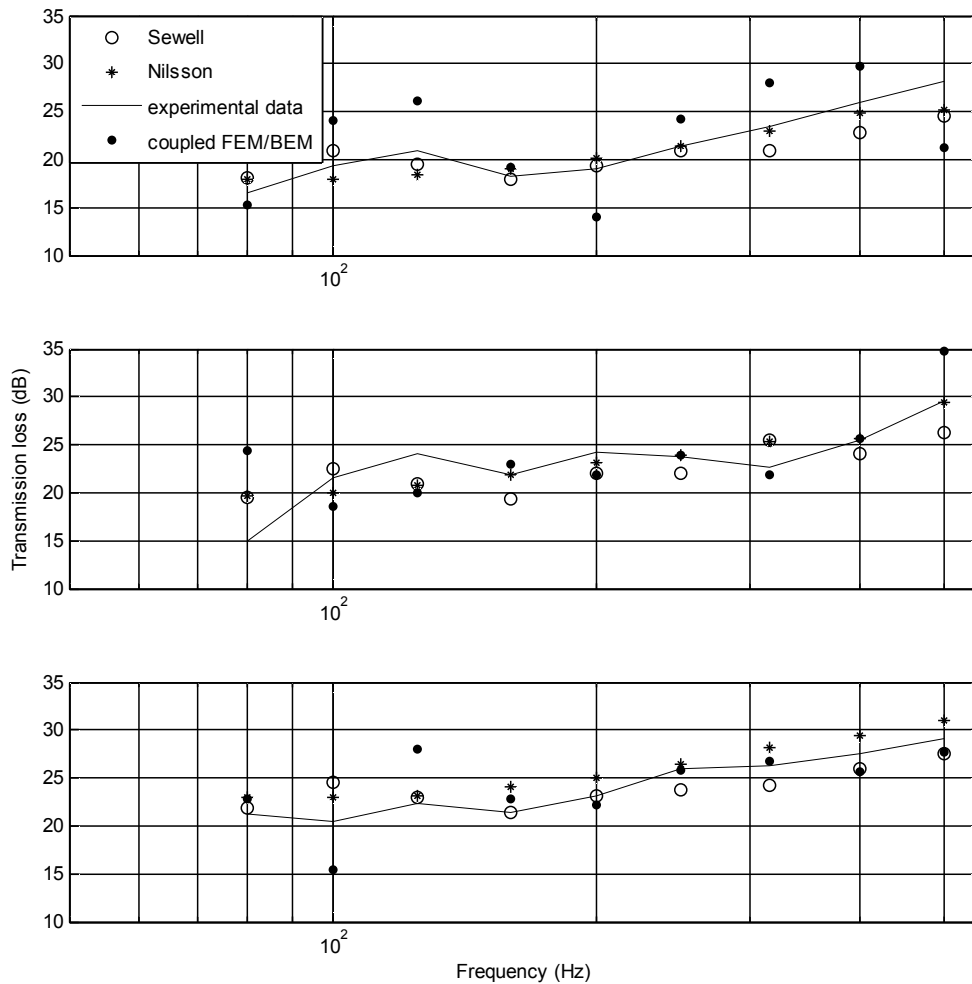
Fig. 2.17. Comparison of the transmission loss computed by the coupled FEM/BEM model (•), Sewell (1970) expression (o), Nilsson (1972) expression (*) and experimental data (Quirt, 1982) (−). (a) 3-*mm* glass, (b) 4-*mm* glass, and (c) 6-*mm* glass.

The predicted results are presented in Fig. 2.17. Since the low frequency region is our focus, we

only show the comparison for the third-octave bands at the low frequencies below 560 Hz. In the

plots, we also show the theoretical predictions according to Sewell (1970) and Nilsson (1972). It

can be seen that the predicted results according to the coupled FEM/BEM model give reasonable

agreements with the Quirt's experimental data for windows of different thicknesses.

2.6. Conclusions

A coupled FEM/BEM model using the technique of the component mode synthesis has been used to predict the transmission of LFN through a window with a set of elastic boundary conditions. The FEM/BEM model performance was first verified against ANSYS FEM models. It was then used in a series of parametric studies to examine the effects of fluid, elastic boundary conditions, window aspect ratio, and window damping on TL for different frequencies. Numerical simulations have been demonstrated that the effect of fluid (air) loading is generally small at all frequencies except in the region close to the resonant frequencies. With the use of numerical simulations, this section examines the problem of building isolation at low frequencies in a more systematical way. Through parametric studies, the acoustic performance of the single pane windows has been examined. It has been shown in the numerical simulations that

(i) The effect of fluid loading is an important factor to predict the transmission loss of LFN at the resonant frequencies.

(ii) The boundary conditions have important effects on the TL, especially at the location of the resonant frequencies;

(iii) The aspect ratio of the windows has significant effects on TL in the stiffness- and resonance- controlled regions. In the stiffness-controlled region, increasing the aspect ratio generally leads to an increase in the TL of the window at all frequencies. On the other hand, there is no general trend in predicting TL for the resonance-controlled region.

(iv) The effect of damping on TL is important at the fundamental frequencies. Increasing the damping leads to a reduction in TL in the regions near the resonant frequencies.

51

References

ANSYS user's manual for revision 10.0. Houston, PA: Swanson Analysis Systems, Inc., 1992.

N. Atalla and R. J. Bernhard, 1994. "Review of numerical solutions for low-frequency structural-acoustic problems," *Applied Acoustics* **43**, 271-293.

A. Berry, J.-L. Guyader and J. Nicolas 1990. "A general formulation for the sound radiation from rectangular, baffled plates with arbitrary boundary conditions," *Journal of the Acoustical Society of America* 8**8**, 2792-2802.

Chiello, O., Sgard, F., and Atalla, N., 2000. "Direct and flanking sound transmissions in enclosures for separated walls mounted on elastic joints at low frequencies," *Proceedings 16th International Congress on Sound and Vibration*, 1589-1596.

Chiello, O., Sgard, F., and Atalla, N., 1999. "A modal synthesis approach to investigate the influence of viscoelastic boundary conditions on the sound radiated from a cavity-backed plate," *Journal of the Acoustical Society of America* **105**, 1087.

O. Chiello, F. C. Sgard, and N. Atalla, 2003. "On the use of a component mode synthesis technique to investigate the effects of elastic boundary conditions on the transmission loss of baffled plates," *Computers & Structures*, **81**, 2645-2658.

R. R. Craig, 1977. "Methods of component mode synthesis," Shock Vibration Digest, **9**, 3–10.

J. M. R. Craik, 1996. *Sound transmission through buildings: using statistical energy analysis,* Aldershot, Hampshire, England; Brookfield, Vt.: Gower.

G. C. Everstine and F. M. Henderson, 1990. "Coupled finite element/boundary element approach for fluid-structure interaction," *Journal of the Acoustical Society of America* 8**7**, 1938-1946.

W. S. Hwang, 1997. "A boundary integral method for acoustic radiation and scattering," *Journal of the Acoustical Society of America* **101**, 3330–3335.

R. A. Jeans and I. C. Mathews, 1990. "Solution of fluid-structure interaction problems using a coupled finite element and variational boundary element technique," *Journal of the Acoustical Society of America* **88**, 2459-2466.

L. E. Kinsler, A. R. Frey, A. B. Coppens, J. V. Sanders, 2000. *Fundamentals of acoustics*, Fourth Edition, New York, John Wiley.

B. U. Koo, B. C. Lee, J. G. Ih, 1996. "A non-singular boundary integral equation for acoustic problems," *Journal of Sound and Vibration* **192**, 263-279.

S. Kopuz, Y. S. Unlusoy, M. Caliskan, 1996. "Integrated FEM/BEM approach to the dynamic and acoustic analysis of plate structures," *Engineering Analysis with Boundary Elements*, **17**, 269-277.

K. M. Li, Z. Yu, 2009. "A simple formula for predicting resonant frequencies of a rectangular plate with uniformly restrained edges," *Journal of Sound and Vibration* **58**, 483-500.

S. Li and D Zhao, 2004. "A modal method for coupled fluid-structure interaction analysis," *Journal of Computational Acoustics* **12**, 217-231.

I. C. Matthews, 1986. "Numerical techniques for three-dimensional steady-state fluid-structure interaction," *Journal of the Acoustical Society of America* **79**, 1317-1325.

A. C. Nilsson, 1972. "Reduction index and boundary conditions for a wall between two rectangular rooms I. Theoretical results; II. Experimental results," *Acustica*, **26**, 1-23.

A. C. Nilsson, 1974. "Sound transmission through single leaf panels." Rep.74-01, Building Acoustics, Chalmers University of Technology, Sweden.

A. C. Nilsson, 2000. *Vibroacoustics*. The Marcus Wallenberg Laboratory for Sound and Vibration Research, Stockholm.

A. Osipov, P. Mees, and G. Vermeir, 1997. "Low-frequency airborne sound transmission through single partitions in buildings", *Applied Acoustics* **52**, 273-288.

A. Osipov, P. Mees, and G. Vermeir, 1999. "Low-frequency airborne sound transmission through single partitions in buildings – Part 2", *Noise and Vibration Worldwide*, **30**, 21-26.

J. Pan and D. A. Bies, 1990a, "The effect of fluid-structural coupling on sound waves in an enclosure – Experimental part," *Journal of the Acoustical Society of America* **87**, 708-717.

J. Pan and D. A. Bies, 1990b, "The effect of fluid-structural coupling on sound waves in an enclosure – Theoretical part," *Journal of the Acoustical Society of America* **87**, 691-707.

J. S. Przemieniecki, *Theory of Matrix Structural Analysis*, Dover Publications, New York, 1985.

J. D. Quirt, 1982. "Sound transmission through windows – 1. single and double glazing," *Journal of the Acoustical Society of America* **72**, 834-844.

E. C. Sewell, 1970. "Transmission of reverberant sound through a single-leaf partition surrounded by an infinite rigid baffle," *Journal of Sound and Vibration* **12**, 1-32.

A. F. Seybert and T. Wu, 1989. "Modified Helmholtz integral equation for bodies sitting on an infinite plane," *Journal of the Acoustical Society of America* **85**, 19–23.

F. Sgard, N. Atalla and J. Nicolas, 1994. "Coupled FEM-BEM approach for mean flow effects on vibro-acoustic behavior for planar structures," *AIAA Journal*, **32**, 2351-2358.

W. Soedel, *Vibrations of shells and plates*, Marcel Dekker, Inc., New York, 1993.

B. Venkatesham, M. Tiwari and M. L. Munjal, 2008, "Analytical prediction of the breakout noise from a rectangular cavity with one compliant wall," *Journal of the Acoustical Society of America* **124**, 2952-2962.

C. E. Wilson, 1994. *Noise control: measurement, analysis, and control of sound and vibration*, Malabar, FL, Krieger publishing company.

D. T. Wilton, 1978. "Acoustic radiation and scattering from elastic structures, "*International Journal for Numerical Methods in Engineering* **13**, 123-138.O. C.

T. W. Wu and A Dandapani, 1994. "A boundary element solution for sound transmission through thin panels," *Journal of Sound and Vibration* **171**, 145-157.

S. W. Wu and S. W. Wu, 2001. "A robust formulation for solving fluid-structure interaction problems," *Computational Mechanics*, **27**, 29-74.

O. C. Zienkiewciz, D. W. Kelly, and P. Bettess, 1977. "The coupling of finite element and boundary solution procedures," *International Journal for Numerical Methods in Engineering* **11**, 355-375.

3. Reduction of low frequency noise transmitted through a single-pane window

3.1 Introduction

The present chapter aims to explore a practical means for mitigating the transmission of low frequency noise (LFN) through windows. Typically, sound absorption and damping materials are used to reduce the levels of sound transmitted indoors. However, these materials become ineffective for reduction of low frequency noise. It has been demonstrated in the last chapter that sound transmission through panels in the very low-frequency region is typically stiffness-controlled and is also dependent on the resonances of the window. Hence, by increasing the stiffness and aspect ratio of a window, it is possible to increase the transmission loss of a window at low frequency, i.e. to reduce the ingression of LFN.

Work with stiffened plates has typically been conducted in the context of either sandwich panels or periodically stiffened structures, such as those with regular beam spacing or corrugations. Mead (1975; 1990) considered mode shapes and wave propagation in periodically stiffened plates, and Lee and Kim (2002) derived equations to predict sound transmission through periodically stiffened panels. They found that the effect of panel stiffening was significant in raising the transmission loss of the panel at lower frequencies. More recently, Wang et al. (2005) modeled sound transmission through a periodically-stiffened plate by modeling the plate structure as a single unit having homogenous properties. However, the addition of periodic supports is generally not practical for windows since the addition of numerous stiffening elements may result in unacceptable visual obstruction.

Photiadis (1992) studied vibration propagation through fluid-loaded plates with irregularly-spaced stiffening elements. He constructed simulations of the stiffened plates and

tested the results of vibration propagation with fluid coupling, and demonstrated localization of energy in the plate.

The current study exploits the use of a stiffening element to improve the acoustical performance of a single panel at frequencies below 150 Hz. In particular, theoretical and experimental studies are conducted to investigate the possible use of internal stiffening of windows for reduction of LFN. The finite element model (FEM) which was used to examine the feasibility of such an approach for reduction of low frequency noise (LFN) transmitted through a single pane window is described in Sec. 3.2. Numerical simulations are then presented in Sec. 3.3 to illustrate the effectiveness of using a single pane window with stiffening elements for reducing the transmission of LFN indoors. An experimental study is presented in Sec. 3.4 to validate of the numerical model used in the current study. Finally, concluding remarks for Chapter 3 are offered in Sec. 3.5.

3.2. Finite-element modeling
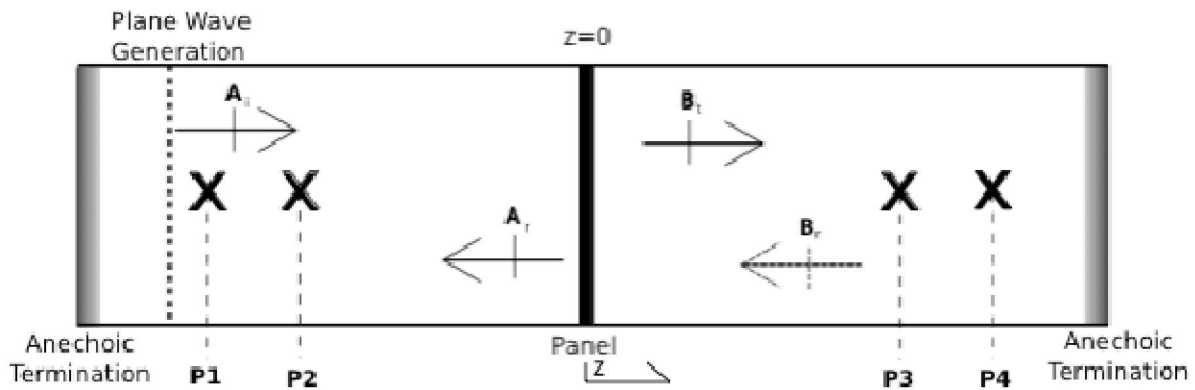
Fig. 3.1. Geometry, measurement points, and defining characteristics
of the set up of standing wave tube.

Finite element method (FEM) modeling of panel transmission was performed here to gauge the effects of various structural elements on the transmission of LFN. The current numerical model,

shown in Fig. 3.1, is similar to a standing wave tube. Incoming pressure waves were generated in the fluid on one side of the panel and were allowed to propagate away from the panel through the fluid on the other side of the panel. The advantage of using the current FEM scheme is that stiffening elements can be added without changing the geometry of the model. As a result, any changes in the transmission loss of the panel configuration can be attributed to the structural changes in the panel.

The FEM was used to model panels with multiple natural frequencies below 150 Hz. While these models were not explicitly based on actual windows, they represent idealizations useful for identifying trends. The basic, fully-constrained isotropic panel was modified by including single stiffening elements across the panel and by allowing for finite edge stiffness by including elastic mounting elements.

In the FEM models, the panel spanned the full cross-section of a long, rigid-walled tube, and the size of the tube was such that only plane waves propagated at all frequencies considered. As a result, there was no baffling around the panel: the tube and the panel had identical height and width. The panel's edges could be constrained at the wall of the "tube" in a variety of ways without interfering with the incident sound field. Other changes, such as the addition of stiffening elements, could be easily made and adjusted in this model without affecting the plane wave behavior of sound in the tube.

Application of these various boundary conditions on the plate structure and plane-wave requirements in the tube yielded a model consisting of a 1 meter square tube. The anechoic terminations in the tube were located 2 meters from the panel in both directions. The panel was 1 meter square "glass" having a density of 2180 kg m^{-3} and a thickness of 2.5 mm. A Young's modulus, E, of 6.8×1010 N m^{-2} and a Poisson's ratio, v, of 0.19 were assumed for the glass in the

numerical simulations described below.

Numerical simulations were conducted from 1 Hz to 150 Hz in 1 Hz increments. The harmonic analysis mode was used in ANSYS, thus representing steady-state oscillation for plane wave transmission. Post-processing of the FEM model yields the transmission loss of the panel. In the current model, a technique known as the four-microphone standing wave tube measurement (Song and Bolton, 2000) was adopted to determine the transmission loss of the panel.

As shown in Fig. 3.1, points P2 and P3 were located 1.1 m from the panel and the spacing between P1 and P2 and between P3 and P4 was set at 0.3 m in the numerical simulations. The phase and magnitude of the pressures at the four points can be used to formulate the magnitude of the plane wave coefficients for right-traveling (A_i and B_t) and left-traveling (A_r and B_r) waves on both sides of the panel, i.e.,

$$A_i = \frac{i\left(P_1 e^{ikz_2} - P_2 e^{ikz_1}\right)}{2\sin\left[k\left(z_1 - z_2\right)\right]}, \tag{3.1}$$

$$A_r = \frac{i\left(P_2 e^{-ikz_1} - P_1 e^{-ikz_2}\right)}{2\sin\left[k\left(z_1 - z_2\right)\right]}, \tag{3.2}$$

$$B_t = \frac{i\left(P_3 e^{jkz_4} - P_4 e^{jkz_4}\right)}{2\sin\left[k\left(z_3 - z_4\right)\right]}, \tag{3.3}$$

and

$$B_r = \frac{i\left(P_4 e^{-ikz_3} - P_3 e^{-ikz_4}\right)}{2\sin\left[k\left(z_3 - z_4\right)\right]}, \tag{3.4}$$

where z_{1-4} correspond to the locations of the 4 measured pressures and k is the wavenumber, ω/c, with ω being the angular frequency of the sound waves and c the sound speed in air. From these

plane wave coefficients, the pressure, P, and velocity, V, on both sides of the panel can be obtained as follows

$$P_0 = A_i + A_r \quad , \tag{3.5}$$

$$V_0 = \frac{A_i - A_r}{\rho_a c} \quad , \tag{3.6}$$

$$P_h = B_t e^{-ikh} + B_r e^{ikh} \quad , \tag{3.7}$$

and

$$V_h = \frac{B_t e^{-ikh} - B_r e^{ikh}}{\rho_a c} \quad , \tag{3.8}$$

where h is the thickness of the panel and ρ_a is the ambient air density. The subscripts 0 and h here denote the corresponding parameters on the left and right sides of the panel, respectively.

A transfer matrix may be conveniently written to relate the pressure and particle velocity on either side of the panel as follows:

$$\begin{bmatrix} P_0 \\ V_0 \end{bmatrix} = \begin{bmatrix} D_{11} & D_{12} \\ D_{21} & D_{22} \end{bmatrix} \begin{bmatrix} P_h \\ V_h \end{bmatrix} , \tag{3.9}$$

where the elements of the transfer matrix can be determined according to [16], as:

$$\begin{bmatrix} D_{11} & D_{12} \\ D_{21} & D_{22} \end{bmatrix} = \frac{1}{P_0 V_h + P_h V_0} \times \begin{bmatrix} P_h V_h + P_0 V_0 & P_0^2 - P_h^2 \\ V_0^2 - V_h^2 & P_h V_h + P_0 V_0 \end{bmatrix} . \tag{3.10}$$

By assuming a unit amplitude incident wave and an anechoic termination at the downstream termination (i.e., $A_i = 1$ and $B_r = 0$), Eqs. (3.5) to (3.8) can be simplified to give

$$P_0 = 1 + R \quad , \tag{3.11}$$

$$V_0 = \frac{1 - R}{\rho_a c} \quad , \tag{3.12}$$

$$P_h = \tau e^{-ikh} \quad , \tag{3.13}$$

and

$$V_h = \frac{\tau e^{-ikh}}{\rho_0 c} \quad ,$$
(3.14)

where $R = A_r/A_i$ and $\tau = A_r/A_i$ are the plane wave reflection and transmission coefficients. The transmission coefficient of the panel can then be obtained by substituting Eqs. (3.11) to (3.14) into the matrix Eq. (3.9) to yield

$$\tau = \frac{2e^{ikh}}{D_{11} + \dfrac{D_{12}}{\rho_0 c} + \rho_0 c D_{21} + D_{22}} \quad .$$
(3.15)

Hence, the transmission loss (*TL*) of the panel can be obtained as

$$TL = 10 \log \frac{1}{|\tau|^2} \quad .$$
(3.16)

Table 3.1. Relevant dimensions of the single-panel FEM model.

Description of Dimension	Dimension Value
Panel/Tube Height and Width	1 m
Incident and Transmitted Lengths	2 m
Density of Panel	2,180 kg m^{-3}
Young's Modulus of Panel	68x10^9 N m^{-2}
Poisson's Ratio of Panel	0.30
Density of Air	1.21 kg m^{-3}
Speed of Sound in Air	343 m s^{-1}
Plane-Wave Generation Location (Upstream of Panel)	1.5 m
Measurement Location of P_1 (Upstream of Panel), z_1	1.4 m
Measurement Location of P_2 (Upstream of Panel), z_2	1.1 m
Measurement Location of P_3 (Downstream of Panel), z_3	1.1 m
Measurement Location of P_4 (Downstream of Panel), z_4	1.4 m

Before we discuss the sound transmission through a stiffened panel, consider a base model for calculating the transmission loss through a panel with different kinds of elastic supports. In the coordinate system where the tube is oriented along the *z*-axis, the center of the

tube is located at $x = y = 0$ and the tube's width and height are each 1 meter along the x- and y-axes, respectively. The panel was located at $z = 0$, and the model was terminated at $z = 2$ and $z = -2$ m on each side. The dimensions and material properties used in the control model are listed Table 3.1.

While local stiffening of the panel can generate non-plane waves, they do not contribute to the measured pressures since they do not propagate at the frequencies considered here. The non-planar waves create a near-field close to the panel which may, however, affect the panel natural frequencies through mass loading effects.

The model was formed using two volume elements comprising the upstream and downstream elements of the tube. The model was meshed with a 0.1 m element size in most cases. In the situations that required finer resolution in the panel, a 0.05 m mesh was used. All models were meshed using a mapped square/cubic geometry, where all faces and edges of all elements were of equal-length and at right-angles to each other. At 150 Hz, the wavelength of air is 2.28 m; there would thus be 22 complete elements per wavelength at the highest frequency, thus allowing for adequate resolution in the FEM model.

All FEM modeling was implemented in ANSYS (1992) using standard element types. In most situations, the simplest possible elements were used to model a particular physical property: unless specified otherwise, similar element types should provide comparable results. The panel was modeled as a shell using the ANSYS SHELL63 element type. Shell elements occupy no space in the geometry of the model, while still accounting for the relevant properties of the panel. The only real constant specified for the shell element was the panel thickness. A damping of 2 percent was assigned to the motion of the panel elements. The shell elements were formed on the faces where the two volumes of the upstream and downstream elements of the tube meet due to

ANSYS-imposed restrictions on fluid elements that two adjacent fluid-coupling elements cannot share a face. Thus, the panel consists of two half-thickness plates coupled together (although occupying the same space). This approach creates a response identical to that of a full-thickness plate while conforming to the requirements of the fluid-structure element coupling. For the control model with clamped edge constraints, the points along the edge of the panel were restrained in all degrees of freedom: i.e., neither rotation nor displacement was allowed at the panel edges.

The fluid surrounding the plate was modeled using the ANSYS FLUID 30 element type. The fluid-structure coupling option was used to model the layer of elements nearest to the panel that allows for deformation of the elements. However, no other fluid elements were assigned this coupling option in the ANSYS model. Anechoic ends in the tube were modeled by using a process described by Khan (2002) for non-spherical infinite ends. This method allows for nearly-anechoic ends on a flat plane so as not to sacrifice the simple structure of the model. In fact, the anechoic ends on both the incident and transmitted sides of the model were created by specifying perfect absorption with the damping factor set at 1.0 in the elements at the inlet and outlet of the model. An impedance flag is also needed at the far end (on the face of the volume) to ensure that ANSYS calculates the energy losses associated with the absorption in the fluid elements.

Plane-wave pressure was generated in the model by specifying a unit pressure degree-of-freedom at all fluid nodes at $z = -1.5$ m. This approach generates waves propagating both towards the panel and towards the far end at the outlet. Anechoic ends were also specified in the ANSYS model to prevent unwanted reflections from the inlet and outlet.

The predicted transmission loss spectrum of the control model is shown as a dark solid line (marked as control) in Fig. 3.2. The predicted results are shown from 1 Hz to 150 Hz.

Beyond 150 Hz (not shown in the figure), the transmission loss follows a generally increasing trend with frequency, as expected from the mass law. However, the clamping of the panel around its edges allows panel modes to occur which can result in decreased transmission loss at the modal natural frequencies.
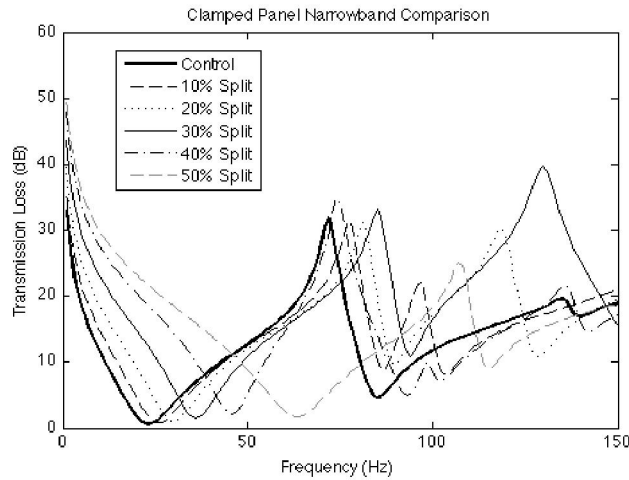
Fig. 3.2. Narrowband transmission loss for select clamped split-panel configurations.

The modal resonant frequencies of a rectangular panel supported with general boundary conditions are well known, (Li and Yu, 2009). It can be expected that the transmission loss will be reduced near the modal natural frequencies that can couple with the incident sound field. The present model matches theoretical predictions, with the first drop in transmission loss occurring at 23 Hz, which is the frequency of the (1,1) mode of the panel. The next 'dip' in the transmission loss is at 85 Hz, which is just below the 86 Hz (1,3)+(3,1) mode of the panel. The slight decrease in frequency is due to fluid loading on the plate. The third transmission loss minimum occurs near the (3,3) mode of vibration of the panel at 144 Hz.

Only the odd modes of vibration, i.e., those exhibiting a net change in volume, showed reductions in transmission loss. The (2,1) or (2,2) resonance frequencies do not appear, as those modes cannot couple with the incident or transmitted plane waves. While, in principle, the latter

64

behavior will only be seen in a tube structure that limits the incident waves on the panel to normally-incident plane waves, the experimental results presented later in the paper show that this finding is also applicable to random-incidence sound waves at low frequencies.

The peaks in the transmission loss above the first resonant frequency are the result of anti-resonances in the system. The explanation provided by Mulholland and Lyon (1973) is that this behavior is caused by non-transmitting modes of vibration: i.e. modes having no net volume displacement which therefore cannot couple with the incident sound field. It would be possible to use the control model to consider the effect of other general boundary conditions, e.g. simply-supported. However, the findings in those cases are rather similar to earlier work shown in Chapter 2 and these results will not be repeated here.

3.3 The predicted transmission loss of a split window
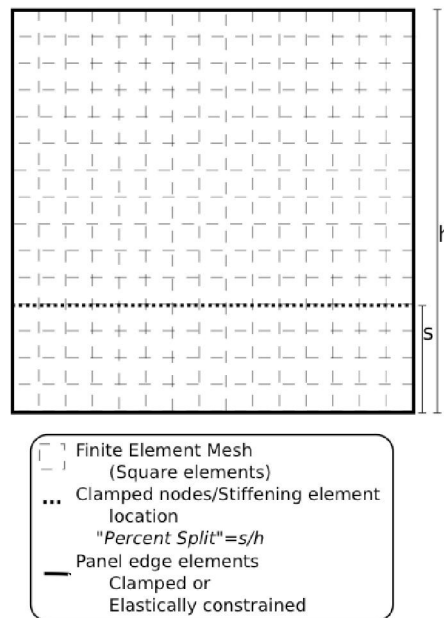
Fig. 3.3. Schematic of finite element mesh show square mesh across panel and clamped.

Several methods were implemented in the model to explore the effects of beam stiffening of a

window. Initials tests were performed by clamping the nodes that lie along a specified location for panel stiffening, as indicated schematically in Fig. 3.3. This represents an ideal constraint to both the translational and rotational response of the panel at the clamped location. Nodes located at 5 percent to 50 percent of the panel height were clamped across the panel in 5 percent height increments; symmetry in the panel dictates that clamping along the width of the panel above 50 percent of the panel will yield identical results to these tests.

Stiffeners were also modeled as beams placed across the panel to simulate a more realistic, non-infinite stiffening of the panel. This was achieved by placing beam elements between the plate nodes at the stiffening locations. The stiffness of the beam was specified by changing the elastic modulus value of the material used in the beam. With a unit moment of area I, a change of the parametric value of Young modulus, E, is equivalent to specifying the bending stiffness, EI, for the beam. The beam was modeled as massless because of the differences in beam construction that would allow for different moments of inertia with different masses.

To simulate elastic edge stiffness, nodes along the edge of the panel were attached to elastic elements; the fixing of those elements to a point in space provides elastic constraint to edge motion. These elastic elements provided both transverse and rotational restraint at the plate edges, but no damping was included in these elements. A uniform stiffness was applied along the entire perimeter of the rectangular panel in each case considered.

The narrowband transmission loss spectra for models clamped at intervals of 10% panel height are shown in Fig. 3.2 together with the predicted results of the control model. Each model exhibits a decrease in transmission loss at the resonance frequency of each section of the panel. The clamping of the panel isolates the vibration between the two segments produced by the split. Each panel segment then exhibits its own resonances in accord with the geometry of the panel

segment. A smaller split in the panel causes the panel segments to be of increasingly disparate size, which separates the resonances of each panel segment further. Since each segment is smaller than the unclamped panel, each will have reduced sound transmission at low frequency. When combined with a shift in resonance frequencies, this mechanism will increase the transmission loss. However, at a 50 percent split, each panel has the same resonance, which does not effectively reduce sound transmission. Similar effects occur with other nearly-equal segment sizes (seen in the 40 percent split, for example).

To illustrate this point, the mean transmission loss averaged from 1 Hz to 150 Hz for all stiffening heights is shown in Fig. 3.4. The simulated data show that for the frequency range considered, the 30 percent split provides the best balance between the reduction of individual panel segment sizes and the separation of the resonance frequencies, as evidenced by the high average transmissions loss. Optimization of the panel split height to maximize transmission loss was not performed, but the data would indicate that the ideal split height would be between 25 and 30% of the panel height for the window geometry and frequency range considered here.
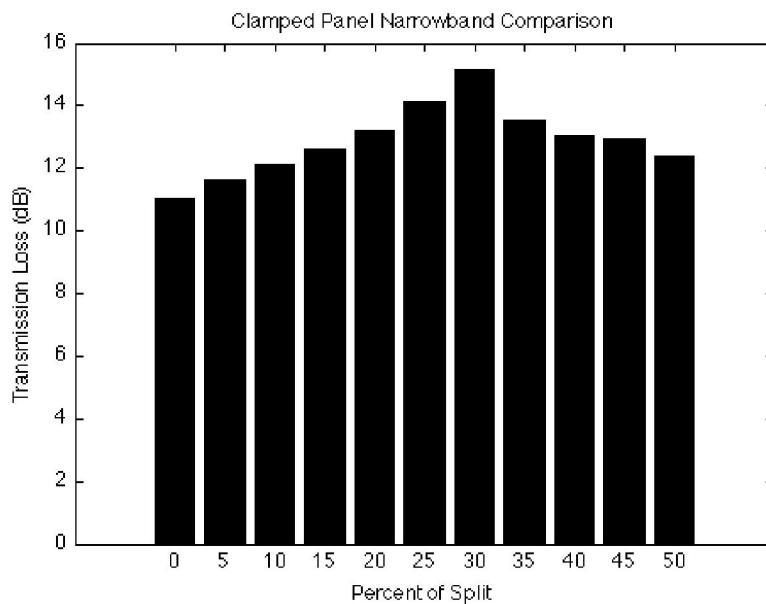
Fig. 3.4. Mean transmission loss averaged from 1 Hz to 150 Hz for clamped, split-panel configurations of a window.

67
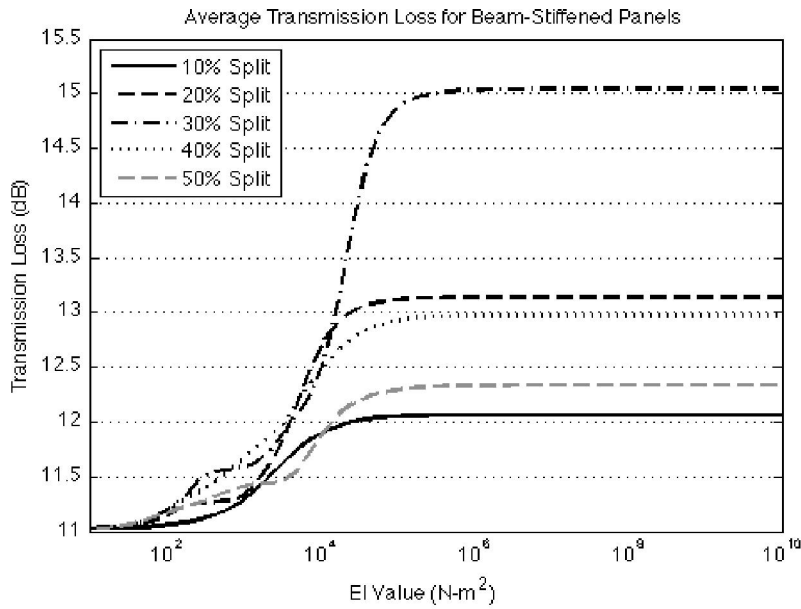
Fig. 3.5. Variation of mean transmission loss with the split height and bending stiffness of the beam.

The mean transmission loss results from models with solid stiffening beams across the panels are shown in Fig. 3.5. The abscissa is the bending stiffness (*EI*) of the stiffening element, while the ordinate is the mean transmission loss from 1 Hz to 150 Hz. The most significant feature in the plot is that a constant transmission loss is reached after a bending stiffness (*EI*) of 10^4 to 10^5 N m^2 is reached. The exact *EI* value at which the transmission loss becomes constant is dependent on the height of the stiffening element within the panel. This result indicates that the stiffening effects seen in clamped panels are obtainable at non-infinite values of panel stiffness, even though coupling between the two sections of the panel is present in these cases. Below the transition to a constant transmission loss, each split has its own characteristic, and different splits could be more effective than the 30 percent split at lower stiffnesses. A sample narrowband plot of transmission loss variation with the bending stiffness of the beam for stiffening elements at 30 percent of the panel height is shown in Fig. 3.6.

68
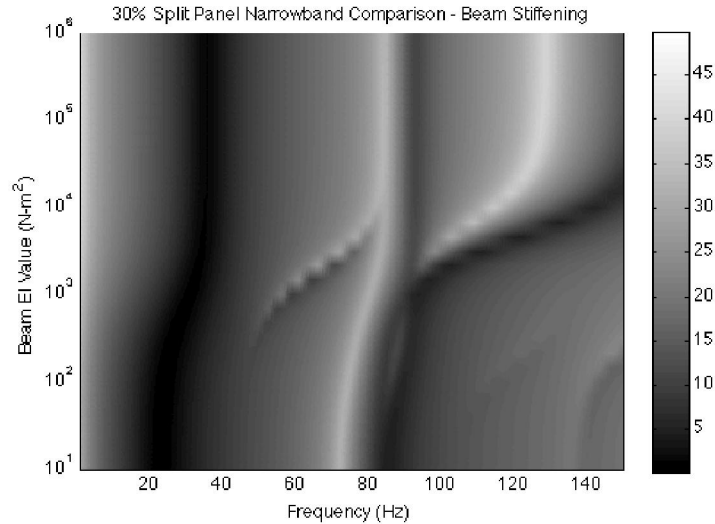
Fig. 3.6. Narrowband transmission loss for beam stiffness with a 30 percent panel split.

The mean transmission losses for elastically-mounted panels are shown in Fig. 3.7. The abscissa is the translational stiffness of the edge and the ordinate is the rotational stiffness around the edges. The mean transmission loss of the elastic edge configurations is nearly constant when the translational stiffness is low. This suggests that plate translational motion has much more effect on transmission of sound through panels than does the rotational motion at the edge. At higher translational stiffnesses when the plate edges are effectively fixed, low rotational stiffness leaves the panel pinned, and increasing the rotational stiffness is similar to applying a clamped condition and increases the transmission loss accordingly. The increase in rotational stiffness will then restrict the motion of the panel to its central region, while the opposite case (high rotational stiffness and low translational stiffness) still allows for high plate translational amplitude. A translational edge stiffness of approximately 10^6 N/m shows the most dramatic effect on average transmission loss. Thus, if the stiffness of the window mounting is too low, the window transmission loss can be reduced by as much as 3 dB compared to a fully clamped support.

69
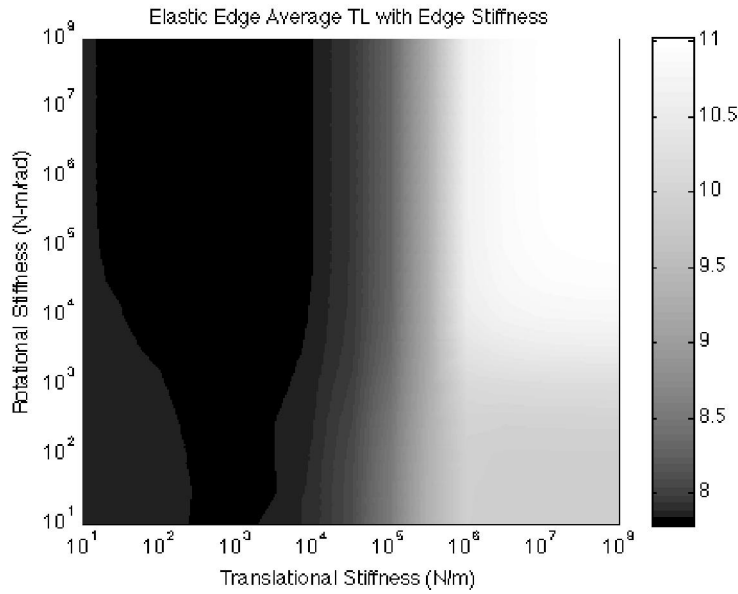
Fig. 3.7. Variation in mean transmission loss with the translational and rotational stiffness.

3.4. Experimental results

Previous experimental work on sound transmission through panels has been focused primarily on the effects of window edge-clamping. The addition of damping or restriction of the edge motion has been shown to reduce panel transmission loss. Utley and Fletcher (1969; 1973) performed experimental measurements on windows to gauge the effects of edge conditions on the transmission loss of single and double panel windows. They found that gasketing windows with a high-damping material increased their transmission loss beyond that provided by low-damping gasketing. Quirt (1982) performed measurements on single- and double-pane windows to experimentally gauge the effects of various properties on sound transmission. His results showed good comparisons with mass-law predictions except at low frequencies below about 100 Hz. Both Utley and Quirt's results were presented in third-octave bands down to 80 Hz, obscuring the influence of resonance frequencies on the transmission loss. Xin and Lu (2009)] derived analytical expressions for the transmission loss of finite, double panel configurations with either

70

simply-supported or clamped boundary conditions. They ran experimental tests on a similar setup in a custom mounting rig allowing for both conditions. The narrowband results of the analytical model and experimental results for normal sound incidence compared well, but results for oblique incidence did not agree as well.

In order to validate the FEM models described in the last two sections, indoor laboratory experiments were performed on an elastically-mounted panel system. A series of experiments was designed to allow for elastic panel mounting. Measurements of the sound transmission loss of a rectangular panel with elastic mounting were performed in a reverberation room.

The reverberation room had dimensions of 7.6 m by 6.1 m by 5.5 m and a volume of about 190 m^3 creating an indoor space for diffuse sound fields with a cut-off frequency of about 100 Hz. Transmitted sound pressure was measured outside the reverberation room in a temporary semi-anechoic space composed of three panels of sound-absorbing material surrounding any measurement equipment outside the reverberation room. A pair of Altec N1201-8A speakers was positioned near the center of the reverberant room to produce the diffuse sound field. The interior pressure inside the semi-anechoic space was measured using a Brüel and Kjaer (B&K) 4189 microphone and B&K 2619 preamp mounted on a boom. The microphone was powered by a B&K 5935 power supply situated outside the room. A General Radio 1390-A Random Noise Generator was used to produce a white noise signal to be supplied to the speakers within the reverberation room. The generator produced a signal from 0 Hz to 20 kHz, which was then band-pass filtered from 20 Hz to 2 kHz by using a Wavetek 852 filter set. The filtered signal was monitored in the data acquisition system. The signal was then amplified by using a SC Audio 1080 Stereo Amplifier and was fed to the speakers inside the reverberation room. A schematic

diagram of the experimental setup is shown Fig. 3.8(a), and a photograph of the equipment used

inside the reverberation room is shown in Fig. 3.8(b).
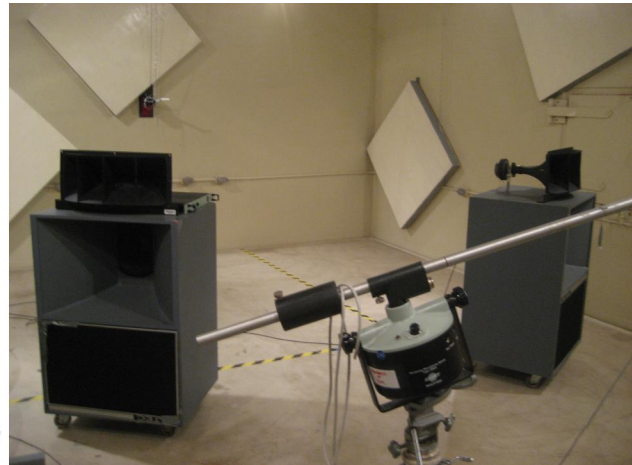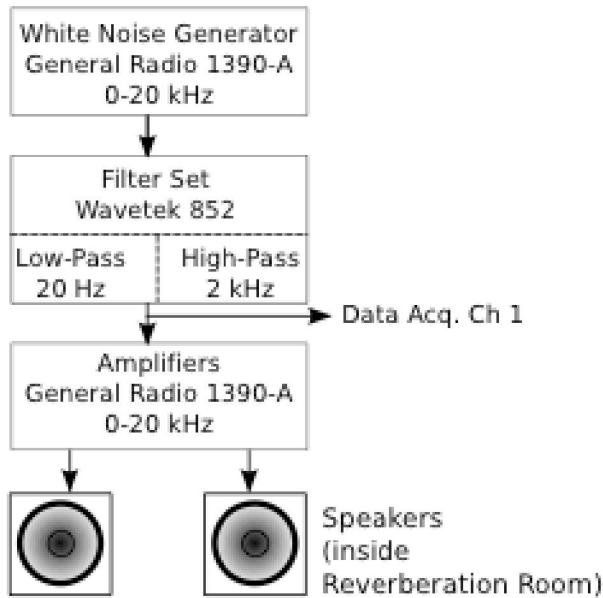
(a) Schematic diagram   (b) Photograph for equipment used

Fig. 3.8. Experimental set up of the study.

The reverberation room has a square aperture of size 1.21 m by 1.21 m which was

designed to hold panels for measurement of sound transmission loss. An adapter was installed in

the port in order to allow for testing of the sound transmission specifically associated with lower-

order modes of a plate. The adapter consisted of a wooden structure filled with sand so as to

provide adequate mass to reduce sound transmission through the structure. This arrangement

reduces the available aperture dimension down to 30 cm square, in which appropriate-sized

panels were installed for the experiments. Due to the limitation on the size of the reverberation

room and the aperture, and because of relatively high levels of low frequency background noise,

accurate results could only be obtained at frequencies above 100 Hz. In the present study, lightweight panels that can be fitted into this port have their first resonant frequency in the range of 180-230 Hz when clamped at their edges.

The panel was mounted in the adapter by using an aluminum frame that screwed directly into the port. Panels to be tested in this configuration were cut to 28.6 cm square to allow for 6.4 mm of the panel material to be clamped between the aluminum frame and the wooden port adapter. Elastic mounting could be achieved by placing lower-density materials such as foam along the 6.4 mm border on both sides of the panel.
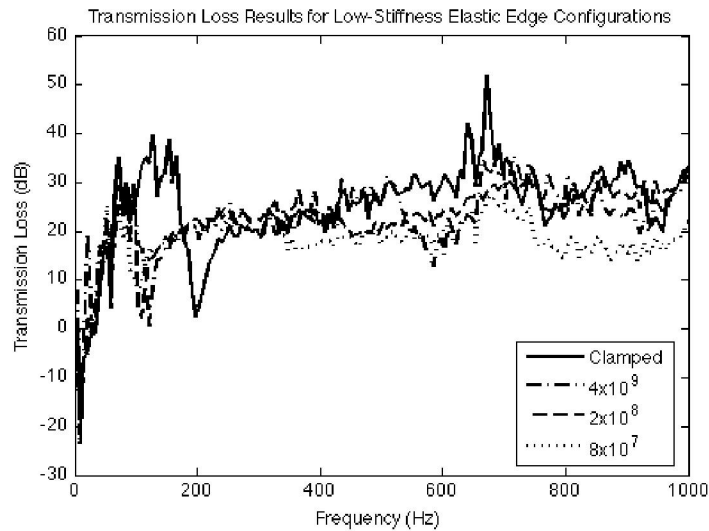
Fig. 3.9. Transmission loss of lower-stiffness elastic mounting conditions. Elastic mounting material stiffness [N/m^2] is given by the manufacturer.

A total of seven unique panel configurations were tested. The plate used in all configurations was 2 mm thick aluminum T-6061 alloy. Six different elastic mounting configurations were tested along with a control, clamped-like condition. The variation in each configuration was in the elastic mounting material used around the plate: a total of 6 different mounting stiffnesses were used. The material used for mounting stiffness control was Getzner Sylomer and Sylodyn foams, which are designed for vibration isolation of floor panels or machinery. The Sylodyn foam is a low-damping variation of the Sylomer material, but for the

purposes of this experiment only the stiffness properties of the foam were significant. A material thickness of 6 mm was used to provide the resilient edge support.
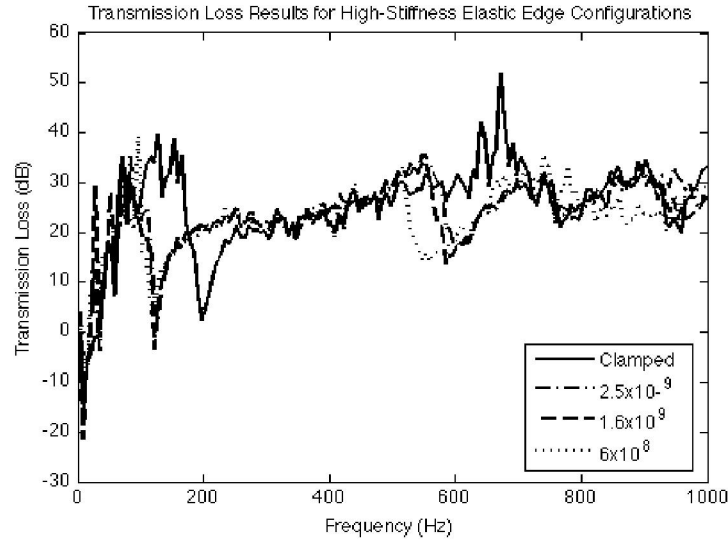
Fig. 3.10. Transmission loss of higher-stiffness elastic mounting conditions. Elastic mounting material stiffness [N/m^2] is given by the manufacturer.

The measured TL spectra for all the configurations are shown in Figs. 3.9 and 3.10. Note that the results below 100 Hz should be disregarded since they were entirely determined by background noise levels. The major difference in the TL of each panel configuration occurs near the natural frequencies of the configuration. The sharp decreases in TL occur close to the natural frequencies of the (1,1) and (3,1) modes in each panel configuration: i.e., near 100 Hz and 500 to 600 Hz, respectively. The modes of vibration are more pronounced in the higher-stiffness configurations shown in Fig. 3.10: the (3,1) mode cannot be distinguished in the cases of the two lowest-stiffness foams shown in Fig. 3.9. This could be due to significant damping provided by these foams.

A finite element model was created to simulate the smaller panel size combined with the elastic edge stiffness. The numerical model was similar to that described earlier, but accounted for the smaller size of the experimental setup. The panel thickness and material were adjusted to

74

match the panel tested, and all other geometrical parameters were scaled down to maintain a similar geometry with a 0.273 m panel size.

Numerical results from this model were compared with experimentally-obtained results of the transmission loss of the panel. In this analysis, the input translational stiffness was adjusted to provide a best fit between the FEM model results and experimental data. A sample comparison of experimentally-obtained data and TL spectrum calculated using the FEM model is shown in Fig. 3.11.
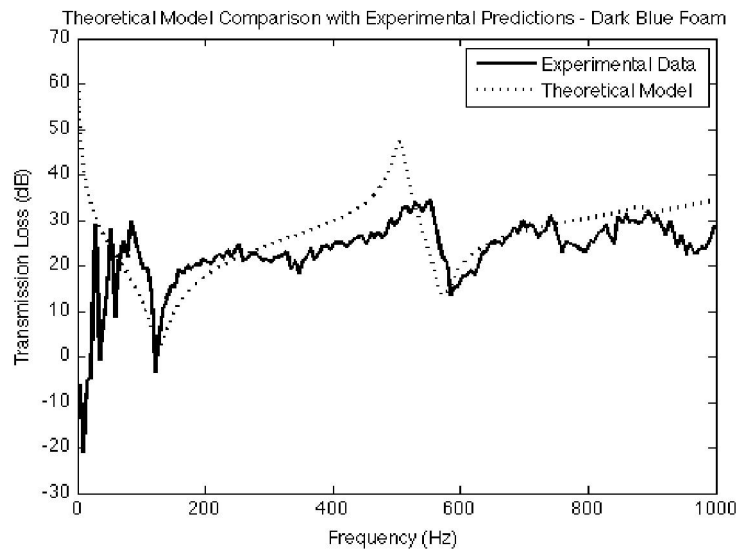
Fig. 3.11. Comparison of experimental data with theoretical predictions for dark blue Sylomer T foam. Estimated material stiffness: 1.6×10^9 N/m^2.

The predicted results including the elastic edge support fit sufficiently well with the experimental results to verify that the important elements of the TL (in a long duct with anechoic terminations) discussed in Sec. 3.2 appear in practice for the TL in a reverberation rooms with diffuse sound field. The decrease in TL at the (1,1) and (3,1) natural frequencies is clearly seen in most of the data. The disparity between the fit of the (1,1) peak and the (3,1) peak could be due to mounting inconsistencies; it was found during repetitions of testing that the (3,1) peak is much more sensitive to re-mounting than was the (1,1) peak.

75

Tests of elastically-mounted panels produced experimental results similar to those predicted by the FEM formulation for a long duct. The odd modes of the panel were observed to transmit the majority of the sound, even under random incidence excitation, though decreased edge stiffness reduced the transmission loss decreases caused by higher-order modes. Finally, the predictions of the FEM model showed a good fit with the experimentally obtained data in the in the region of the lower natural frequencies of the configuration.

3.5   Conclusions

Numerical simulations suggest that stiffening elements added to a panel can cause a significant increase in average sound transmission loss at low frequencies. The addition of stiffening elements increases the natural frequencies of the modes of vibration of the panel, and in cases of high stiffening, they effectively split the panel into two smaller segments, each of which exhibits modes of vibration at frequencies higher than for the original panel. Thus splitting the panel tends to increase sound transmission loss. However, for splits that yield two panel segments of nearly equal size, this increase was not seen as both panels have high radiation at the same frequency. The FEM model showed that a split at 30 percent of the height of the panel provided the best balance between shifted natural frequencies and reduction of panel size, and gave the highest average transmission loss from 1 Hz to 150 Hz, with an increase of 4 dB from the non-stiffened panel.

The addition of elastic edge mounting to plates reduces the natural frequencies of the panel configuration. In extreme cases, particularly with low rotational stiffness, the mode shapes can change significantly. These changes in mounting stiffness can cause as much as 3 dB decrease in the transmission loss of typical window configurations.

Experimental testing on elastically-mounted panels showed the predicted effects, with lower natural frequencies found in the cases of elastic edge mounting of lower stiffness. The sound transmission at non-resonant frequencies was not dependent on the mounting stiffness, but the resonance of the modes of vibration of the plate caused low transmission loss regions. Numerical simulation results obtained using the FEM model agreed well with experimental results, despite the difference in incident sound field type in the simulation and experiment.

References

ANSYS user's manual for revision 10.0. Houston, PA: Swanson Analysis Systems, Inc., 1992.

N. Atalla, J. Nicolas, C. Gauthier, 1996. "Acoustic radiation of an unbaffled vibrating plate with general elastic boundary conditions," *Journal of the Acoustical Society of America* **99**, 1484-1494.

A. Berry, 1990. "A general formulation for the sound radiation from rectangular, baffled plates with arbitrary boundary conditions," *Journal of the Acoustical Society of America* **88**, 2792-2802.

M. S. Khan, C. Cai, K. C. Hung, 2002. "Acoustics field and active structural acoustic control modeling in ANSYS," *ANSYS International Conference Proceedings*, Singapore.

J. H. Lee, J. Kim, 2002. "Analysis of sound transmission through periodically stiffened panels by space-harmonic expansion method," *Journal of Sound and Vibration* **251**, 349-366.

D. J. Mead, 1975. "Wave propagation and natural modes in periodic systems: 1. Mono-coupled systems," *Journal of Sound and Vibration* **20**, 1-18.

D. J. Mead, 1990. "Plates with rectangular stiffening in acoustic media: Vibration and radiation," *Journal of the Acoustical Society of America* **88**, 391-401.

K. A. Mullholland, R. H. Lyon, 1973. "Sound insulation at low frequencies," *Journal of the Acoustical Society of America*, **54**, 867-878.

D. M. Photiadis, 1992. "Anderson localization of one-dimensional wave propagation on a fluid loaded plate," *Journal of the Acoustical Society of America* **91**, 771-780.

J. D. Quirt, 1982. "Sound transmission through windows I. Single and doubling glazing," *Journal of the Acoustical Society of America* **73**, 834-844.

B. H. Song, J. S. Bolton, 2000. "A transfer-matrix approach for estimating the characteristic impedance and wave numbers of limp and rigid porous materials," *Journal of the Acoustical Society of America* **107**, 1131-1152.

W. A. Utley, B. L. Fletcher, 1969. "Influence of edge conditions on the sound insulation of windows," *Applied Acoustics* **2**, 131-136.

W. A. Utley, B. L. Fletcher, 1973. "The effect of edge conditions on the sound insulation of double windows," *Journal of Sound and Vibration* **26**, 63-72 (1973).

J. Wang, T. J. Lu, J. Woodhouse, R. S. Langley, J. Evans, 2005. "Sound transmission through lightweight double-leaf partitions: theoretical modeling," *Journal of Sound and Vibration* **286**, 817-847.

F. X. Xin, T. J. Lu, 2009. "Analytical and experimental investigation of transmission loss of clamped double panels: implication of boundary effects," *Journal of the Acoustical Society of America* **125**, 1506-1517.

4. Transmission of low-frequency noise through double-pane windows

4.1 Introduction

Mitigation of increasing levels of low-frequency noise (LFN) pollution requires more and better acoustic insulation of buildings. This insulation design depends on several components, and the component with the highest transmission rate dominates. Windows are usually the components most conducive to sound transmission, especially at low frequencies. Among the designs to increase the acoustic insulation performance of windows, the multi-pane window with a gas-filled cavity is the most common, practical, and economical. To design such windows, simple but accurate models have to be built for the calculation of sound transmission in complex fluid-solid systems.

In this chapter, a theoretical study for the transmission of LFN through a double-pane window mounted on a rigid wall are presented. A hybrid approach based on the finite element (FEM) and boundary element (BEM) formulations are examined. It is well-known that the FEM (Criag, 1977) is ideal for modeling elastic structures within a finite structure. However, BEM formulation (Chiello et al., 2003) is suitable for evaluating the propagation of sound in both finite and infinite gas media. In the numerical model developed in this chapter, FEM is used to model window panes, whereas BEM is applied to model the gas-filled cavity between the window panes and the corresponding gas medium in the source and receiving regions. The interaction between the gas medium and the structure is incorporated by introducing appropriate coupling conditions.

The stiffness matrix in FEM is adjusted by the technique of component mode synthesis (Criag 1997; Chiello et al., 2003). This permits a straightforward inclusion of window mounting

conditions, i.e., the visco-elastic boundary support for the window pane from its wooden frame can be incorporated.

The development of an iteration scheme to obtain numerical solutions to the coupled FEM/BEM equations is also discussed in this chapter. The iteration method is introduced to avoid solving the coupling matrix equations for double-pane windows. In fact, this iteration method can be easily extended to the problem of a triple-pane window.

4.2 Literature review

In the past 40 years, there has been a sustained interest in studying the response of a double-panel structure subjected to acoustic excitations in a compressible fluid medium. Among the previous simulation models of a double-panel structure, we can divide them into 3 categories.

One of them, known as the impedance-transfer method, is based on an impedance approach. Among the previous studies, one of the earliest models was introduced by Beranek and Work (1949). There was a shortcoming in their study because the bending stiffness of individual panels was not considered. In another study, London (1950) introduced a real part to the panel impedance in his progressive-wave model. However, London's model was restricted to double panels with an empty cavity, which is generally not a good assumption in practice. In these two studies, the mounting wall of the double-pane windows was assumed to be infinite in size, which could not be true or appropriate for the analysis of most windows commonly found in residential structures. The concept of the impedance-transfer method was also used by Mulholland et al. (1968) for an oblique angle of incidence. However, only empty cavities were considered in this study. Fahy (1985, 2001) presented two models for uncoupled double walls. The benefit of his models was that the lowest normal modal frequency of the panel was considered in the analysis.

The second category is based on the statistical energy analysis (SEA) method. White and Powell (1966) used the statistical mechanical approach (Lyon and Maidanik, 1962) to tackle the problem of a double-panel structure. The most obvious flaw in this early model was that White and Powell did not consider the cavity thickness in their analysis. In the late 1960s, Crocker and Price (1969, 1970) applied the SEA technique to a numerical study of a double-wall structure. Resonant and non-resonant transmission coefficients were considered separately in their model. The Crocker and Price model introduced considerably more parameters than earlier models, and their equations were relatively more complicated. However, Crocker and Price ignored the mass-air-mass resonant effect in their model. Craik (2003) improved the SEA method by computing the loss factor for the non-resonant coupling between a room and a cavity. Later, he and his co-workers developed a simple model, which predicted the transmission of vibration through a double-leaf partition.

The third category is based on coupled FEM/BEM. Kang and Bolton (1996) presented a finite element model by coupling a foam lining (elastic porous material) with the structural elements. They concluded that the constraint conditions at the edges of both the foam lining and the facing panels had a significant effect on the normal-incidence sound transmission loss (TL) of the double-panel system at low frequencies. Sgard et al. (2000) discussed the prediction of low-frequency transmission loss (TL) through double-wall sound barriers with elastic porous linings using an approach based on a finite element model. The different layers of the sound barrier were coupled to a variational BEM technique to account for the effect of fluid loading. They also performed parametric studies of the septum mass, the decoupling porous layer properties, and the multi-layer mounting conditions. Langer and Antes (2003) presented an

81

FEM/BEM model similar to that of Kang and Bolton (1996) using air instead of foam inside the cavity. However, they did not include the effects of mass-air-mass resonance in their study.

The models in the first two categories (the impedance approach and the SEA method) are suitable for the high frequencies because typical assumptions are used such that some factors in the low-frequency domain were ignored. These factors include the boundary conditions of the edges, the size of the panels, and the cavity thickness between the panels. These factors are critical for analysis in the low-frequency regime. Donato (1972) and others (Cummings and Mulholland, 1968) pointed out that the size of a specimen was important at low frequencies where the resonance of panels dominates the shape of the TL spectrum. Utley and Fletcher (1973) investigated the edge conditions of double-pane windows. Two methods of mounting were used and compared. It was shown that a resilient mounting gasket for the glass produces a greater TL than conventional mounting. The importance of including the general boundary conditions in the modeling was confirmed in the Utley and Fletcher study.

The coupled FEM/BEM approach is good for low-frequency analysis. The full FEM/BEM model presented in this chapter uses a different approach from the previous FEM/BEM models: BEM is used instead of FEM for modeling the cavity inside a double-pane window. In this approach, the effects of cavity thickness, mass-air-mass resonance, and sound field pressure in the cavity can be included in the numerical modeling in the low-frequency regime.

The cavity between double panes plays an important role for the acoustic performance of the sound insulation for double-pane windows. London (1950) found that for double walls with air-coupling, very shallow airspaces can produce appreciable increases in TL over a single wall. Mulholland and his co-workers (1968, 1973) presented two models where the lateral sound

propagation in the cavity was taken into account. They concluded that the low-order modes or resonant frequencies of the in-plane sound fields in the cavity dominate the shape of TL spectrum. It is also well known that the pressure and dynamic behavior of the sound field inside the air cavity between double panes are important for active control or feedback control of the sound transmission through double-pane windows. Active control of sound transmission through double-pane windows was presented by Kaiser et al. (2003), Cheng and Li (2006), and Jakob and Moser (2003).

For the transmission of LFN through double-pane windows, the structural properties including stiffness, thickness, and other elastic properties are important for the analysis of the dynamic response of the window panes. More importantly, the sound fields inside the window cavity are significant and cannot be ignored as in the case which assumes an empty (vacuum) cavity.

4.3 Exact-coupled FEM/BEM formulation

A baffled window is immersed in a gas medium excited by acoustic disturbances from the upper medium V_1, and the receiver is located in the lower medium V_2 of an otherwise quiescence environment. To model the double-pane window, we assumed that it is a set of two thin rectangular panels (the one adjacent to V_1 as Panel 1 and the other as Panel 2), which was placed in an infinite-plane rigid baffle, S. The upper and lower surfaces of Panel 1 are denoted as S_1 and S_2, respectively. Similarly, S_3 and S_4 are used to denote the upper and lower surfaces of Panel 2. The normal directions of the surfaces S_i (where $i = 1, 2, 3, 4$) are denoted by n_i, and the respective surface pressures are represented by p_i. Figure 4.1 shows the details of the geometry and variables of a double-pane window.
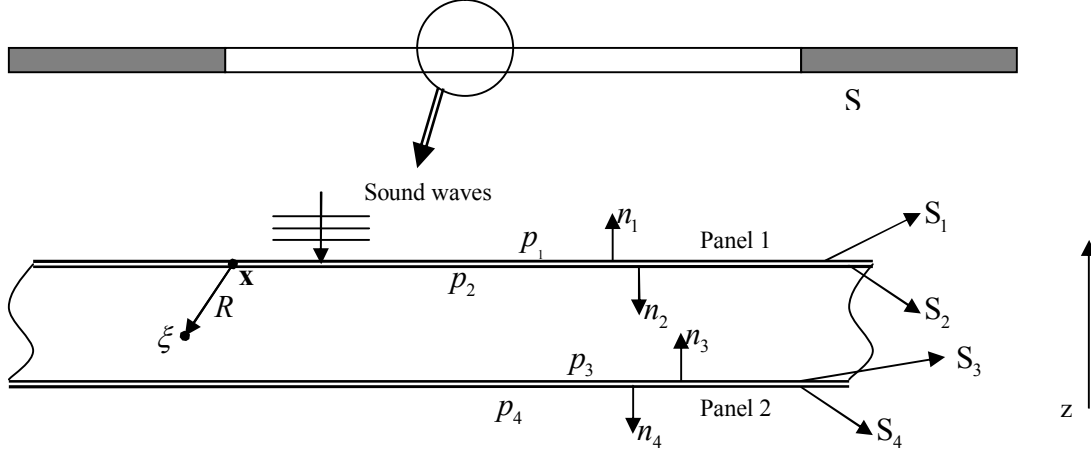
Fig. 4.1. Geometrical configuration of a double-pane window.

A rectangular elastic panel can be divided into a number of identical units where each finite element has length a and width b. Suppose that there is a total of Q elements in the elastic panel. The deflection at the center of each finite element can be assembled to form a row matrix $\{\mathbf{d}\}$, which can be used to approximate the deflection of the elastic panel. By applying Hamilton's principle [see, for example, Sodel (2005)], it is possible to obtain a set of global matrix equations linking the deflection $\{\mathbf{d}\}$ with the acoustic excitation $\{\Delta\mathbf{P}\}$ by

$$\{\mathbf{d}\} = \{\mathbf{H}\} \times \{\Delta\mathbf{P}\}, \tag{4.1}$$

where the overall stiffness matrix $\{\mathbf{H}\}$ is defined as

$$\{\mathbf{H}\} = (ab) \times \{\mathfrak{R}\} \times \left[\{\mathbf{C}\} + \{\mathbf{S}\}\right]^{-1} \times \{\mathbf{T}\}. \tag{4.2}$$

The overall stiffness $\{\mathbf{H}\}$ is dependent on the physical properties of the elastic panel, which includes its mass $\{\mathbf{M}\}$, damping $\{\mathbf{D}\}$, and stiffness $\{\mathbf{K}\}$ as well as the angular frequency ω of the acoustic excitations such that

$$\{\mathbf{C}\} = -\omega^2 \{\mathbf{M}\} + i\omega\{\mathbf{D}\} + \{\mathbf{K}\}. \tag{4.3}$$

84

The second term in the square bracket of Eq. (4.2), $\{\mathbf{S}\}$, is the stiffness matrix of the visco-elastic supports along the edge of the elastic panel. The matrix $\{\mathbf{T}\}$ is the transformation matrix between the force at the center of the element and its equivalent nodal forces. The matrix $\{\mathfrak{R}\}$ is a global transformation matrix converting the nodal displacement vectors to the corresponding central displacement vectors. Here in Eq. (4.2), $\{\mathbf{d}\}$ and $\{\Delta\mathbf{P}\}$ are column vectors with Q elements, but $\{\mathbf{H}\}$ is a $Q \times Q$ square matrix.

The acoustic excitations are the net pressure acting on the upper and lower surfaces of the elastic panel. For the double-pane window shown in Fig. 1, the acoustic excitations on Panel 1 and 2 are given, respectively, by

$$\left\{\Delta\mathbf{P}^{(1)}\right\} = \left\{\mathbf{P}_1\right\} - \left\{\mathbf{P}_2\right\} \tag{4.4a}$$

and

$$\left\{\Delta\mathbf{P}^{(2)}\right\} = \left\{\mathbf{P}_3\right\} - \left\{\mathbf{P}_4\right\}. \tag{4.4b}$$

where the superscripts j ($j = 1, 2$) represent the corresponding parameters for Panel 1 and Panel 2 respectively. The matrices, $\left\{\mathbf{P}_1\right\}$, $\left\{\mathbf{P}_2\right\}$, $\left\{\mathbf{P}_3\right\}$, and $\left\{\mathbf{P}_4\right\}$, which are the column vectors of Q elements, are the surface pressure acting on S_1, S_2, S_3, and S_4, respectively. Making use of Eq. (4.1), two sets of matrix equations can be formed for both window panes as follows:

$$\left\{\mathbf{d}^{(1)}\right\} = \left\{\mathbf{H}^{(1)}\right\} \left[\left\{\mathbf{P}_1\right\} - \left\{\mathbf{P}_2\right\}\right] \tag{4.5a}$$

and

$$\left\{\mathbf{d}^{(2)}\right\} = \left\{\mathbf{H}^{(2)}\right\} \left[\left\{\mathbf{P}_3\right\} - \left\{\mathbf{P}_4\right\}\right] \tag{4.5b}$$

In the discretization of the boundary integral equation, all variables are assumed to be piecewise smooth on the boundary surfaces S_1, S_2, S_3, and S_4. It is convenient to choose each

of the elements used in BEM to coincide with that used in FEM. As a result, the BEM formulation for each surface can be written as follows:

$$\{\mathbf{P}_1\} = 2\{\mathbf{P}_0\} - 2\{\mathbf{A}_{11}\}\{\mathbf{d}^{(1)}\}, \tag{4.6a}$$

$$\{\mathbf{P}_2\} = \{\mathbf{A}_{22}\}\{\mathbf{d}^{(1)}\} - \{\mathbf{A}_{32}\}\{\mathbf{d}^{(2)}\} + \{\mathbf{B}_{32}\}\{\mathbf{P}_3\}, \tag{4.6b}$$

$$\{\mathbf{P}_3\} = -\{\mathbf{A}_{33}\}\{\mathbf{d}^{(2)}\} + \{\mathbf{A}_{23}\}\{\mathbf{d}^{(1)}\} - \{\mathbf{B}_{23}\}\{\mathbf{P}_2\}, \tag{4.6c}$$

and

$$\{\mathbf{P}_4\} = 2\{\mathbf{A}_{44}\}\{\mathbf{d}^{(2)}\}, \tag{4.6d}$$

where $\{\mathbf{P}_0\}$ is the vector of the incoming sound pressure acting at the center of each element on the upper surface of Panel 1 because of the incoming sound.

The subscripts used for matrices $\{\mathbf{A}\}$ and $\{\mathbf{B}\}$ are explained in the following paragraph. Nevertheless, the matrices, $\{\mathbf{A}\}$ and $\{\mathbf{B}\}$, are formed by the process of collocation in the boundary integral formulation. Typically, the interaction between two elements l_1 and l_2 on the upper (or lower) surface of the window can be determined according to

$$\mathbf{A}(l_1, l_2) := \rho_0 \omega^2 \int_S G\left(\mathbf{x}_{l_1} \middle| \xi_{l_2}\right) dS \tag{4.7a}$$

and

$$\mathbf{B}(l_1, l_2) := \int_S \frac{\partial G\left(\mathbf{x}_{l_1} \middle| \xi_{l_2}\right)}{\partial n} dS, \tag{4.7b}$$

where ρ_0 is the density of the gas medium, ω is the angular frequency of the incoming sound, and $G\left(\mathbf{x}_{l_1} \middle| \xi_{l_2}\right)$ and $\dfrac{\partial G\left(\mathbf{x}_{l_1} \middle| \xi_{l_2}\right)}{\partial n}$ are Green's function and its derivative, respectively, from the source located at $\mathbf{x}_{l_1}$ and the receiver located at ξ_{l_2}.

In Eqs. (4.6a–d), the subscripts used for the matrices $\{\mathbf{A}\}$ and $\{\mathbf{B}\}$ are defined as follows. Making use of the notations given in Eqs. (4.7a) and (4.7b), we have $A_{ij} = A(l_i, l_j)$ and $B_{ij} = B(l_i, l_j)$, where the source, $\mathbf{x}_{l_i} \in S_i$, and the receiver $\xi_{l_j} \in S_j$. Since the boundary surfaces S_1, S_2, S_3, and S_4 are discretized in the same way, it follows immediately that

$$\{\mathbf{A}_{11}\} = \{\mathbf{A}_{44}\} \equiv \{\mathbf{A}_a\}, \ \{\mathbf{A}_{22}\} = \{\mathbf{A}_{33}\} \equiv \{\mathbf{A}_b\} \tag{4.8a,b}$$

and

$$\{\mathbf{B}_{11}\} = \{\mathbf{B}_{44}\} \equiv \{\mathbf{B}_a\} \ , \ \{\mathbf{B}_{22}\} = \{\mathbf{B}_{33}\} \equiv \{\mathbf{B}_b\} \tag{4.9a,b}$$

for $\mathbf{x}_{l_1}$ and ξ_{l_2} located on the same surface. However, if $\mathbf{x}_{l_1}$ and ξ_{l_2} lie on different surfaces within the window cavity, it can be shown that

$$\{\mathbf{A}_{23}\} = \{\mathbf{A}_{32}\} \equiv \{\mathbf{A}_c\}, \tag{4.10a}$$

and

$$\{\mathbf{B}_{23}\} = \{\mathbf{B}_{32}\} \equiv \{\mathbf{B}_c\}. \tag{4.10b}$$

It is worth mentioning that Green's function for a source/receiver located outside the window cavity is different from that for a source/receiver located inside. Consequently, the matrix $\{\mathbf{A}_a\}$ is different from $\{\mathbf{A}_b\}$ in Eqs. (4.8), and that the matrix $\{\mathbf{B}_a\}$ is different from $\{\mathbf{B}_b\}$ in Eq. (4.9).

Substituting Eqs. (4.8a,b), (4.9a,b), and (4.10a,b) into Eq. (4.6a–d), a more compact form of matrix equations can be obtained to verify,

$$\{\mathbf{P}_1\} = 2\{\mathbf{P}_0\} - 2\{\mathbf{A}_a\}\{\mathbf{d}^{(1)}\}, \tag{4.11a}$$

$$\{\mathbf{P}_2\} = \{\mathbf{A}_b\}\{\mathbf{d}^{(1)}\} - \{\mathbf{A}_c\}\{\mathbf{d}^{(2)}\} + \{\mathbf{B}_c\}\{\mathbf{P}_3\}, \tag{4.11b}$$

$$\{\mathbf{P}_3\} = -\{\mathbf{A}_b\}\{\mathbf{d}^{(2)}\} + \{\mathbf{A}_c\}\{\mathbf{d}^{(1)}\} - \{\mathbf{B}_c\}\{\mathbf{P}_2\}, \tag{4.11c}$$

$$\{\mathbf{P}_4\} = 2\{\mathbf{A}_a\}\{\mathbf{d}^{(2)}\}. \tag{4.11d}$$

To evaluate the sound pressure transmitted through a double-pane window, the surface pressure vectors $\{\mathbf{P}_1\}$, $\{\mathbf{P}_2\}$, $\{\mathbf{P}_3\}$, and $\{\mathbf{P}_4\}$ and the displacement vectors $\{\mathbf{d}^{(1)}\}$ of Panel 1 and $\{\mathbf{d}^{(2)}\}$ of Panel 2 are required. This information may be obtained using Eqs. (4.11a–d) in conjunction with Eqs. (4.5a) and (4.5b) for the boundary surfaces, S_1, S_2, S_3, and S_4. These coupled FEM/BEM equations can then be solved by standard mathematical methods to obtain numerical solutions for the displacement vectors of Panel 1 and Panel 2.

The sound fields on either side of the window can then be obtained from Eqs. (4.11a) and (4.11d) for the known $\{\mathbf{d}^{(1)}\}$ and $\{\mathbf{d}^{(2)}\}$. With the knowledge of the surface pressure at every element of S_1 and S_2, it is possible to evaluate the sound power on both sides of a double-pane window. The sound power of the incident waves on the upper side of the window can be calculated by

$$W_I = (ab)\sum_{q=1}^{Q}\left(\left[\mathbf{P}_0\left(\mathbf{x_q}\right)\right]^2 \middle/ 2\rho_0 c_0\right), \tag{4.15a}$$

where Q is the total number of elements. The power of the sound, W_T, radiated from the vibrating window at the lower surface can be estimated by

$$W_T = (ab)\sum_{q=1}^{Q}\mathrm{Re}\left\{\mathbf{P}_4\left(\mathbf{x_q}\right)\left[-i\omega\,\mathbf{d}^{(2)}\left(\mathbf{x_q}\right)\right]^*\right\}, \tag{4.15b}$$

where the superscript * represents the conjugate of the complex parameter. The sound transmission loss of the window can then be calculated (based on the ratio of incident to transmitted power) by using the definition of TL (Kinsler et al, 2000) given as follows:

$$\mathrm{TL} = 10\log_{10}\left(W_I/W_T\right). \tag{4.16}$$

4.4 An iteration scheme

Although it is possible to solve the coupled FEM/BEM equations directly by standard numerical routines using matrix operations, the computational resources required becomes excessive for a high-frequency sound source. This is because the solution involves the inversion of a square matrix with a size of $4\,Q \times 4\,Q$ where Q is the number of finite elements in each of the surfaces S_1, S_2, S_3, and S_4. We shall outline an iteration scheme in this section to reduce the computational time to obtain the numerical solutions for the TL of a double-pane window according to Eq. (16).

An iterative scheme may be developed by assuming that at step $m + 1$, the surface pressure on S_2 is given by $\{\mathbf{P_2}\}^{(m)}$, and the displacement vectors on Panel 2 are given by $\{\mathbf{d}^{(2)}\}^{(m)}$. Then, Eqs. (4.5) and (4.11) can be re-written in a recursive form as follows:

$$\left\{\mathbf{d}^{(1)}\right\}^{(m+1)} = \left\{\mathbf{H}^{(1)}\right\}\left[\left\{\mathbf{P_1}\right\}^{(m+1)} - \left\{\mathbf{P_2}\right\}^{(m)}\right], \tag{4.17a}$$

$$\left\{\mathbf{d}^{(2)}\right\}^{(m+1)} = \left\{\mathbf{H}^{(2)}\right\}\left[\left\{\mathbf{P_3}\right\}^{(m+1)} - \left\{\mathbf{P_4}\right\}^{(m+1)}\right], \tag{4.17b}$$

$$\left\{\mathbf{P_1}\right\}^{(m+1)} = 2\left\{\mathbf{P_0}\right\} - 2\left\{\mathbf{A}_a\right\}\left\{\mathbf{d}^{(1)}\right\}^{(m+1)}, \tag{4.17c}$$

$$\left\{\mathbf{P_2}\right\}^{(m+1)} = \left\{\mathbf{A}_b\right\}\left\{\mathbf{d}^{(1)}\right\}^{(m+1)} - \left\{\mathbf{A}_c\right\}\left\{\mathbf{d}^{(2)}\right\}^{(m+1)} + \left\{\mathbf{B}_c\right\}\left\{\mathbf{P_3}\right\}^{(m+1)}, \tag{4.17d}$$

$$\left\{\mathbf{P_3}\right\}^{(m+1)} = -\left\{\mathbf{A}_b\right\}\left\{\mathbf{d}^{(2)}\right\}^{(m)} + \left\{\mathbf{A}_c\right\}\left\{\mathbf{d}^{(1)}\right\}^{(m+1)} - \left\{\mathbf{B}_c\right\}\left\{\mathbf{P_2}\right\}^{(m)}, \tag{4.17e}$$

and

$$\left\{\mathbf{P_4}\right\}^{(m+1)} = 2\left\{\mathbf{A}_a\right\}\left\{\mathbf{d}^{(2)}\right\}^{(m+1)}, \tag{4.17f}$$

where the superscripts (m) and $(m+1)$ denote two consecutive iteration steps with m as a positive integer.

A close examination of these matrix equations reveals that the interactions between Panel 1

and Panel 2 are decoupled for known values of $\{P_2\}^{(m)}$ and $\{d^{(2)}\}^{(m)}$. The following steps are involved in the mth iteration:

(1) Solve Eq. (4.17a) and Eq. (4.17c) simultaneously to obtain $\{P_1\}^{(m+1)}$ and $\{d^{(1)}\}^{(m+1)}$ as follows,

$$\left\{d^{(1)}\right\}^{(m+1)} = \left[\{I\}+2\{A_a\}\right]^{-1}\left\{H^{(1)}\right\}\left[2\{P_0\}-\{P_2\}^{(m)}\right], \tag{4.18a}$$

and

$$\{P_1\}^{(m+1)} = 2\{P_0\}-2\{A_a\}\left(\{I\}+2\{A_a\}\right)^{-1}\left\{H^{(1)}\right\}\left[2\{P_0\}-\{P_2\}^{(m)}\right]. \tag{4.18b}$$

(2) Substitute $\{P_2\}^{(m)}$, $\{d^{(1)}\}^{(m)}$, and $\{d^{(2)}\}^{(m+1)}$ (which is obtained from step 1) into Eq. (4.17e) to obtain a numerical solution for $\{P_3\}^{(m+1)}$.

(3) Solve Eqs. (4.17b) and Eq. (4.17f) simultaneously to yield

$$\left\{d^{(2)}\right\}^{(m+1)} = \left[\{I\}+2\{A_a\}\right]^{-1}\left\{H^{(2)}\right\}\{P_3\}^{(m+1)} \tag{4.19a}$$

and

$$\{P_4\}^{(m+1)} = 2\{A_a\}\left[\{I\}+2\{A_a\}\right]^{-1}\left\{H^{(2)}\right\}\{P_3\}^{(m+1)}, \tag{4.19b}$$

where $\{P_3\}^{(m+1)}$ is obtained from Step 2.

(4) The iteration terminates if the solutions for $\{P_1\}$ and $\{P_4\}$ converge to within a specified limit. If not, the iteration process continues by calculating (i) $\{P_2\}^{(m+1)}$ from Eq. (4.17d) and (ii) using $\{d^{(1)}\}^{(m)}$ from Eq. (4.18a) for the next iteration.

Using this method, we do not have to solve the coupled matrix equations directly, which can potentially reduce substantial computational efforts. However, initial values for $\{P_2\}^{(m)}$ and $\{d^{(2)}\}^{(m)}$ (when $m = 0$) are needed for the iteration scheme. These initial values can be chosen as

$$\{P_2\}^{(m)} = \{0\}, \ \left\{d^{(2)}\right\}^{(m)} = \{0\}. \tag{4.20a,b}$$

4.5 Validation of the hybrid FEM/BEM scheme

The hybrid FEM/BEM model described in the previous section was implemented in the form of a suite of MATLAB programs for predicting the sound TL through double-pane windows. The validity of the hybrid model was confirmed by comparing the numerical predictions with those computed by ANSYS, a commercially available software FEM package, under the same boundary conditions. The details of setting up an ANSYS model for FEM analysis have been described in Chapter 2 and will not be repeated here.
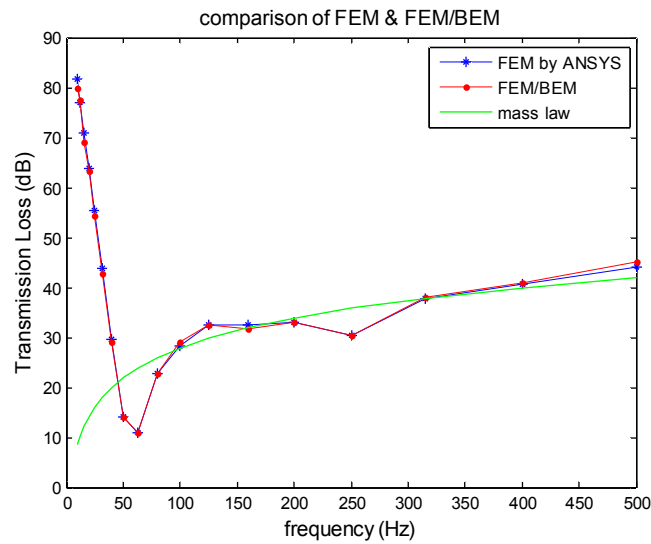
Fig. 4.2. Comparison of TL computed by FEM (ANSYS) and by hybrid FEM/BEM model.

Unless stated otherwise, the window used for the numerical simulations has a dimension of 1 m × 1 m. The Young's Modulus, Poisson's ratio, and density of the glass are assumed to be 70.3 GPa, 0.35, and 2700 kg·m^{-3}, respectively. In the first set of numerical simulations, the window panes had thicknesses of 5 and 7 mm and a cavity depth of 10 mm. This particular set of double-pane windows is referred to as 5(10)7 which indicates the thickness of each glass pane and the airspace (in parentheses). The same naming convention will be used throughout this

chapter to represent other double-pane windows used in the numerical simulations.

Figure 4.2 shows a comparison of the predicted TL spectrum according to the standard FEM formulation and those predicted by the hybrid FEM/BEM in one-third octaves varying from 25–500 Hz. The predictions of TL according to the mass law were also shown for the purpose of illustration. As expected, the predicted TL agreed with that predicted by the mass law at high frequencies (see Fig. 4.2). In general, the FEM predictions of TL were in good agreement with those computed by the hybrid FEM/BEM scheme developed in the present study.

Next, the numerical predictions of the hybrid FEM/BEM scheme were validated with the experimental data. The first set of data was taken from Robinson (2007) who conducted a series of sound TL measurements for high-performance, acoustically rated windows at the Structural Acoustic Load and Transmission (SALT) facility at the NASA Langley Research Center. The windows were placed in an aperture between a reverberant source chamber and an anechoic receiving chamber. The windows were secured by a wooden sub-frame where the sound intensity method was used to measure the sound transmitted through the windows. The dimensions of the windows used in the experiments were $1.21 \text{ m} \times 1.21 \text{ m}$. In his experiments, Robinson conducted a one-third octave band measurement ranging from 63 Hz to 4 kHz. A double-pane window, 6(13)5, was chosen for comparison with the predictions of the hybrid FEM/BEM model. The Sound Transmission Class (STC) and Outdoor-Indoor Transmission Class (OITC) indicated by the manufacturer were 36 dB and 29 dB, respectively. No information was provided about the mounting conditions. Hence, it was not possible to estimate the translational stiffness and rotational stiffness for the experimental setup. Nevertheless, these two stiffnesses were adjusted in the numerical simulations that led to the best-fit agreement between the measured data and the numerical predictions of the TL spectrum for frequencies varying from 63 to 500 Hz. Figure 4.3

presents the comparison of the experimental data with the predicted TL.
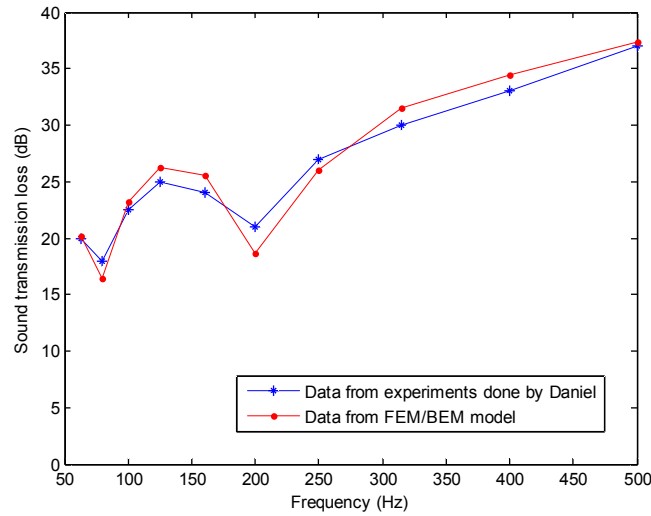
Fig. 4.3. Comparison of predicted TL (the hybrid model: -*-) with experimental data (-•-) taken from Robinson (2007).

As shown in the plots, the predicted TL was generally lower than the measured TL in the region around the natural frequencies (about 80 Hz and 200 Hz), but they were higher than the measured TL in other regions. This can be explained by noting two factors that influenced the measured TL. The first factor was the possible leakage of sound through other acoustic paths, e.g., transmission through the flanking supports of the window. This would have lowered the measured TL at the receiving chamber. On the other hand, the presence of damping along the edge supports of the glass panes could have caused a higher measured TL, particularly at the resonant frequencies. These two factors may provide possible reasons to explain the apparent discrepancies between the measured and predicted TL, shown in Fig. 4.3 above.

The second set of data was taken from Quirt (1983) who conducted a series of experiments in the 1980s for measuring TL of double-pane windows. Only the "simply supported" type of boundary conditions were used to mount the double-pane windows in his

93

experiments. However, it was found that a better agreement with experimental data can be achieved by assuming visco-elastic constraints at the support. Both rotational and translational stiffnesses and damping were used in the numerical simulations for frequencies varying between 80 and 500 Hz. For comparison, two different double-pane windows, 3(63)6 and 6(63)6, were used. Figure 4.4 displays the comparison between Quirt's experimental data and the predictions according to the hybrid FEM/BEM model presented in Section 4.3. It can be seen that the agreement is reasonably good between the experimental data and numerical predictions.
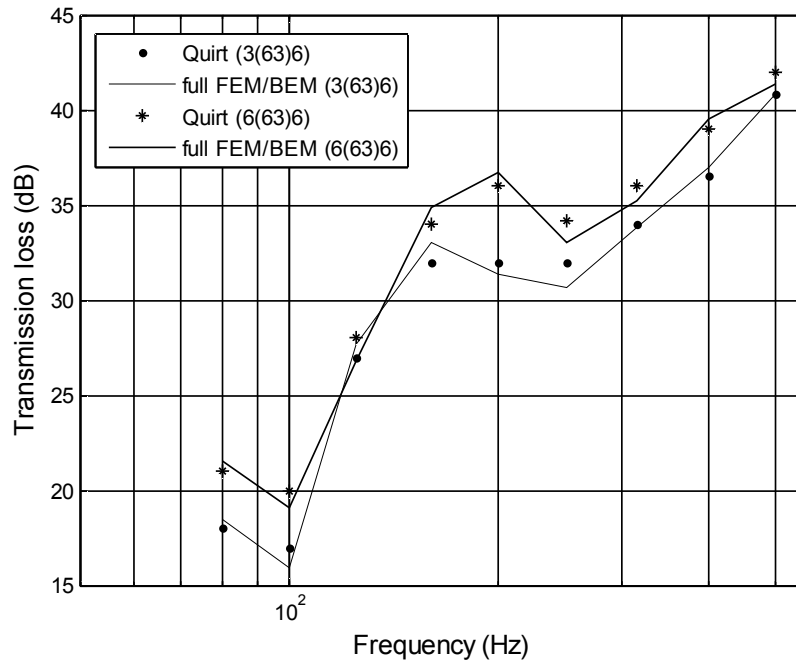
Fig. 4.4. Comparison of predicted TL with experimental data.

By comparing the results from the FEM models to two sets of experimental data, it was confirmed that the hybrid FEM/BEM model can provide an accurate numerical scheme for predicting the TL of LFN through double-pane windows. However, the computer program takes considerable time to predict the TL at higher frequencies. Section 4.4 presents an approximate

94

FEM/BEM model developed to calculate TL. To validate this approximation scheme, the numerical results from the hybrid FEM/BEM and the approximate FEM/BEM are compared, as shown in Fig. 4.5. The same double-pane window as in Fig. 4.3 was used in the numerical simulations for frequencies ranging from 25 to 500 Hz. The average discrepancy in the predicted TL between these numerical methods was about 2 dB, which can be used to confirm the validity of the approximate FEM/BEM model.
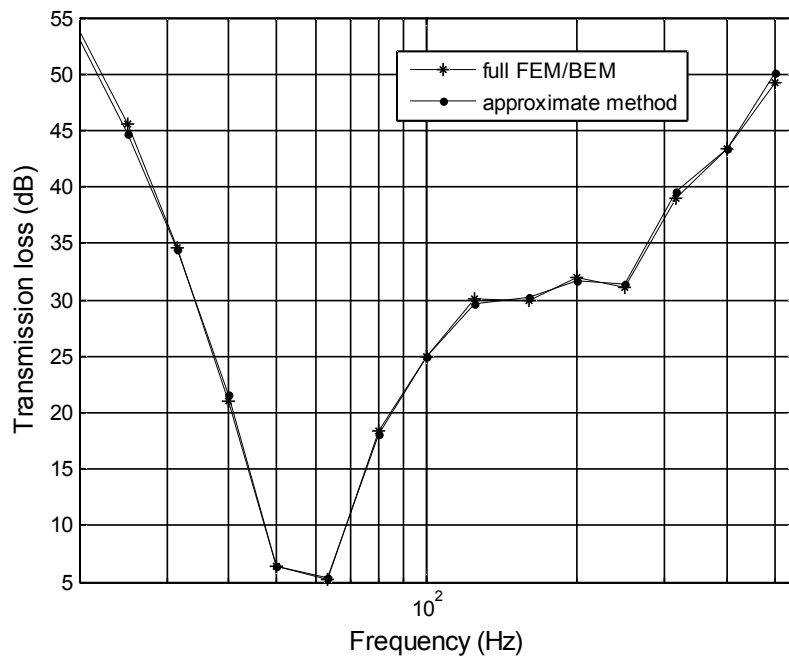
Fig. 4.5. Comparison of TL calculated by the hybrid FEM/BEM method (-*-) with the approximate method (-•-).

4.6 Numerical analysis and parametric studies of double-pane windows

As shown in Section 4.5, the approximate FEM/BEM model can be used to predict the TL of a double-pane window system. This approximate numerical model was used in addition to the hybrid FEM/BEM scheme in the following simulations for the parametric studies of double-pane windows.

(A) Effect of airspace in double-pane windows on TL

It is expected that the predicted sound TL is proportional to the thickness of the airspace in a double-pane window. Figure 4.6 displays TL predictions for three types of double-pane windows: 5(10)7, 5(20)7, and 5(30)7, where the window panes have identical thicknesses, but the airspaces have thicknesses of 10 mm, 20 mm, and 30 mm, respectively. As shown in Fig. 4.6, the increase in the thickness of the airspace caused an increase in the predicted TL for most one-third octave bands.
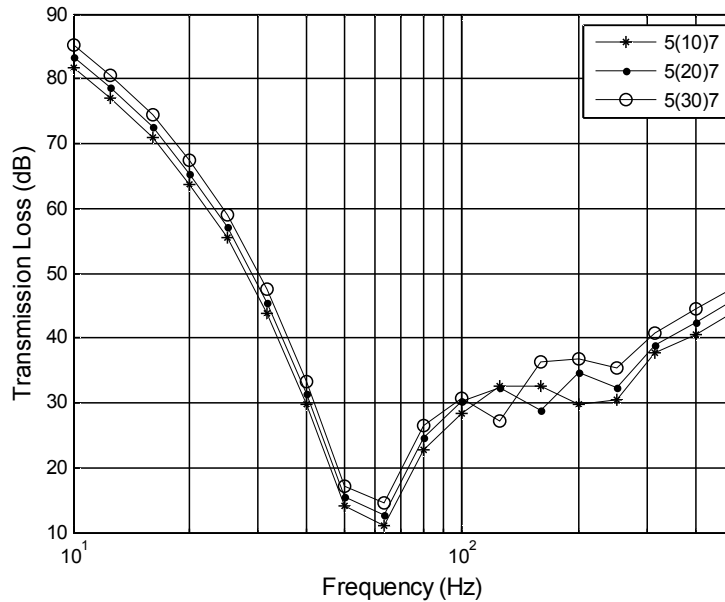
Fig. 4.6. Comparison of predicted TL for three different double-pane windows with different thicknesses of airspace.

As shown in Fig. 4.6, the predicted TL for different double-pane windows showed a respective "dip" or reduction in the frequency spectra. This was largely due to the presence of a mass-air-mass resonance region in the double-pane window. The mass-air-mass resonant frequency can be calculated readily as (Fahy, 2001)

$$f_{m\_a\_m} = \frac{1}{2\pi}\left(\rho_0 c_0^2\right)^{1/2}\left(\frac{m_1 + m_2}{m_1 m_2 \Delta_c}\right)^{1/2},$$ (4.21)

where Δ_c is the thickness of the airspace, m_1 and m_2 are the density per unit area of the first and second panels of the windows, ρ_0 is the air density, and c_0 is the speed of sound in air.
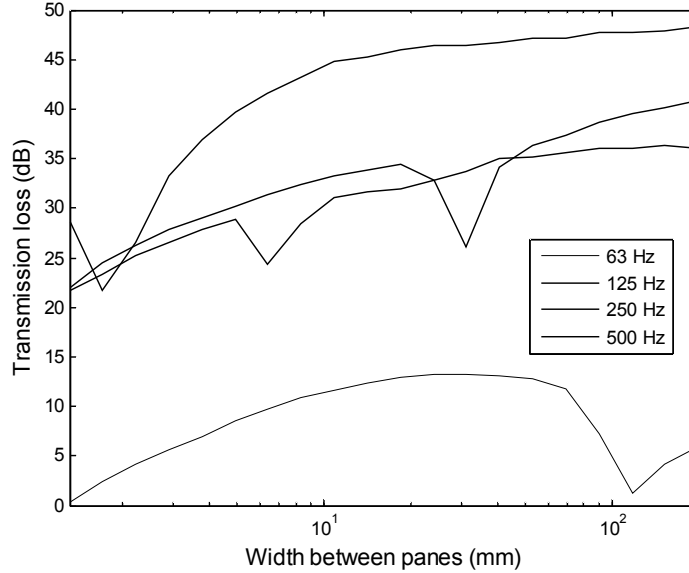
Fig. 4.7. Variation of TL with the width of airspace of a double-pane window.

For the appropriate constants for ρ_0 and c_0, the factor $\left(\rho_0 c_0^2\right)^{1/2}\big/2\pi$ in Eq. (4.21) is ~60.

Equation (4.21) enables the calculation of the corresponding mass-air-mass resonant frequencies of the windows used in the above numerical simulations. These respective resonance regions are within the 250, 160, and 12 Hz one-third octave bands for the 5(10)7, 5(20)7, and 5(30)7 double-pane windows. It is clear from Fig. 4.6 that it is the effect of the mass-air-mass resonant frequency that produces a dip in the predicted TL spectra at the respective resonance regions for these three windows. For other frequency regions, the predicted TL generally increases with the thickness of the airspace in the double-pane windows. This characteristic is demonstrated in the numerical simulations shown in Fig. 4.7.

It is of interest to note that different fluids may be used in the sealed airspace of the double-pane windows in order to improve their sound insulation characteristics. To elucidate the effects of different fluids, hydrogen (H_2) gas, carbon dioxide (CO_2) gas, and air were used in the next set of numerical simulations for a 5(10)7 double-pane window. It is expected that the sound TL through double-pane windows would decrease with the density of the fluid in the sealed airspace. Since the density of CO_2 is highest and that of H_2 is lowest among the three type of gases used in the numerical simulations, i.e., $\rho_{co_2} > \rho_{air} > \rho_{H_2}$, it is expected that $TL_{co_2} < TL_{air} < TL_{H_2}$. Indeed, the numerical simulations of TL spectra shown in Fig. 4.7 confirmed this trend. However, there was a dip in each of the mass-air-mass frequency region in these three, as spectra shown in Fig. 4.8.
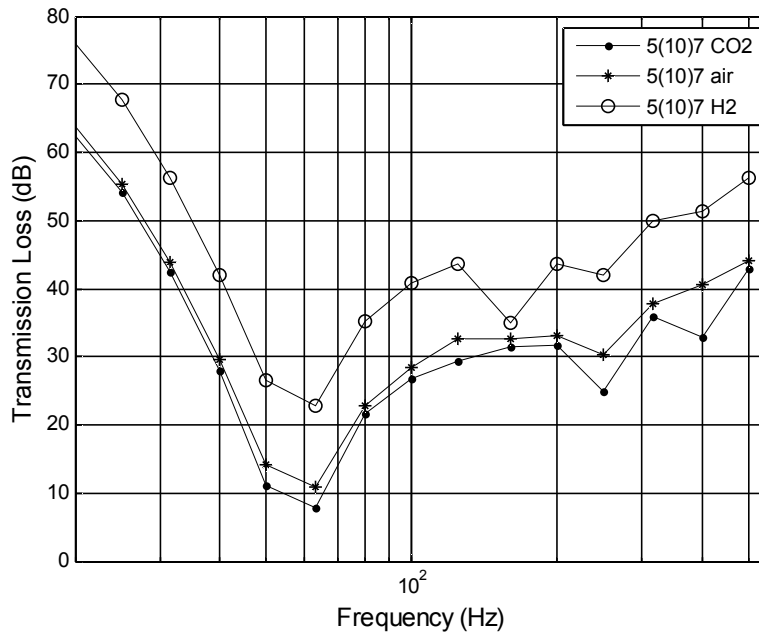
Fig. 4.8. Prediction of TL for different fluid filled in the airspace of the double-pane window.

For reference, the mass-air-mass resonant frequencies for different types of double-pane windows are listed in Table 4.1.

Table 4.1. Mass-air-mass resonance frequencies of double-pane windows.

Windows	Mass-air-mass resonant frequency (Hz)
5(10)7	Air: 218 CO_2: 360 H_2: 172
5(20)7	165
5(30)7	124
10(30)7	104
5(30)14	110
5(10)5	235
7(10)7	200

(B)   Effect of pane thickness on TL of double-pane windows
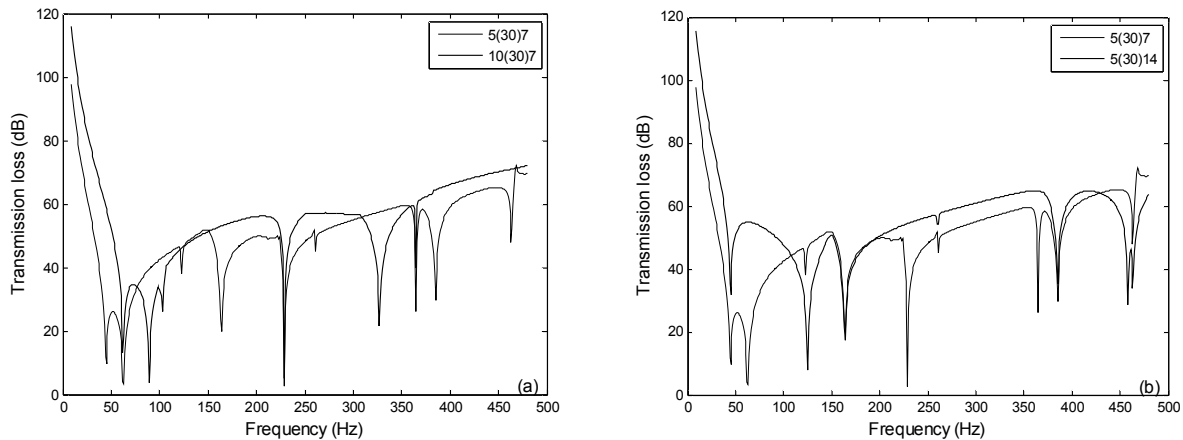
Fig. 4.9. Prediction of TL for different double-pane window systems.

According to the mass law, the sound TL increases with the density per unit area of the glass

99

panes (m_1 and m_2). By increasing the thicknesses of the glass panes, the TL was expected to increase because of the increments in m_1 and m_2. This observation is shown in Figs. 4.9a and 4.9b. According to our analysis in Chapter 2, the thickness of a window pane is an important factor in calculating the natural frequencies of rectangular panels. Hence, these frequency dips are located at different frequencies for double-pane windows with different thicknesses for each pane. When the thickness of only one pane is changed, some of these dips will occur at different frequencies. However, the dips at the natural frequencies of the unchanged pane remain constant. These observations are evident in Fig. 4.9a and 4.9b.
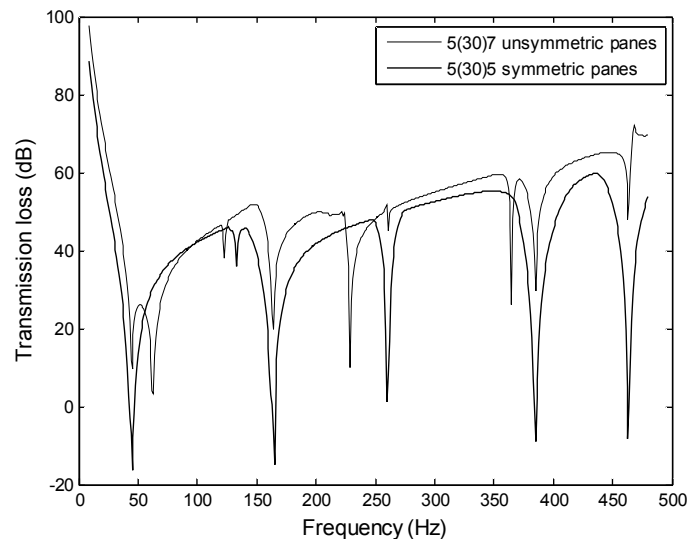
Fig. 4.10. Prediction of TL for a symmetric and non-symmetric double-pane windows.

Figure 4.10 shows the comparison of the predicted TL for double-pane windows with symmetric panes (two panes of the same thickness) and non-symmetric panes. Specifically, two different windows, 5(30)5 and 5(30)7, were used in the numerical simulations. For the 5(30)5 double-pane window, there were significant dips at the natural frequencies since both panes resonated at the same natural frequencies. In fact, London (1950) showed that a double wall composed of two identical single walls could lead to a significant break-down problem in sound insulation. The

recommendation (Marsh 1971, Cops et al. 1975) of using glass panes of different thicknesses is supported by the simulation results shown Fig. 4.10.

(C) Effects of boundary conditions of window panes

It has been demonstrated in Chapter 2 that the mounting conditions of the glass pane significantly affect sound transmission through single-pane windows. The mounting conditions of the two glass panes are again detrimental to predictions of sound transmission through the double-pane windows. The predicted TL spectra for some typical mounting conditions are shown in Figs. 4.11a and 4.11b. The resonant-frequency dips are located at different frequencies for windows with different types of boundary conditions for each glass pane.
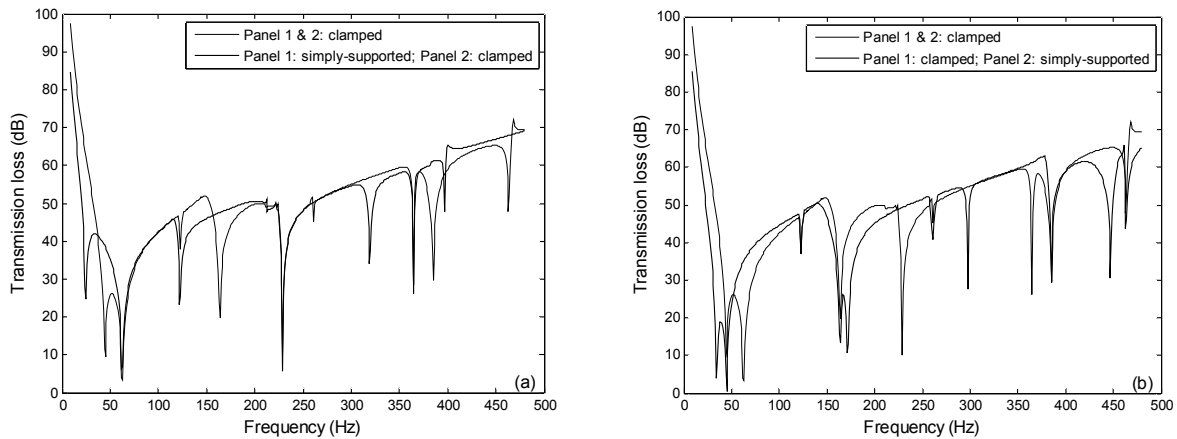
Fig. 4.11. Prediction of TL for a double-pane window with different mounting conditions.

4.7 Conclusions

In this chapter, the formulation of a coupled FEM/BEM model for double-pane windows was presented. An iteration scheme was introduced that could be easily extended to a triple-pane window or even a multiple-pane window. This study is expected to form the basis for developing

an efficient numerical scheme to calculate the TL of a double-pane window in a future study. Both the hybrid and approximate FEM/BEM methods were applied to the parametric studies, and the following conclusions were drawn:

- When the thickness of the airspace in a double-pane window increases, the sound TL increases.

- When the density of the fluid in the sealed airspace of the double-pane window decreases, the sound TL increases.

- The mass-air-mass resonance significant affects the prediction of the sound TL of double-pane windows.

- The change in the thickness of the airspace or the density of the fluid in the sealed airspace can change the mass-air-mass resonant frequency.

- The thickness and boundary conditions of the panes significantly affect the shape of the TL curve.

- The hybrid and approximate FEM/BEM models are useful for studying the transmission of LFN through double-pane windows during the design stage.

References

L. L. Beranek, G. A. Work, 1949. "Sound transmission through multiple structures containing flexible blankets," *Journal of the Acoustical Society of America* **21**, 419–428.

A. Cops, H. Myncke, and G. Vermeir, 1975. "Insulation of reverberant sound through double and multilayered glass constructions," *Acustica* **33**, 257-265.

L. Cheng, and Y. Y. Li, 2006. "Active noise control of a mechanically linked double panel system coupled with an acoustic enclosure," *Journal of Sound and Vibration* **297,** 1068-74.

O. Chiello, F. C. Sgard, and N. Atalla, 2003. "On the use of a component mode synthesis technique to investigate the effects of elastic boundary conditions on the transmission loss of baffled plates," Computers & Structures **81**, 2645-2658.

R. R. Craig, 1977. *"Methods of component mode synthesis," Shock Vibration Digest* **9**, 3–10.

R. J. M. Craik, 2003. "Non-resonant sound transmission through double walls using statistical energy analysis," *Applied Acoustics* **64**, 325-341.

M. J. Crocker, A. J. Price, 1969. "Sound transmission using statistical energy analysis," *Journal of Sound and Vibration* 9, 469–486.

A. Cummings, K. A. Mulholland, 1968. "The transmission loss of finite sized double panels in a random incidence sound field," *Journal of Sound and Vibration* **8**, 126–133.

R. J. Donato, 1972. "Sound transmission through a double-leaf wall," *Journal of the Acoustical Society of America* **51,** 807–15.

F. J. Fahy, 1985. *Sound and structural vibration – radiation, transmission and response.* Academic Press Ltd, London, England.

F. J. Fahy, 2001. *Foundations of engineering acoustics.* Academic Press, London, UK.

L. Gaul, M. Ko̎gl and M. Wagner, 2003. *Boundary element methods for engineers and scientists: an introductory course with advanced topics*, New York: Springer.

K. H. Huebner, E. A. Thornton and Ted G. Byrom, 1995. *The finite element method for engineers,* New York: Wiley.

A. Jakob, and M. Moser, 2003. "A modal model for actively controlled double-glazed windows," *Acta Acustica United With Acustica* **89,** 479-93.

O.E. Kaiser, S.J. Pietrzko, M. Morari, 2003. "Feedback control of sound transmission through a double glazed window," *Journal of Sound and Vibration* **263**, 775-95.

L. E. Kinsler, A. R. Frey, A. B. Coppens, J. V. Sanders, 2000. *Fundamentals of acoustics*, Fourth Edition, New York, John Wiley.

Y. J. Kang, J. S. Bolton, 1996. "A finite element model for sound transmission through foam-lined double-panel structures," *Journal of the Acoustical Society of America* **99**, 2755-65.

L. E. Kinsler, A. R. Frey, A. B. Coppens, J. V. Sanders, 2000. *Fundamentals of acoustics*, Fourth Edition, New York, John Wiley.

S. Langer, H. Antes, 2003. "Analyses of sound transmission through windows by coupled finite and boundary element methods,*" Acta Acustica United With Acustica* **89**, 78-85.

A. London, 1950. "Transmission of reverberant sound through double walls," *Journal of the Acoustical Society of America* **22** 270–279.

R. H. Lyon, G. Maidanik, 1962. "Power flow between linearly coupled oscillators," *Journal of the Acoustical Society of America* **34**, 623–639.

J. A. Marsh, 1971. "The airborne sound insulation of glass," *Applied acoustics*, Part 1: 55-70; Part 2: 131-154; Part 3: 175-192.

K. A. Mulholland, A. J. Price, H. D. Parbrook, 1968. "Transmission loss of multiple panels in a random incidence field." *Journal of the Acoustical Society of America* 43, 1432–1435.

K. A. Mulholland, H. D. Parbrook, A. Cummings, 1967. "The transmission loss of double panels," *Journal of Sound and Vibration* **6**, 324–334.

J. Price, M. J. Crocker, 1970. "Sound transmission through double panels using statistical energy analysis," *Journal of the Acoustical Society of America* **47,** 683–93.

J. D. Quirt, 1983. "Sound transmission through windows – 1. double and triple glazing", *Journal of the Acoustical Society of America* **74**, 534-542.

D. Robinson, 2007. *Effect of low frequency sound on resonant sound insulation and rattle*

systems. M. S. Thesis, Purdue University.

F. C. Sgard, N. Atalla, J. Nicolas, 2000. "A numerical model for the low frequency diffuse field sound transmission loss of double-wall sound barriers with elastic porous linings," *Journal of the Acoustical Society of America* **108**, 2865-72.

W. Soedel, 1993. Vibrations of shells and plates, Marcel Dekker, Inc., New York.

W. A. Utley, B. L. Fletcher, 1973. "The effect of edge conditions on the sound insulation of double windows," *Journal of Sound and Vibration* **26**, 63-72.

P. H. White, A. Powell, 1966. "Transmission of random sound and vibration through a rectangular double wall," *Journal of the Acoustical Society of America* 40, 821–832.

5. Energy efficiency of dual-airflow windows in different climate zones

5.1 Introduction

In the United States, energy demand by buildings accounts for about one third of the total primary energy demand and about two thirds of the electricity consumption (Shen, 2007). Heating, ventilation, and air conditioning (HVAC) systems use nearly 55% of the energy for buildings (Shen, 2007). In order to reduce energy demand by HVAC systems, it is essential to reduce heat loss in winter and heat gain in summer through building envelopes such as windows, walls, roofs, and floors, and through natural ventilation, i.e., infiltration. As a result, glazing has been increased from single to double, and even to triple layers. A parallel effort has been made to improve glazing and frame properties. For example, it is becoming more and more common to seal windows against leakage and to use low-emissivity (low-e) coatings to reduce radiation.

Better window and wall construction has made buildings more airtight which is good for energy conservation. However, improvement in energy efficiency has been achieved at the expense of IAQ (Sherman and Matson, 1997). The Environmental Protection Agency (EPA) in the U.S. has reported that inadequate ventilation can increase indoor pollutant levels (see http://www.epa.gov/iaq/ia-intro.html). Poor IAQ has been linked to respiratory illness, allergies, asthma, and sick building syndrome (Luo, 2007). It is a challenging task to devise a scheme to conserve energy and to maintain acceptable IAQ in buildings, particularly in residences.

One way to improve IAQ is to supply fresh air through the window frames. However, supplying very cold air in winter and very warm air in summer directly to a room through the window frames can waste substantial amounts of energy and cause discomfort to the occupants. Heat recovery ventilators or enthalpy recovery ventilators are frequently used in commercial and

industrial buildings. They transfer heat between the exhaust air and the supply fresh air to conserve energy (Liu et al., 2007; Zhong and Kang, 2009). Such a heat-recovery system is often integrated with central air-conditioning systems (Zhong and Kang, 2009). However, it is not suitable for residential buildings with hydraulic heating systems and window/split air-conditioning units. Double-skin façades are sometimes used to trap solar energy and to supply fresh air into indoor spaces (Saelens et al., 2003), but they are too expensive to be used in residential buildings (Saelens et al., 2008).

Airflow windows, which work like a double-skin façade, can be used in residential buildings (Baker and McEvoy, 2000). In fact, some airflow windows can work like a heat exchanger (Gosselin and Chen, 2008a), which is very promising for energy conservation and IAQ improvement. Our effort in the present study was to analyze one of the best airflow windows for its energy efficiency in different climates. The results were compared with the energy efficiency of conventional types of windows. The present study also investigated the change in the IAQ of buildings where airflow windows were used.

This chapter and those that follow address the environmental performance of dual-airflow windows. In particular, Chapter 6 studies their ability to improve IAQ. Details of the investigations of the energy efficiency of dual-airflow windows are presented in the following sections.

5.2 Principles of the theoretical formulation

This section starts by describing the basic principles of airflow windows. Then, an outline of the numerical model used in the simulation is presented. The details of the mathematical formulation are given in Appendix A, and the experimental validation of the numerical models is provided.

The main difference between an airflow window and a conventional window is the existence of free or forced convection in the cavity between the two glass layers. Depending on the airflow pattern through the window structure, there are five modes of operation for airflow windows (Gosselin and Chen, 2008a): supply mode, exhaust mode, indoor air curtain mode, outdoor air curtain mode, and dual airflow mode. Figure 5.1 shows these five modes of operation for airflow windows, where the outdoor and indoor locations are shown on the left and right sides of each window, respectively.

The supply mode (Fig. 5.1a) draws fresh air from the outside through the cavity and into the building. The air is heated in the cavity by solar radiation, and hence, this mode is designed for winter heating. The exhaust air mode (Fig. 5.1b) extracts the air inside the cavity and expels it into the outdoor space. The window uses cool indoor air and buoyancy force from the solar radiation to cool the window panels and to remove heat accumulated in the cavity. The exhaust mode is suitable for summer passive cooling. The indoor air curtain window (Fig. 5.1c) uses solar radiation to heat indoor air in winter. The outdoor air curtain window (Fig. 5.1d) circulates the outdoor air by solar radiation to cool the window panels in summer. There is no air exchange between the indoor and outdoor spaces for air curtain windows. Venetian blinds are often added into the cavity because solar radiation can be easily trapped by the blinds.

The dual-airflow window (Fig. 5.1e) has two airflow paths in which the outer airflow path supplies fresh outdoor air to the inside space and the inner airflow path extracts indoor air to the outside space. The middle layer of glass works as a heat exchanger. The first four modes can be operated by a buoyancy force from solar radiation or a mechanical force provided by a fan. The dual-airflow window requires two fans for the inlet and exhaust flows.

Unlike conventional windows, all the airflow windows can capture solar heat trapped in the cavity and direct it indoors or outdoors depending on the operating mode. This captured solar energy is used for passive heating in winter or passive cooling in summer. The dual-airflow window is better than the supply or exhaust mode windows because it has a higher efficiency due to the heat exchanger function. The window is also better than the outside and inside curtain windows because it can bring in fresh air (Gosselin and Chen, 2008b).
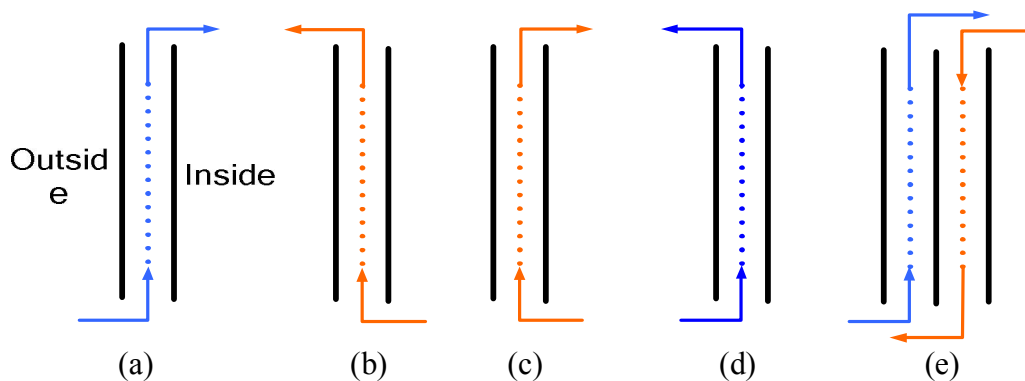
Fig. 5.1. Operating modes of airflow windows: (a) supply mode, (b) exhaust mode, (c) indoor air curtain mode, (d) outdoor air curtain mode, and (e) dual airflow mode.

Dual-airflow windows can conserve energy and improve IAQ by supplying fresh outdoor air to indoor spaces. Gosselin and Chen (2008b) demonstrated in a laboratory environment that dual-airflow windows can conserve energy. However, their study was on steady-state heat transfer and did not compare the performance of other windows. The present investigation further evaluated the energy efficiency of dual-air windows in different climates in the U.S. and compared their energy efficiency with other types of conventional windows.

Different approaches, e.g., bin methods (Doty and Turner, 2009), experimental measurements, and computational fluid dynamics (CFD) numerical schemes can be used to analyze the energy efficiency of window systems. It is known that the bin methods are too simple for the comparison of the energy efficiency of these window systems since solar radiation

is not included in the analysis, and energy demand is usually approximated as a linear function of the outdoor air temperature. As a result, although this approach is straightforward and simple to apply, the bin methods were not suitable for the present study.

While the experimental approach offers the most reliable and realistic results, it is both expensive and time consuming to collect the data required for design purposes. It is also unrealistic to use the experimental approach to study yearly energy demand in different climate regions. In contrast, the CFD method can produce accurate and informative results by solving highly reliable Navier-Stokes equations. Unfortunately, the CFD method requires significant computational resources in order to obtain accurate simulations for yearly energy demand under various weather conditions. It is of interest to point out that an energy-based numerical method can be used as an alternative to CFD methods in order to reduce the need for large computational resources. Commercially available energy analysis programs, such as EnergyPlus (Strand et al., 2000) and ESP-r (Yezioro et al., 2008), can be used to simulate the energy efficiency of a window system by solving a one-dimensional energy equation (Strand and Pedersen, 1997).

As mentioned in the preceding paragraphs, the energy-based method offers a convenient approach for calculating energy demand over a long period of time. EnergyPlus is a popular computer program in which the energy-based method was implemented. The accuracy of EnergyPlus has been validated by many previous studies, e.g. (Dutton et al, 2008) . In addition, the source code for EnergyPlus is written in Visual Fortran, and hence, it can be easily modified. Consequently, EnergyPlus was chosen for the present study. It should be pointed out that EnergyPlus uses a one-dimensional heat transfer model; however, dual-airflow windows have significant vertical airflows. As a result, an unmodified EnergyPlus program is not sufficiently accurate to model the heat transfer process in dual-airflow windows. In light of this shortcoming,

a two-dimensional model was developed and implemented in EnergyPlus to provide a more accurate calculation of the energy demand for dual-airflow windows. Details of the mathematical analysis have been relegated to Appendix A; a flowchart of the implementation scheme is shown in Fig. 5.2.
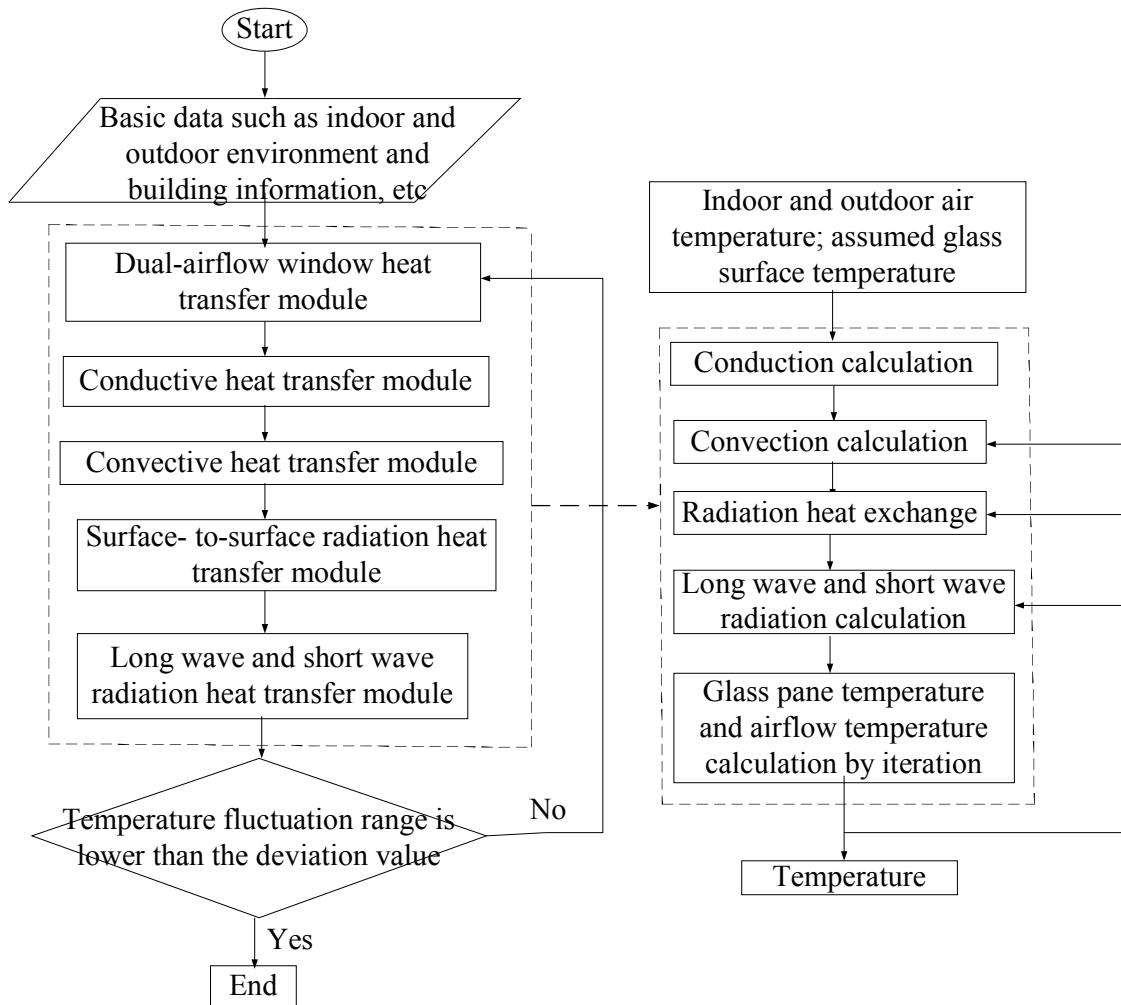
Fig. 5.2. Flowchart to illustrate the calculation procedures for a dual-airflow window network model.

Because of the assumptions used in the mathematical formulation, it is necessary to validate the modified EnergyPlus program with experimental data. More importantly, the numerical implementation of a two-dimensional model in EnergyPlus is complicated. Experimental

validation ensures that the simulated results can be applied accurately to designing dual-airflow windows with optimal parameters. The validation procedures are based on dual-airflow windows and two types of conventional windows: (i) a low-e double-pane window and (ii) a double-pane window with internal blinds. The simulated results were compared with measured data obtained from an experimental study conducted in Harbin, China.

Figure 5.3a shows a schematic diagram of a dual-airflow window. Figures 5.3b and 5.3c show sketches of a low-e window and an internal blind window, respectively. The simulated results for these two types of conventional windows were compared with those obtained for a dual-airflow window. The modified EnergyPlus program was used to provide simulated results. The low-e and internal blind windows were selected as the conventional windows in the present study because they are popularly used in residential buildings located in the northeastern part of China.
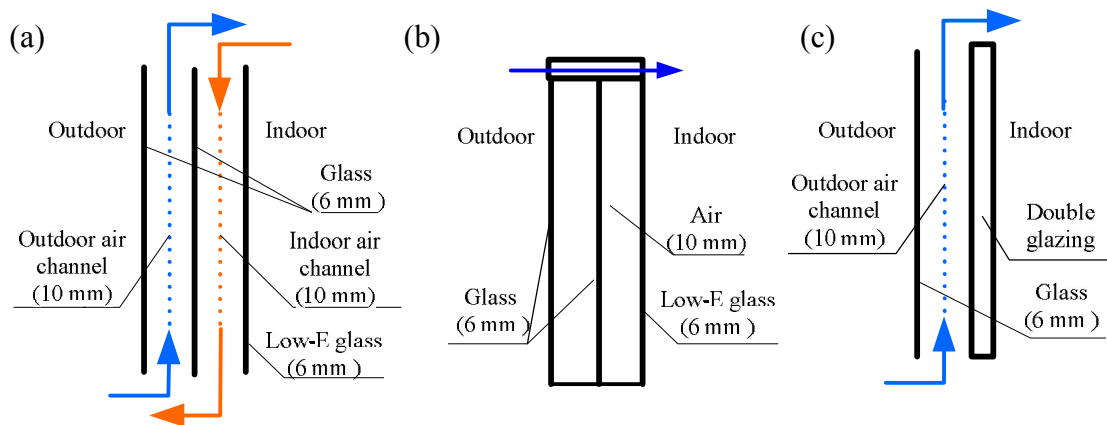
Fig. 5.3. Three different windows used in this study: (a) dual-airflow window, (b) low-e window, and (c) internal blind window.

In the experimental studies, the dual-airflow window was constructed with 3 clear glass panes with no coating. The thickness of airflow channel between 2 glass panes was 10 mm as suggested by Gosselin and Chen (2008a). The thickness of each glass pane was 6 mm. The same

112

type of glass pane was used for the two remaining window systems. Both the low-e and blind windows were double-paned since these are typically used in China, and they meet the thermal insulation requirements of Chinese national standards. The low-e window had a low-emissivity coating on the interior surface of the inner glass panes. The coating reduces long-wave radiation loss to the outside space (Werner and Roos, 2008). The thickness of the cavity between the glass panes was 9 mm. Venetian blinds were installed in the cavity of the blind window to absorb solar radiation in winter and reflect a major part of solar radiation back to the outdoor space in summer. During winter nights, the blinds work as an insulation layer that can reduce heat loss to the outside (Tzempelikos, 2008). The cavity thickness was 23 mm to permit the movement of the 20 mm width of the blinds between the window panes. To obtain a comparable configuration, the blinds were closed in the summer daytime and in the winter nighttime for the experimental setup, and the closed position was assumed in the relevant numerical simulations.

The experiments were conducted at a test site in Harbin, China during the period between 17th and 23rd February in 2007. The weather was sunny throughout the measurement period, including nearly the coldest days in Harbin that year. From the measured data, daily energy demand profiles were determined for the three types of windows which were installed in different cells. These measured results were compared with simulated results, which were calculated by the modified EnergyPlus program using a network model (see Appendix A). Measured data on February 23, 2007 were compared with the corresponding numerical simulation data. Figure 5.4 shows that the simulated energy demand profiles of the cells agree well with the measured data with a discrepancy of less than 0.01 kW in most cases. The difference between the measured and computed results was equivalent to the energy loss caused by 0.9 m^3/h, or 0.045 air changes per hour (ACH), of infiltration with a temperature difference of

40 K between the indoor and outdoor air. It is generally expected that the fluctuation in infiltration is significantly higher in field measurements than in those assumed in the numerical simulations. Consequently, the energy demand simulations generally produced smoother profiles than those obtained from the measured data.
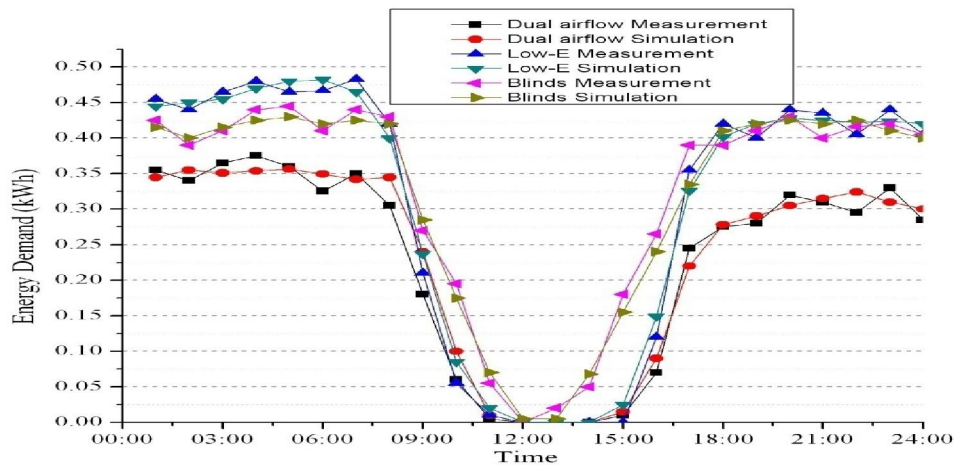
(a) Windows without ventilation in the south-facing cells
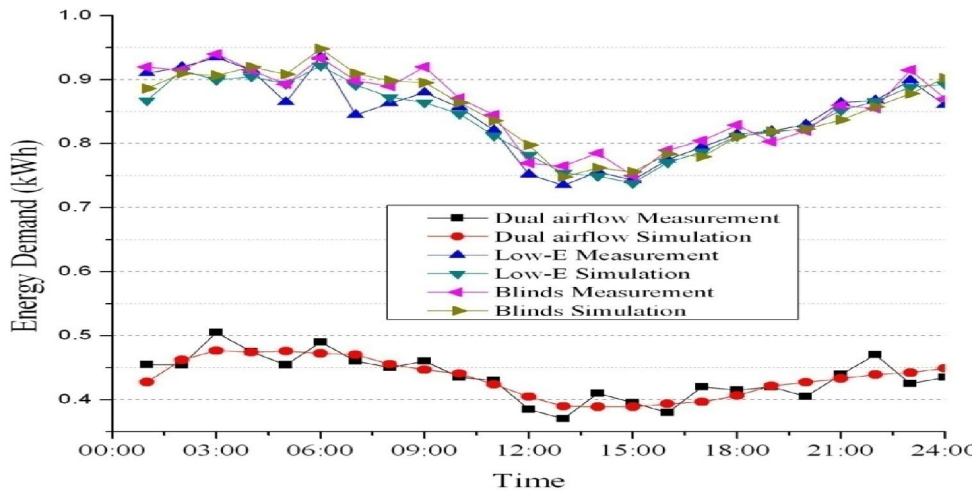
(b) Windows with ventilation in the north-facing cells

Fig. 5.4. Comparison of computed energy demand by the cells with the three types of windows along with experimental data from February 23, 2007.

Next, a more detailed comparison of the measured data to the simulated results is described as follows. Figure 5.4a shows the energy demand profiles of the three south-facing cells where

114

there was no ventilation for the test windows. During the non-daylight periods (from 6:00 p.m. to 8:00 a.m.), all cells showed rather constant energy demand profiles. The cell with the dual-airflow windows required the least energy because its three-pane construction provided the best thermal insulation. As the sun rose, the energy demand for all cells decreased steadily starting about 8:00 a.m. and reached zero by about noon. Depending on the weather conditions, the energy demand increased steadily as sunlight faded. These diurnal changes can be attributed to the heat gain from solar radiation transmitted through the test windows. Among the three types of test windows, the cell with the blind window required more energy between 8:00 a.m. and 5:00 p.m. This is because the blinds reflected much of the solar energy incident on the windows.

Figure 5.4b shows the energy demand for the three cells with north-facing windows. All windows were ventilated with a supply air rate of 40 m^3/h. The low-e and blind windows supplied fresh air from outdoors directly to the cells with a fan. The measured data were modified to include the effect of the ventilation on energy demand. As depicted in the plots, the cell with the dual-airflow window required only about a half as much energy as the cells with the conventional windows. The significant reduction in energy demand was largely because of heat recovery between the two streams of air flowing in the window cavities in the dual-airflow window. The energy demand for all the cells with the three types of windows changed little during the day because very little solar energy was received by the north-facing windows. There was a significant difference in the indoor and outdoor air temperatures.

As shown in Figs. 5.4a and 5.4b, the experimental data confirm the validity of the numerical model for predicting the energy efficiency of the dual-airflow window with and without ventilation. These results demonstrated that the modified EnergyPlus program can conveniently be used to calculate the energy demand for a room with dual-airflow windows.

115

5.3 Prediction of energy efficiency in different climate regions

The energy-saving ability of dual-airflow windows is increased by their high thermal insulation and improved heat recovery due to their triple-pane construction. It is known that the energy efficiency of dual-airflow windows can be optimized by considering the heating and cooling loads of the windows. However, these thermal loadings cannot be converted directly into building energy demand which renders the evaluation of energy efficiency more difficult. This is because the building efficiency can be affected by such factors as indoor heat gain, heat transfer through exterior walls, and availability of ventilation. It is therefore necessary to investigate the energy demand for buildings with dual-airflow windows. The objective of Sec. 5.3 is to evaluate the effect on residential building energy demand in different climate zones in the U.S. owing to the use of dual-airflow windows.

Two types of residential buildings were considered: an apartment and a detached house with dual-airflow windows in both. They were selected based on the assumption that the energy demand of different types of buildings is affected by the window heating/cooling load. This heat transfer between different indoor spaces and exterior walls causes different total thermal loads on the buildings. A generic apartment with a floor area of 80 m^2 and a detached house with a floor area of 200 m^2 were assumed in the numerical simulations using the modified EnergyPlus program.

Specifically, the apartment was placed on a middle floor of a residential building with neighboring apartments on the east and west sides and exterior walls on the north and south sides. The interior walls, ceiling, and floor of the apartment were assumed to be parts of an interior envelope. The interior walls of the apartment were assumed to be adiabatic because their neighboring rooms have essentially the same air temperature. However, the simulated detached

house has four exterior walls, which means it has more heat transfer through exterior walls than the apartment. The exterior walls of the apartment and the detached house were constructed with 240 mm thick reinforced concrete with 120 mm polystyrene insulation boards.
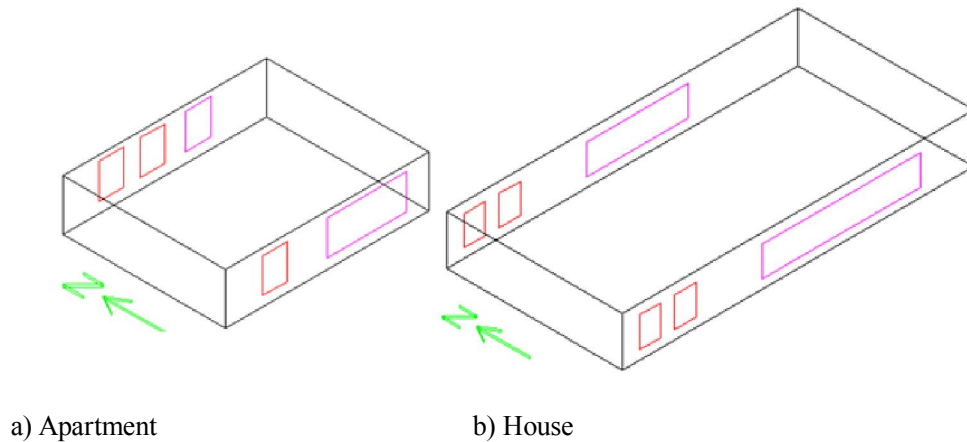
a) Apartment   b) House

Fig. 5.5. Simplified model for buildings used in the modified EnergyPlus program. Red rectangles indicate the ventilated windows, pick rectangles represent conventional windows.

Table 5.1. Size of the apartment, the detached house, and their windows.

	Apartment	House	Ventilated window	North conventional window in the apartment	South conventional window in the apartment	North conventional window in the house	South conventional window in the House	PVC frame
length (m)	10	20	-	-	-	-	-	-
width (m)	8	10	1	2.2	4.8	7.3	11	0.08
height (m)	2.6	2.8	1.5	1.5	1.5	1.5	1.5	-

Figure 5.5 shows the building models used in the modified EnergyPlus program for calculating the energy demand of the buildings. The sizes of the two buildings are listed in Table 5.1. All indoor spaces within a building were assumed to have the same air temperatures. Consequently, all partition walls inside these two types of buildings were ignored for facilitating the numerical analyses. In Fig. 5.5, the red rectangles indicate the ventilated windows, and the pink rectangles represent conventional windows. A further assumption was made that there were

three occupants in the apartment and four in the detached house. Inside the buildings, each occupant was provided with fresh air by one ventilated window. Hence, there were three ventilated windows in the apartment and four in the detached house.

The energy efficiency of three different types of windows was examined here. Figure 5.6 shows the schematic diagrams of these three types of windows:

(a)   a dual air-flow window,

(b)   a double-pane low-e window, and

(c)   a double-pane, supply-airflow window.

a) Dual-airflow window   b) Three-layer glazing   c) Supply-airflow
conventional window   window
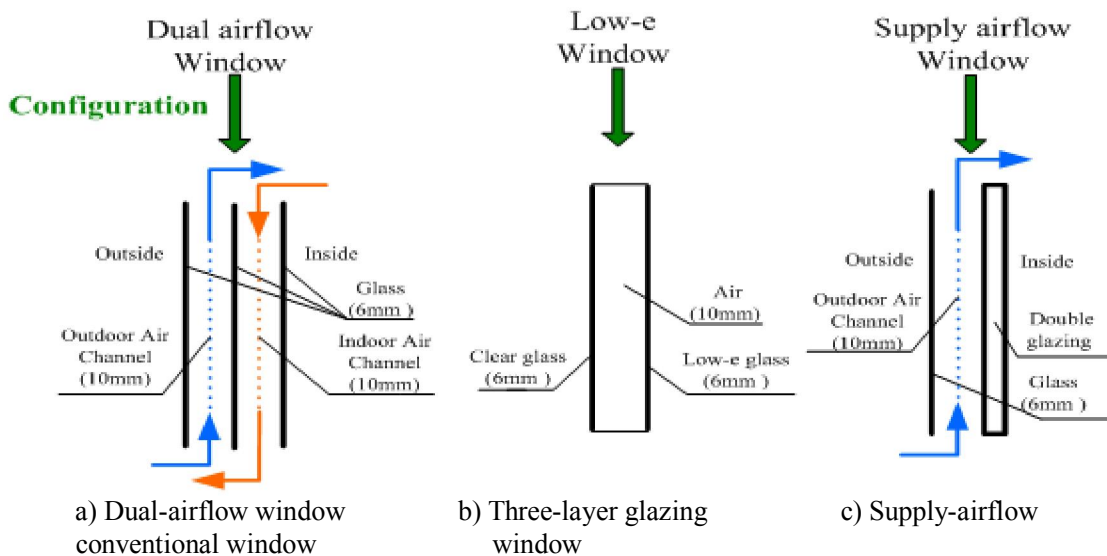
Fig. 5.6. Three different types of windows used in this study.

The same ventilation rate of 36 m^3/h was used in these three types of windows. This air flow rate, which meets the ANSI/ASHRAE Standard (2001) of 10 liter/s per person, provides an acceptable IAQ in the residential building. The ventilation was provided by an electric fan in each ventilated window. The total electric power consumption for the three ventilated windows

was estimated to be 50 W. A further assumption was made in which a total electric load of 100 W was needed for lighting and electrical appliances in the buildings. The indoor air temperature was set between 20 °C and 26 °C for human comfort. No additional heating or cooling was needed when the indoor temperature stayed within this range. Table 5.2 lists the daily activities of occupants in the residential buildings. It was assumed that there were no activities between 9:00 a.m. and 5:00 p.m. during weekdays, but the occupants were assumed to remain in the buildings during weekends. The indoor air temperatures at different times are given in Table 5.2.

Table 5.2. Occupant activity time and indoor air temperature control.

	Weekday				Weekend	
	23:00–8:00	8:00–9:00	9:00–17:00	17:00–23:00	23:00–8:00	8:00–23:00
Indoor space with occupancy	Bedroom	Living room	-	Living room	Bedroom	Living room
Heating setpoint	18 ℃	18 ℃	≥10 ℃	18 ℃	18 ℃	18 ℃
Cooling setpoint	26 ℃	26 ℃	No control	26 ℃	26 ℃	26 ℃

Owing to the large geographical size of the U.S., weather conditions vary widely in different parts of the country. According to a study by Briggs et al. (2003a, 2003b), it is possible to divide the continental U.S. into seven climate zones:

(1) Very hot climate that can be described as tropical wet and dry for the humid regions and tropical desert for the dry regions;

(2) Hot climate that can be described as humid sub-tropical (warm summer) for the humid regions, and, arid sub-tropical for the dry regions;

(3) Warm climate that can be described as humid subtropical for the humid regions (warm summer), humid sub-tropical/humid continental (warm summer) for the dry regions, and, dry summer sub-tropical (Mediterranean) for the marine regions;

(4) Mixed climate that can described as humid sub-tropical/humid continental (warm summer) for the humid regions, semi-arid middle latitude/arid sub-tropical/highlands for the dry regions, and marine (cold summer) for the marine regions;

(5) Cool climate that can be described as humid continental (warm summer) for the humid regions, semi-arid middle latitude/highlands for the dry regions, and, Marine (cool summer) for the marine regions;

(6) Cold climate that can described as humid continental (warm summer/cool summer) for the humid regions, and, semi-arid middle latitude/highlands for the dry regions;

(7) Very cold climate that can be described as humid continental (cool summer).
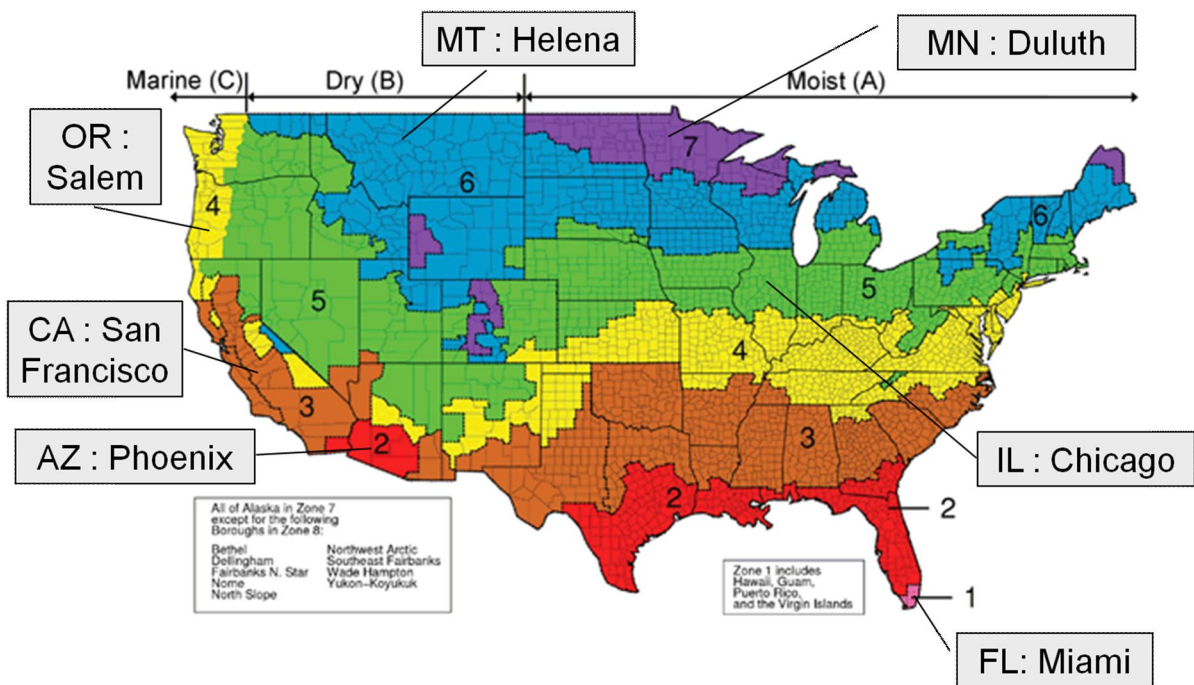
Fig. 5.7. Seven climate zones and their representative cities in the U.S. (numbers from 1 to 7 in the figure indicate the zone number).

In each climate zone, a representative city was selected for detailed numerical analysis. Figure 5.7 shows these seven climate zones and their corresponding representative cities. These representative cities and their typical daily weather data are listed in Table 5.3. These data were

120

used in the numerical analyses of the energy efficiency of different window types installed in the simulated buildings.

Table 5.3. Location and the assumed day climate conditions in the seven typical cities in the U.S.

City	Site locations			Summer/Winter day Outdoor dry-bulb temperature (°C)
	Latitude(°)	Longitude(°)	Altitude(m)	
Duluth	N46.83	W92.22	433	32.2/–32.1
Helena	N46.6	W111.97	1167	36.8/–29.8
Chicago	N41.78	W87.75	190	35.7/–24.2
Salem	N44.9	W123	60	39.7/–15.9
San Francisco	N37.62	W122.38	5	34.7/ 1.4
Phoenix	N33.68	W112.08	450	37.4/–1.2
Miami	N25.65	W80.43	3	40.1/3.2
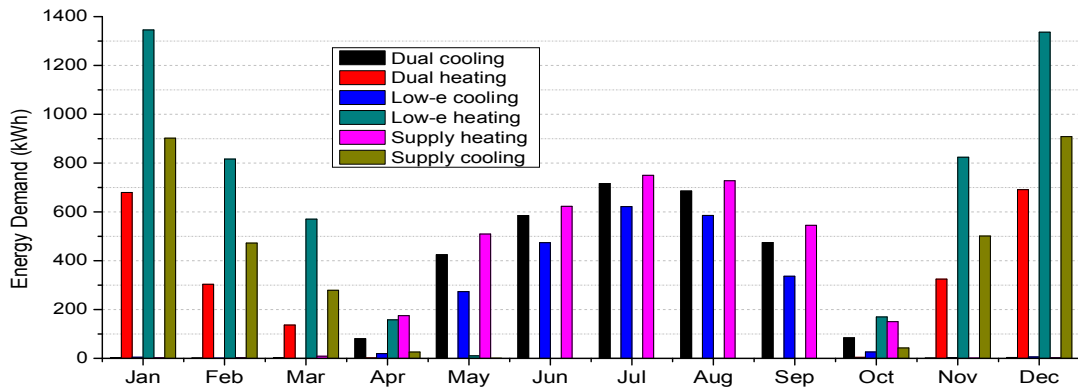
a)   Apartment
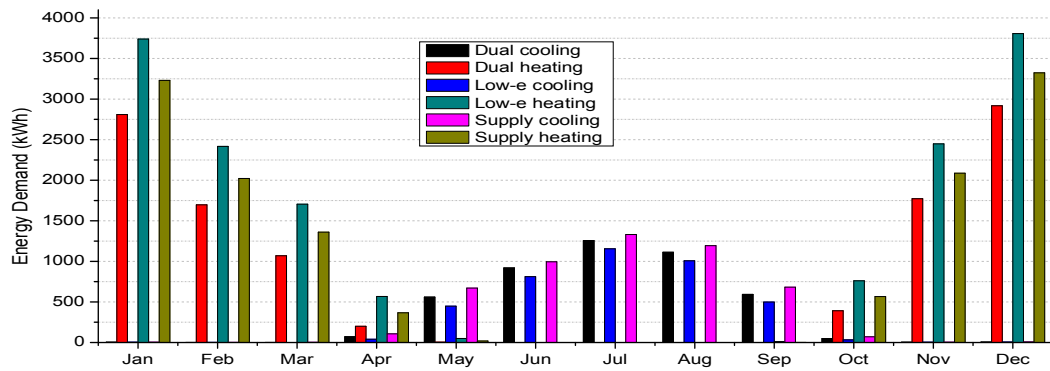
b)   Detached house

Fig. 5.8. Monthly energy demand with the three types of windows in Duluth
(a) an apartment, (b) a detached house

121

Using the modified EnergyPlus program, detailed numerical simulations were conducted to evaluate the energy efficiency of different windows installed in buildings in different climates. Detailed numerical results for Duluth, Minnesota, in zone 7, and Miami, Florida, in zone 1 are presented together with the summary results for all other climate zones. The detailed results for Zones 2–6 are provided in Appendix B.

Figure 5.8 shows the monthly building energy demand for three types of windows for Duluth located in the very cold climate region (zone 7). The charts in the figures show that heating is required from October to April and cooling from April to October for both buildings. In the months of April and October, the buildings require heating as well as cooling loads because there are warm days and cool nights.

In the heating season, the buildings with dual-airflow windows required the least heating energy, and those with the low-e windows required the most. The dual-airflow windows had the advantage of the three-layer glazing construction and the capability for heat recovery that led to better energy efficiency for the buildings. Low-e windows are not designed with heat recycling capability, which make them less effective in terms of energy efficiency. However, the supply-airflow windows could save some ventilation energy. This was because the cold air from outdoors could absorb some solar heat energy as the supply air channeled into the indoor spaces through the cavity between the glass panes. Dual-airflow windows could save even more heat energy than supply-airflow windows because the heat exchange between the supply airflow and the exhaust airflow in the dual-airflow window was higher than that of the supply-airflow window, which only had a single stream of air supply.

The energy demand for cooling during the warmer season showed a different trend. According to the simulated results, the buildings with dual-airflow windows used slightly more

energy than those with the low-e windows and the supply airflow windows. This was because the supply air from outdoors absorbed heat energy by solar radiation as it was driven through the window cavity. In addition, more electrical energy was consumed to drive the extra fan unit for the supply airflow. As a result, the ventilated windows were expected to use more energy for cooling than the low-e windows. It may therefore be suggested that only one fan unit be used in order to reduce electrical energy consumption, while still providing a stable airflow rate to achieve an acceptable IAQ.

Comparing the two charts in Fig. 5.8, the energy saving achieved by the dual-airflow windows during the heating season was larger in the apartment than in the detached house. This was because the energy demand in the space near the windows accounted for a larger percentage of the total energy demand for the entire apartment. A smaller floor area and less heat energy transfer through external walls implied that there is a good potential to obtain energy savings by using a better window design. To summarize, the installation of dual-airflow windows in the apartment saved 59.1% more heating energy than conventional windows. The heating energy savings were only 38.8% over the supply-airflow windows. In the detached house, the heating energy savings were 29.9% and 16.3% over the conventional windows and supply-airflow windows, respectively.

In contrast, the buildings with the dual-airflow windows consumed more total energy than those with the other two types of windows. Using conventional windows, the savings in cooling energy from conventional windows were 30.2% in the apartment and 14.2% in the detached house. For the supply-airflow window, the savings were 12.2% and 9.7%, respectively.

Miami, Florida, was the representative city selected for climate zone 1, a very hot and humid region. It has tropical weather with a long summer and a very short, mild winter. Figure

123

5.9 shows the monthly energy demand for the simulated buildings in Miami. In particular, it was assumed that only cooling energy was required in the buildings. Furthermore, it was also assumed that the variations in the cooling energy demand for different months did not change significantly. These were reasonable assumptions because Miami is located in a tropical zone surrounded by oceans, and the range of fluctuation in outdoor temperatures is rather small.

a) Apartment
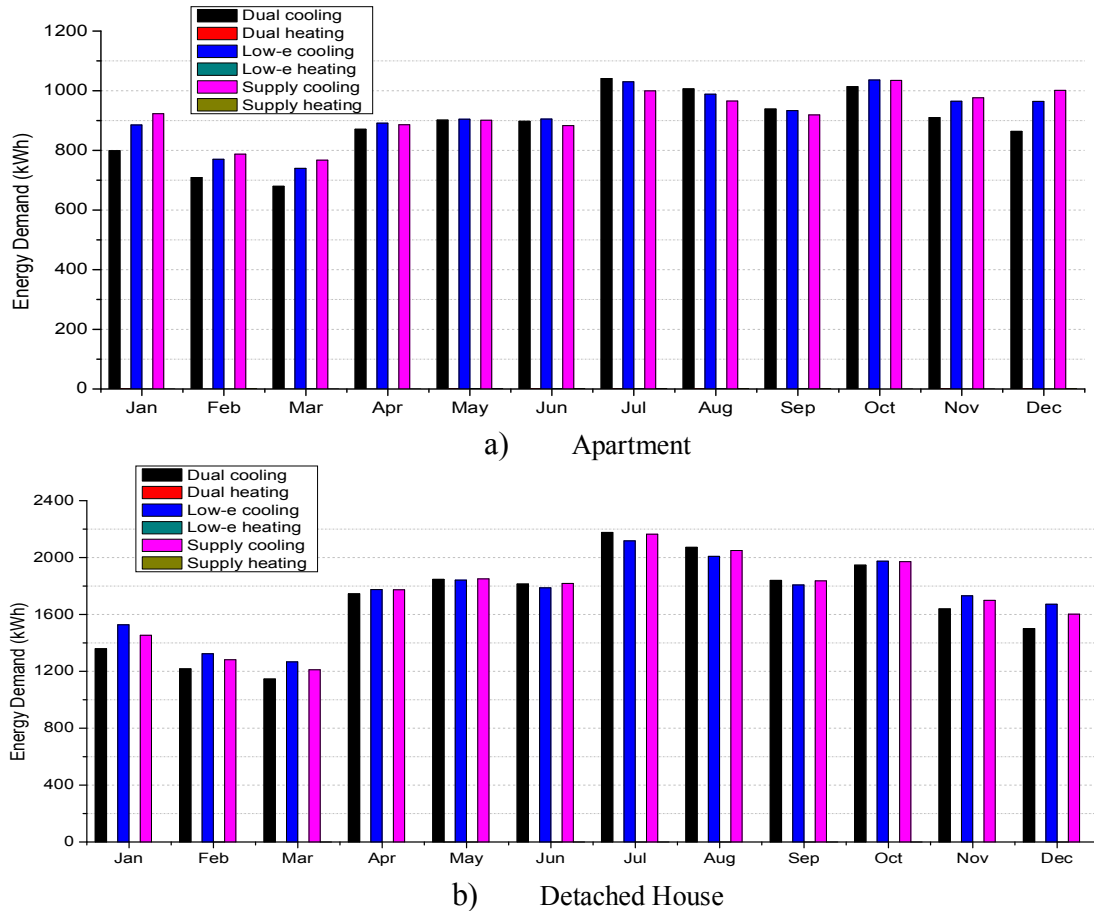
b) Detached House

Fig. 5.9. Monthly energy demand with the three types of windows in Miami
(a) an apartment, (b) a detached house.

Between October and April, the buildings with dual-airflow windows required the least cooling energy, and those with supply-airflow windows consumed the most energy. Between May and June, there was very little difference in the cooling energy demand for buildings with different types of windows. Between July and September, the dual-airflow windows used the

most cooling energy and conventional windows used the least. These simulation results confirmed that energy conservation from either dual-airflow windows or supply-airflow windows is not sufficient to compensate for the additional solar heat gain during the summer in Miami.

The simulation results for Miami can be summarized as follows. The use of dual-airflow windows in an apartment can save 3.5% of the required annual electrical energy over conventional windows and 3.7% over supply-airflow windows. For the detached house, the benefit of using the dual-airflow windows was shown to be less effective. The annual energy savings were reduced to 2.5% for conventional windows and 2% for the dual-airflow windows.

Table 5.4. Annual energy efficiency in the apartment.

a) Heating energy demand and their relative energy saving

City	Heating energy demand (kWh)			Relative heating saving (%)	
	Dual-airflow	Conventional	Supply	Conventional	Supply
Duluth	2141	5229	3497	59.1	38.8
Helena	829	2953	1445	71.9	42.6
Chicago	912	2906	1585	68.6	42.4
Salem	159	1180	455	86	65
San Fran.	0	3	1	-	-
Phoenix	0	1	0	-	-
Miami	0	1	0	-	-

b) Cooling energy demand and their relative energy saving

City	Cooling energy demand (kWh)			Relative cooling saving (%)	
	Dual-airflow	Conventional	Supply	Dual-airflow	Conventional
Duluth	3062	2351	3132	-30.2	2.2
Helena	3987	3162	4551	-26.1	12.4
Chicago	4354	3769	4788	-15.5	9.1
Salem	4475	3542	5024	-26	11
San Fran.	5424	3872	6370	-40.1	14.9
Phoenix	12446	12285	12677	-1.3	1.8
Miami	10631	11013	11044	3.5	3.7

Similar numerical simulations were conducted for other representative cities in the climate

zones 2–6. These cities were Helena, Montana, for zone 2; Chicago, Illinois, for zone 3; Salem, Oregon, for zone 4; San Francisco, California, for zone 5; and Phoenix, Arizona, for zone 6. The full results of these simulations can be found in Appendix B. Nevertheless, Tables 5.4 and 5.5 list the estimated monthly energy demand (both cooling and heating) and the energy savings for the apartment and the detached house, respectively.

Table 5.5 Annual energy efficiency in the detached house.
a) Heating energy demand and their relative energy saving

City	Heating energy demand (kWh)			Relative heating saving (%)	
	Dual-airflow	Conventional	Supply	Dual-airflow	Conventional
Duluth	10865	15506	12975	29.9	16.3
Helena	6214	9811	7819	36.7	20.5
Chicago	6115	9307	7634	34.3	19.9
Salem	2896	4896	3807	40.8	23.9
San Fran.	129	592	325	78.3	60.4
Phoenix	0	9	0	-	-
Miami	0	1	0	-	-

b) Cooling energy demand and their relative energy saving

City	Cooling energy demand (kWh)			Relative cooling saving (%)	
	Dual-airflow	Conventional	Supply	Dual-airflow	Conventional
Duluth	4581	4012	5073	−14.2	9.7
Helena	6344	5765	6918	−10.1	8.2
Chicago	7195	6736	7637	−6.8	5.8
Salem	6871	6172	7501	−11.3	8.4
San Fran.	6699	5561	7851	−20.5	14.7
Phoenix	24132	24056	24449	−3.1	1.3
Miami	20303	20833	20710	2.5	2

According to Tables 5.4 and 5.5, the dual-airflow windows performed better in Duluth, Helena, Chicago, and Salem. This was because the heating energy demand in these four cities was higher. Hence, dual-airflow windows could save more energy during the heating season. In general, the demand for heating energy was rather limited in San Francisco, Phoenix, and Miami.

126

It was clear that the apartment and the detached house with the dual-airflow windows consumed more energy than those with conventional windows. Therefore, it was suggested that dual-airflow windows should not be used in these three climate zones if energy conservation is the prime motivation.

5.4 Conclusions

A modified EnergyPlus program was developed to simulate the energy efficiency of three types of windows, (a) low-emissivity double-pane windows, (b) supply-airflow windows, and (c) dual-airflow windows. The computed results obtained from the numerical model were compared with a series of field experiments conducted in a test cell which was located in the northeastern part of China at Harbin. Extensive comparisons confirmed the validity of the modified EnergyPlus program to simulate the energy efficiency of these windows.

The modified EnergyPlus program was then used to simulate the energy efficiency of these windows installed in apartments and detached houses located in different climate zones in the U.S. Seven representative cities were selected with each of these cities represents a typical climate zone in the U.S. The numerical study indicated that the dual-airflow windows can achieve greater energy savings in the heating season than in the cooling season. As a result, dual-airflow windows were shown to be more effective for energy conservation in colder climate regions than in warmer climate regions.

References

ANSI/ASHARE, 2001. "Ventilation for acceptable indoor air quality," Standard 62-2001.

P. H. Baker, M. McEvoy, 2000. "Test cell analysis of the use of a supply air window as a passive solar component," *Solar Energy* **69**, 113–130.

R. S. Briggs, R. G. Lucas, T. Taylor, 2003. "Climate Classification for Building Energy Codes and Standards: Part 1 - Development Process," *Technical and Symposium Papers, ASHRAE Winter Meeting*, Chicago, IL, January, 2003.

R. S. Briggs, R. G. Lucas, T. Taylor, 2003. "Climate Classification for Building Energy Codes and Standards: Part 2 - Zone Definitions, Maps and Comparisons," *Technical and Symposium Papers, ASHRAE Winter Meeting*, Chicago, IL, January, 2003.

S. Doty, W. C. Turner, 2009. *Energy Management Handbook*. The Fairmont Press Inc. 2009.

S. Dutton, L. Shao, and S. Riffat, 2008. "Validation and parametric analysis of EnergyPlus: Air flow network model using CONTAM," *3rd National Conference of IBPSA – USA, Berkeley, California, July 30 – August 1, 2008.*

J. R. Gosselin, Q. Chen, 2008a "A computational method for calculating heat transfer and airflow through a dual-airflow window," *Energy and Buildings* **40**, 452-458.

J. R. Gosselin, Q. Chen, 2008b. "A dual-airflow window for indoor air quality improvement and energy conservation in buildings," *HVAC&R Research* **14**, 359-372.

J. J. Liu, B. Wang, Y. H. Xu, 2007. "Research on the energy saving performance of the enthalpy recovery ventilator in Chinese residential buildings," *International Solar Energy Conference* **6**, 595-602.

Q. M. Luo, 2007. "Impacts of ventilation strategies on IAQ," *Refrigeration Air Conditioning & Electric* **2,** 14-18.

D. Saelens, S. Roels, H. Hens, 2003. "On the influence of the inlet temperature in multiple-skin facade modeling," *Eighth International IBPSA Conference* **8**, Eindhoven, Netherlands, 11-14.

D. Saelens, S. Roels, H. Hens, 2008. "Strategies to improve the energy performance of multiple-skin facades," *Building and Environment* **43**, 638-650.

J. M. Shen, (2007) "Indoor air quality and health," *Refrigerating Technology* **1**, 10-14.

M. H. Sherman, N. Matson, 1997. "Residential ventilation and energy characteristics," *ASHRAE Transactions* **103**, 717-730.

R. K. Strand, C. O. Pedersen, 1997. "Implementation of a radiant heating and cooling model into an integrated building energy analysis program," *ASHRAE Transactions* **103**, 949-958.

R. K. Strand, D. B. Crawley, L. K. Lawrie, F. C. Winkelmann, W. F. Buhl, Y. J. Huang, D. E. Fisher, 2000. "EnergyPlus: A new-generation energy analysis and load calculation engine for building design," *Proceedings of the ACSA Technology Conference on EnergyPlus*, Cambridge, Massachusetts, 1-12.

A. Tzempelikos, 2008. "The impact of venetian blind geometry and tilt angle on view, direct light transmission and interior illuminance," *Solar Energy* **82**, 1172–1191.

A. Werner, A. Roos, 2008. "Simulations of coatings to avoid external condensation on low U-value windows," *Optical Materials* **30**, 968–978.

A. Yezioro, B. Dong, F. Leite, 2008. "An applied artificial intelligence approach towards assessing building performance simulation tools," *Energy and Buildings* **40**, 612-620.

K. Zhong, Y. M. Kang, 2009. "Applicability of air-to-air heat recovery ventilators in China," *Applied Thermal Engineering* **29**, 830-840.

Chapter 6: Assessment of the effects of infiltration and mechanical ventilation on IAQ

6.1 Introduction

A dual-airflow window can be treated as a heat exchanger, and it can save energy by heat recovery. In the last chapter, the energy conservation ability of dual-airflow windows was explored by numerical simulations and experimental measurements. In the numerical analyses, a stable airflow rate was assumed where a minimum fresh air volume for each occupant was used to ensure acceptable IAQ.

It is well known that the IAQ has a direct correlation with the indoor contaminant release rate and the indoor/outdoor air exchange rate (Jokl, 2000). The problem of sub-standard IAQ has been mitigated by the development of green building materials and by the introduction of better ventilation strategies (Luo, 2007). However, to save energy demand, buildings are built more air-tight to reduce demand for ventilation energy. However, this tighter envelop has led to the so-called sick building syndrome that affects the health and work efficiency of building occupants. A sufficient supply of outdoor fresh air is needed in order to dilute indoor contaminants.

Carbon dioxide (CO_2) is generated continuously by building occupants. However, the concentration of CO_2 is generally stable outdoors. Thus, CO_2 concentration is a good indicator to evaluating the relationship between IAQ and the ventilation rate (Leephaakpreeda, 2001). The American Society of Heating, Refrigerating, and Air Conditioning Engineers (ASHRAE) has suggested a standard for acceptable indoor CO_2 concentration to be less than 1000 ppm (Seppanen, 1999).

Chapter 6 is devoted to the study of the IAQ under different ventilation approaches. The advantages of using dual-airflow windows for improving IAQ were examined. In particular, CO_2

was used as the tracer gas for studying the IAQ in residential buildings under different modes of ventilation.

6.2 Ventilation modes in residential buildings

In many residential buildings, natural ventilation, i.e., infiltration, is the major mechanism allowing air exchange between indoor and outdoor spaces. The fresh air supply rate due to infiltration is dependent on outdoor weather conditions and the air-tightness of the building. Use of infiltration to improve IAQ may not meet national standards for the occupants. Open windows for natural ventilation can only be used effectively in mild weather because during the heating/cooling seasons, there is a large temperature difference between indoor and outdoor spaces (Jokl, 1996).

Exhaust fans are used in bathrooms and kitchens to exhaust indoor air to the outdoor environment. However, their use is normally not an attractive option for enhancing indoor/outdoor air exchanges. Mechanical ventilation systems have been suggested to meet the demand for indoor fresh air (Jokl, 1999). As studied in Chapter 5, supply-airflow and dual-airflow windows have fans to bring in outside air. They represent two alternative strategies for indoor mechanical ventilation. Their ability for heat recovery was studied in Chapter 5, and their ventilation performance are reported in the following sections.

As shown in Fig. 6.1(a), the supply-airflow window is driven by a supply fan (Zheng and Qi, 2002). The fan provides a positive indoor pressure to force indoor air to the outdoor space. The supply air flows indoors passing through the cavity between interior and exterior glass panes. The airflow can exchange heat energy with the indoor space through the interior glass pane to adjust the temperature of the supply air. The air in the cavity can absorb heat from the

131

warmer indoor air in the heating season and can be cooled in the cooling season to save energy.

(a) Supply-airflow window   (b) Dual-airflow window
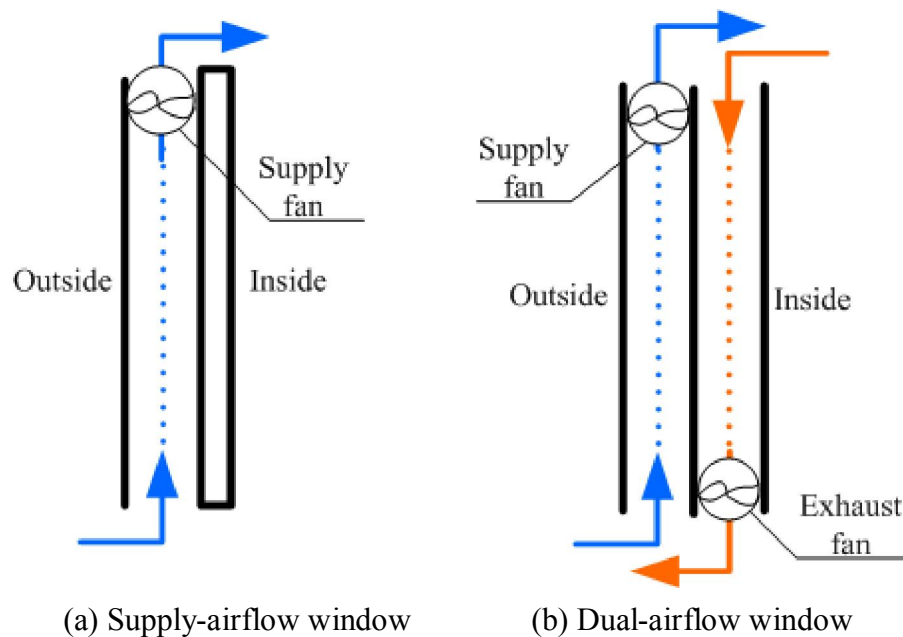
Fig. 6.1 Ventilation of airflow windows.

However, the dual-airflow window [see Fig. 5-.1(b)] has a supply and an exhaust fan (Wei et al., 2010). Outdoor air is brought into the indoor space by the supply fan, and indoor air is ejected to the outdoor environment by the exhaust fan. The supply airflow between the exterior glass pane and middle glass pane can exchange heat with the exhaust airflow between the middle glass pane and interior glass pane. This arrangement enables a decrease in energy usage by the fresh air ventilation. The IAQ under different ventilation approaches are reported in the following sections.

6.3 Models used for studying IAQ

The IAQ is often studied by experimental methods or numerical simulations. A tracer gas is usually used in the experimental methods to monitor the ventilation rate or the airflow distribution in an indoor space. However, the experimental approach is both time-consuming and

expensive and is therefore limited to a more fundamental investigation. There are two popular approaches for numerical simulations: a computational fluid dynamics (CFD) scheme or a multi-zone airflow model. The CFD method can be used to study the airflow or the distribution of contaminants in a more detail, but it can only be used to simulate time-dependent situations. A multi-zone model method can be used to calculate the mean levels of the ventilation rate, the indoor temperature, and the concentration of the contaminants in the indoor space. The multi-zone model can also be used to obtain a dynamic simulation for a short period. The purpose of the current study is to compare the changes in the contaminant concentration for different ventilation approaches instead of investigating the distribution of contaminants in the indoor space. As a result, the multi-zone method is used in favor of the CFD scheme.

The National Institute of Standards and Technology (NIST) has developed a multi-zone simulation tool known as CONTAM. It can be used to simulate airflow between neighboring zones effectively which allows the simulation of natural ventilation driven by a thermal gradient or wind pressure difference. CONTAM can also be used to simulate mechanical ventilation.
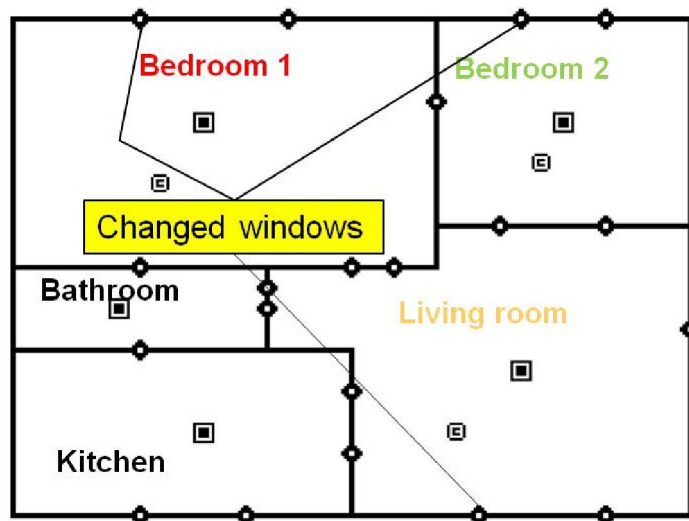
(a)   Apartment
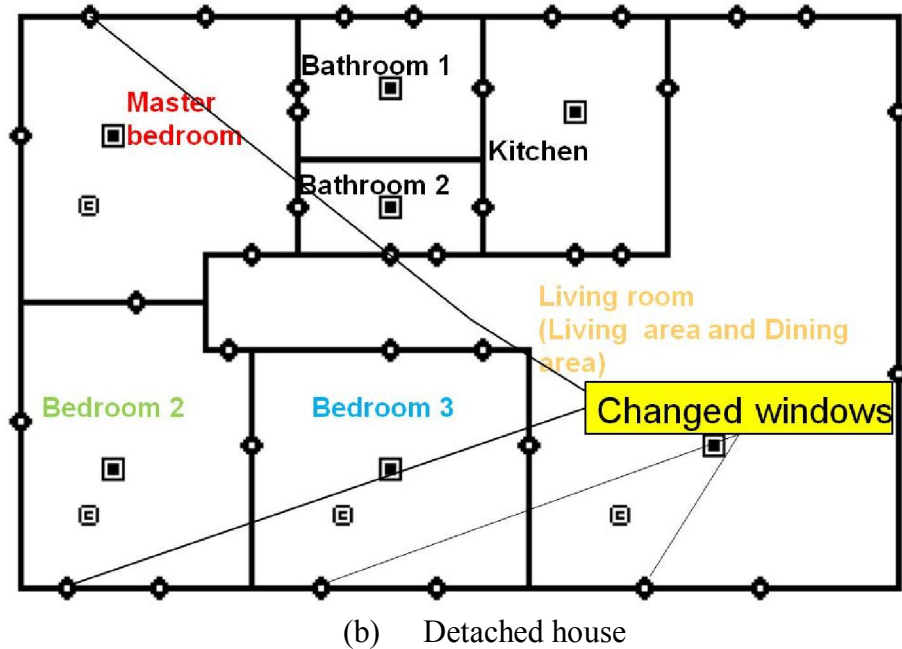
(b)   Detached house

Fig. 6.2. Building model in CONTAM (a) apartment, (b) detached house.

The multi-zone airflow simulation program CONTAM was used to study the air and contaminant exchanges between indoor and outdoor spaces as well as the exchanges between the neighboring rooms in the building. Again, the same apartment and detached house used in Chapter 5 were selected for use in CONTAM. The floor area of the apartment and the detached house were 80 m^2 and 200 m^2, respectively. Different ventilation modes were considered in the numerical analyses, and they are reported separately. The models for the apartment and the detached house used in CONTAM are shown in Fig. 6.2.

In the CONTAM multi-zone airflow simulation, each room was treated as a separate zone. The indoor air temperature, airflow velocity, and contaminant concentration were considered to be uniform within each zone, but these parametric values were different for different zones. All exterior joints between wall/ceiling/floor, windows, and doors were modeled as airflow paths. The size of each room (including all windows, if applicable) in the buildings is listed in Table 6.1

for information.

Table 6.1 Sizes of the apartment and the detached house used in simulations.

	Apartment	House	Ventilated window	North conventional window in the apartment	South conventional window in the apartment	North conventional window in the house	South conventional window in the house	PVC frame
length (m)	10	20	-	-	-	-	-	-
width (m)	8	10	1	2.2	4.8	7.3	11	0.08
height (m)	2.6	2.8	1.5	1.5	1.5	1.5	1.5	-

The rate of ventilation in a building by either infiltration or other mechanical means is dependent on the air-tightness profile of the building. The rates of air leakage through different joints in the buildings are listed in Table 6.1. These parametric values were taken from the *ASHRAE Handbook 2007*.

The generation of CO_2 by occupants was considered in this study. The generation rates for an adult and a child were assumed to be 0.005 liter/s and 0.003 liter/s, respectively (Jokl, 2000). A further assumption was made that there were 2 adults and 2 children in the detached house and 2 adults and 1 child in the apartment. Based on this assumption, the generation rate of CO_2 indoors could be estimated. The outdoor CO_2 level of concentration was constant at 380 ppm throughout.

Table 6.2 Parameters of air paths in the building.

Exterior joint (cm^2/m^2)			Interior wall (cm^2/m^2)	Interior door (cm^2/ea)	Exterior door (cm^2/ea)
Ceiling-wall	Wall-wall	Floor-wall			
0.5	2.5	0.8	2	75	12

6.4 Analysis of IAQ under natural ventilation

Natural ventilation has a direct correlation with outdoor weather conditions because its main mechanism is because of the presence of thermal and/or wind pressure gradients. In the present study, the natural infiltration rate from exterior windows is calculated by

$$Q = C(\Delta P)^n \tag{6.1}$$

where C is the infiltration airflow coefficient, ΔP is the difference in the indoor and outdoor pressures and n is the air infiltration exponent. According to *ASHARE Handbook 2007*, $\underline{Q}$ is measured in m^3/s, ΔP is taken as 0.015 $m^3/(s, pa^n)$, and n has a parametric value of 0.65 for a residential building.

Natural ventilation (i.e., infiltration) is expected to vary significantly in different climate zones at different seasons for different types of buildings with various sizes of airflow paths. Initially, numerical simulations of infiltration were conducted for different seasons in one climate zone for the apartment and the detached house. It was found to be unnecessary to simulate ventilation performance for all climate zones, because the infiltration was mainly influenced by temperature differences and wind speeds. The difference in the ventilation performances in different climate zones can be represented by simulations in one climate zone in different seasons. Since climate zone 7 has the largest temperature differences between the indoor and outdoor spaces during the heating and cooling seasons, Duluth (the representative city of zone 7) was therefore selected for conducting the numerical simulations. As shown in the weather data for Duluth, February was the coldest month, and July was the warmest. Hence, the respective numerical results for these two months are presented.

Figure 6.3 shows the change in CO_2 concentration for the detached house in February and in July. The numerical results suggest that in these two months the indoor CO_2 concentration in the

detached house was well above 1000 ppm. It should be noted that the acceptable level for indoor CO_2 concentration is below 1000 ppm. Hence, for the detached house, the ventilation rate provided by infiltration alone could not introduce sufficient outdoor fresh air into the indoor space for diluting the CO_2 concentration to the acceptable level.

Date: Feb 01 – Feb 28
(a)   February

Date: Jul 01 – Jul 28
(b)   July
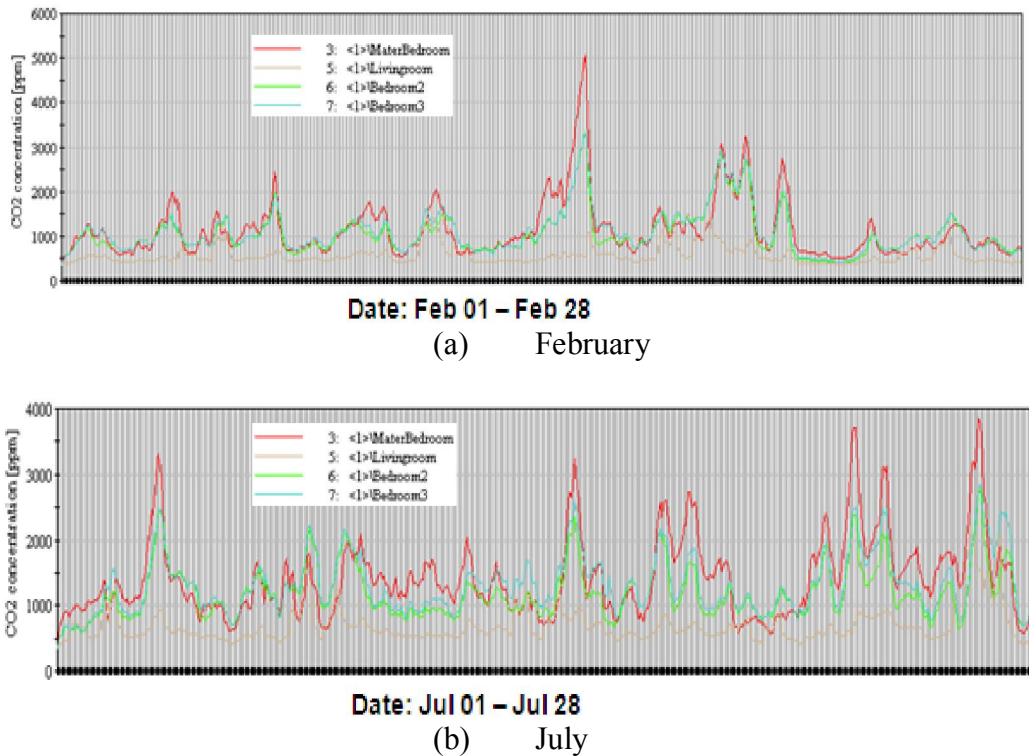
Fig. 6.3. Variations of the indoor CO_2 concentration in the detached house in Duluth; (a) the coldest month, February, (b) the warmest month, July.

It is worth pointing out that weather data (not shown in this report for brevity) suggested that wind speeds and direction played an important role in infiltration. These factors were reflected in the simulation results. As shown in Figs. 6.3a and 6.3b, the fluctuation in the CO_2 concentration was quite significant throughout these two month-long periods. Although the variations in temperatures for these two months were small, there were considerable fluctuations in wind speed and direction that caused significant variations in indoor CO_2 concentration.
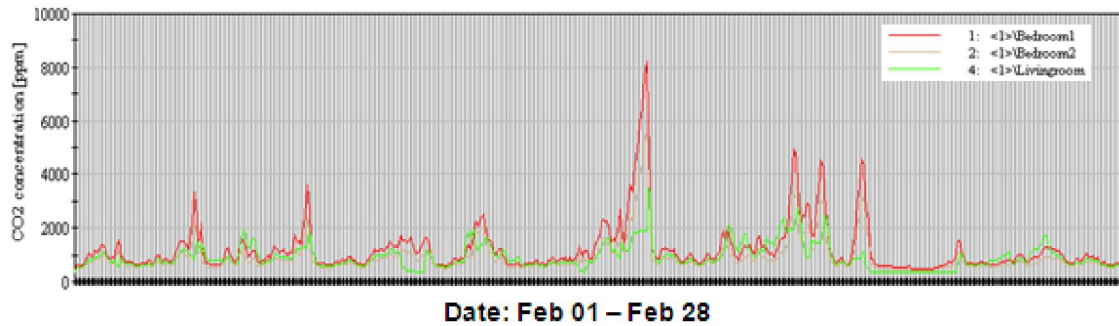
Fig. 6.4. Variations of the indoor CO_2 concentration in the apartment in Duluth.

Figure 6.4 shows the CO_2 concentration in the apartment in February. Compared with Fig. 6.3(a), the average and peak CO_2 concentration in the apartment was higher than that in the detached house. This was because the CO_2 concentration is dependent on the building area and the airflow path sizes. The larger volume per occupant of the detached house results in a lower CO_2 concentration for the same generation rate of CO_2 per occupant. In addition, the house has more air leakage and thus a larger infiltration volume. Hence, if infiltration cannot provide an acceptable level of the IAQ in the detached house, then the conditions cannot be met in the apartment. Consequently, it is only necessary to show the simulation results for the apartment because the results for the detached house show a similar trend.

Next, the simulation results for infiltration in different seasons in Duluth are presented. Specifically, the predictions of the variations in CO_2 concentration for January, April, and July are shown in Fig. 6.5. These three months are chosen to represent the heating, mild, and cooling seasons respectively. For clarity of presentation, only one week of data from the ninth through the fifteenth day of each month was selected for the analyses. It can be observed that infiltration cannot reduce CO_2 concentration to an acceptable level, i.e., below 1000 ppm, for all seasons. Nevertheless, the infiltration in these three months can be ranked with July the most, and January the least.

138
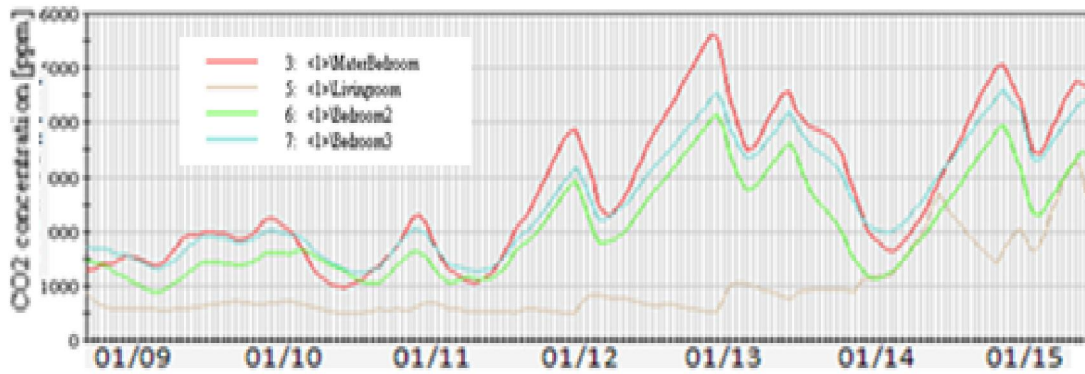
a) January, heating season
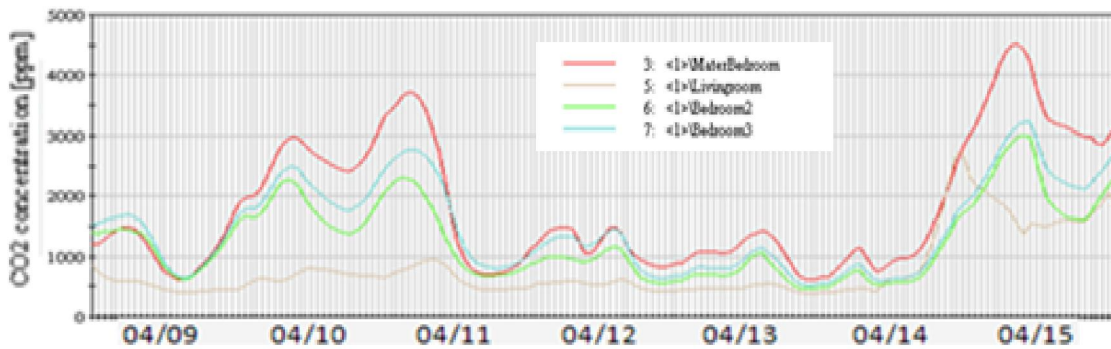
b) April, mild season
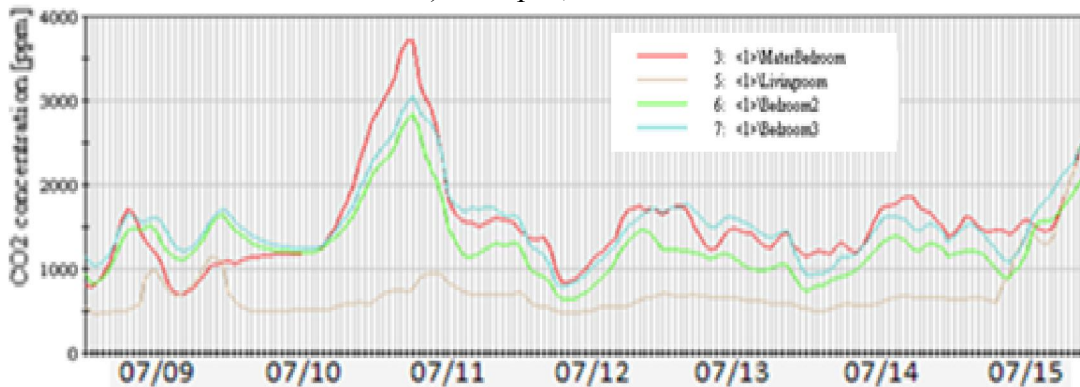
c) July, cooling season

Fig. 6.5. Indoor CO_2 concentration changed by infiltration in the house in Duluth in different season.

In addition to the predicted results for CO_2 concentrations in different seasons, variations in outdoor air temperature and outdoor wind speed are shown in Figs. 6.6. Again, only one week of data for outdoor air temperature and wind speed are shown. The fluctuation in temperature over the one-week period was relatively small, but the variation in wind speed was much more

significant over the same period. These data can be used to explain the daily variations in infiltration. The average wind speed in January was the lowest in these three months, which serves to explain why the indoor CO_2 concentration was highest in that month. The absence of a strong pressure gradient led to a less infiltration in January.
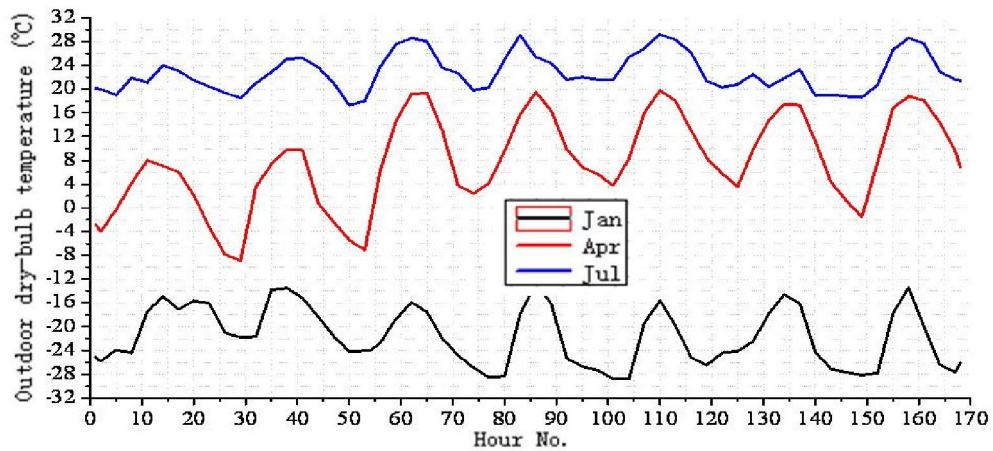
a)   Outdoor dry bulb temperature
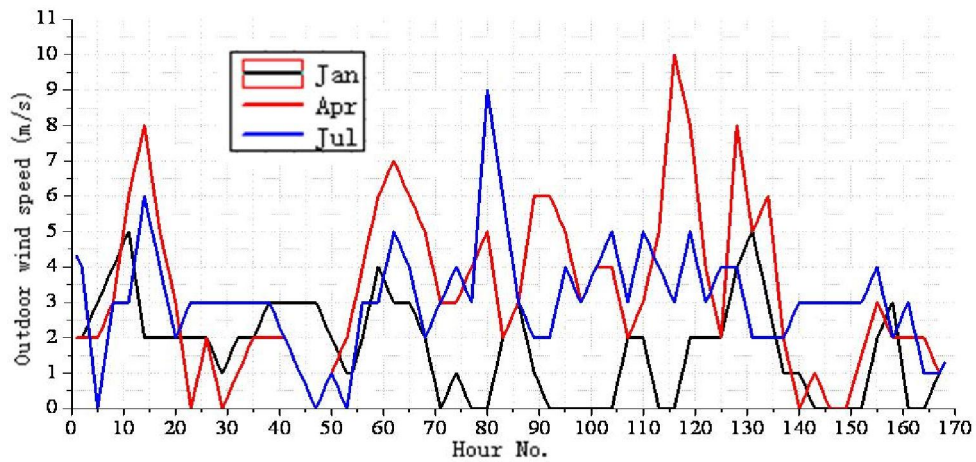
b)   Outdoor wind speed

Fig. 6.6. The weather data from the ninth day to the fifteenth day in January, April and July in Duluth, (a) outdoor temperature, (b) outdoor wind speed.

To a certain extent, the outdoor air temperature was a good indicator of the locations of the climate zones described in Chapter 5. However, the above weather data and simulation results demonstrated that outdoor air temperature could affect infiltration, but it was not a key factor. It

was therefore inappropriate to use outdoor air temperature (and, hence, the climate zone) as an indicator of infiltration. To illustrate this point, comparable simulations for indoor CO_2 concentration were conducted for Miami, the representative city for climate zone 1.
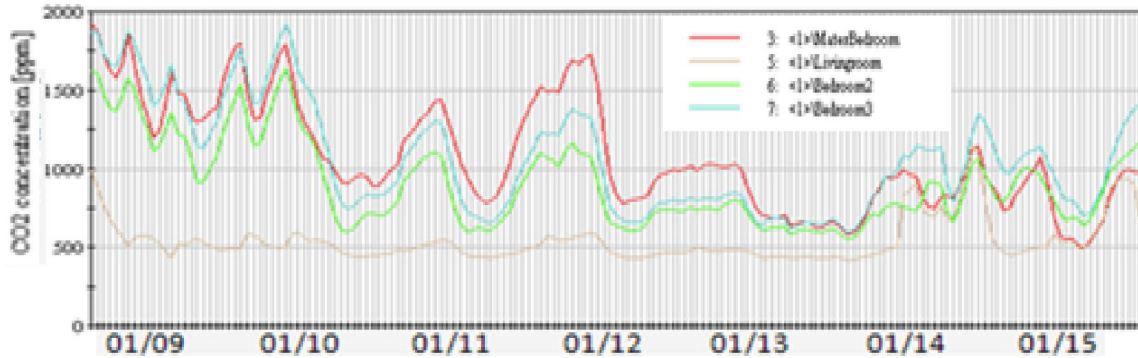
a)   January
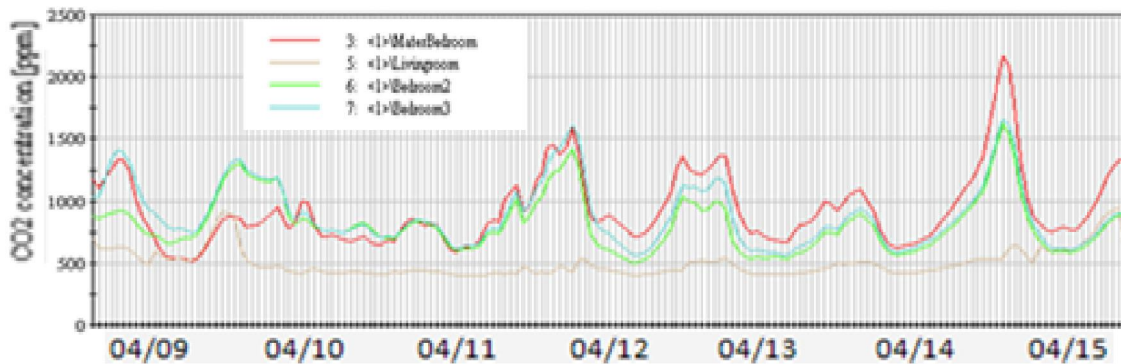
b)   April
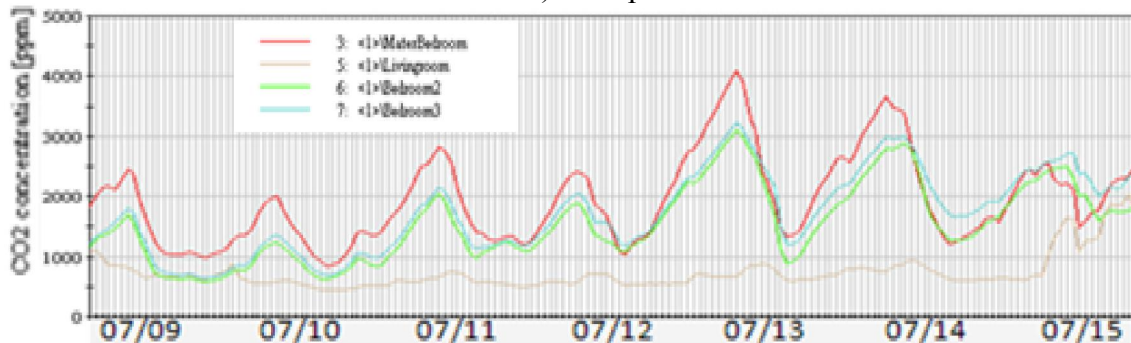
c)   July

Fig. 6.7. Predicted indoor CO_2 concentration by infiltration in the detached house in Miami in different seasons

Figure 6.7 shows indoor CO_2 concentration during different seasons in Miami for the detached house. Again, January was selected for the heating season, April for the mild season,

and July for the cooling season. Infiltration was assumed the main mode of ventilation for the detached house. According to the numerical simulations, CO_2 concentration was below 1000 ppm most days in January and April. In July CO_2 concentration was above 1000 ppm for most periods. An examination of weather data (results not shown here for brevity) indicates that wind speeds were lower in July than in the other two months.

Table 6.3 Predicted IAQ for a detached house with
natural ventilation in climate zones 2–6 for different seasons.

City	January			April			July		
	ΔT	W_m	H	ΔT	W_m	H	ΔT	W_m	H
(2) Phoenix	18	6.9	168	9	7.9	162	17.1	7.1	166
(3) San Francisco	17.2	7	155	13.9	7.2	164	8.9	7.9	167
(4) Salem	19.6	6.9	118	18.9	6.8	151	9.9	7.6	168
(5) Chicago	34.4	5.1	79	19.4	6.7	149	11.6	7.5	168
(6) Helena	42.8	4.8	129	32.2	5.2	165	.3	7.8	164

[Keys : ΔT (in °C) is the maximum temperature between indoor and outdoor spaces; W_m (in m/s) is the minimum outdoor wind velocity); H (in hours) is the number of hours that the indoor CO_2 concentration is higher than 1000 ppm, i.e. does not meet the acceptable standard for IAQ]

A series of numerical simulations was conducted for Phoenix, San Francisco, Salem, Chicago, and Helena, which are representative cities for climate zones 2 through 6, respectively. Based on weather conditions, indoor CO_2 concentrations were computed for these representative cities. Table 6.3 lists the number of hours (H) when the indoor CO_2 concentration was above 1000 ppm for each city. When the CO_2 concentration was higher than 1000 ppm, the IAQ of the detached house was regarded as not meeting the acceptable standard. As can be observed from Table 6.3, Chicago in January was the only case in which H reached the acceptable level of CO_2 concentration below 1000 ppm more than 50% of the time. In all other representative cities, ventilation by infiltration was simply unsatisfactory in providing an acceptable level of IAQ with

regard to CO_2 concentration.

6.5 Analysis of IAQ under mechanical ventilation

In mild weather, it is possible to open windows to increase infiltration and improve ventilation. However, this method cannot solve the problem of poor IAQ during the heating and cooling seasons. In these cases, mechanical ventilation is often the only means to reduce CO_2 concentration and improve IAQ.

In this section, three types of mechanical ventilation systems are considered. First, exhaust fans installed in the bathroom and kitchen are a direct method to increase the air ventilation rate and improve IAQ. This method is based on an indoor environment with a negative pressure. In the numerical analyses, all interior doors of the apartment were assumed to be open to facilitate indoor air exchange when the occupants were in the living room. However, the bedroom doors were assumed to be closed when the occupants were in the bedrooms.

Figure 6.8 shows the indoor CO_2 concentration in the apartment for a one-week period with an exhaust fan running continuously in either the kitchen or the bathroom. The simulation results of these two modes depict a similar changing trend, which means these two modes of operation led to comparable indoor pressure environments. At different times of the same day, CO_2 concentration showed a high level of fluctuation. This was largely because of the fact that the interior doors were typically the main pathways of indoor airflow. When the doors were closed, the exhaust fan could not provide a sufficient pressure drop in bedrooms, and hence, the process of infiltration was limited. When the doors were opened, the indoor airflow exchange rate varied according to the pressure difference between different rooms. The living room had no interior doors. This environment permitted a stable airflow rate throughout the day in the living room

resulting in better IAQ than other rooms in the apartment. Nevertheless, exhaust fans in bathroom and kitchen could not provide for acceptable IAQ in other parts of the apartment.

a)   Bathroom exhaust fan

b)   Kitchen exhaust fan
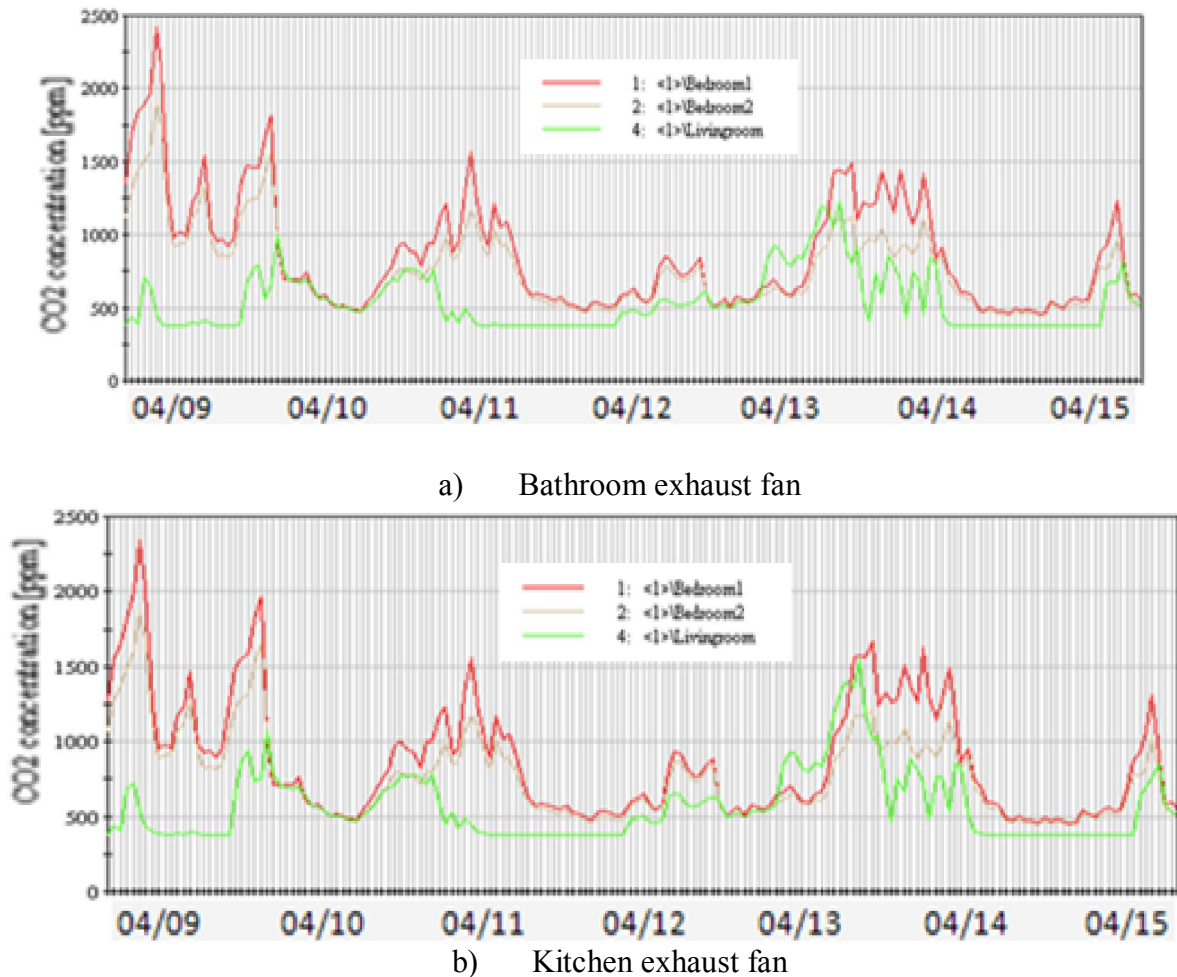
Fig. 6.8. Predicted indoor CO_2 concentration in April with an exhaust fan mounted
(a) in the bathroom, (b) in the kitchen of an apartment.

The second method is the use of a supply-airflow window where forced ventilation is provided by a supply fan installed in the window as shown in Fig. 6.1a. The supply-airflow window produced positive indoor pressure. The indoor air was exhausted by the pressure difference between indoor and outdoor spaces. Figure 6.9 shows the predicted indoor CO_2 concentration over a one-week period in April. According to the numerical simulation, CO_2

concentration was predicted to be below 1000 ppm most of the times during that period. There are only two short periods of time when the CO_2 concentration in the living room stayed above 1000 ppm. In general, the ventilation provided by the supply-airflow window ventilation met the indoor fresh air requirement.
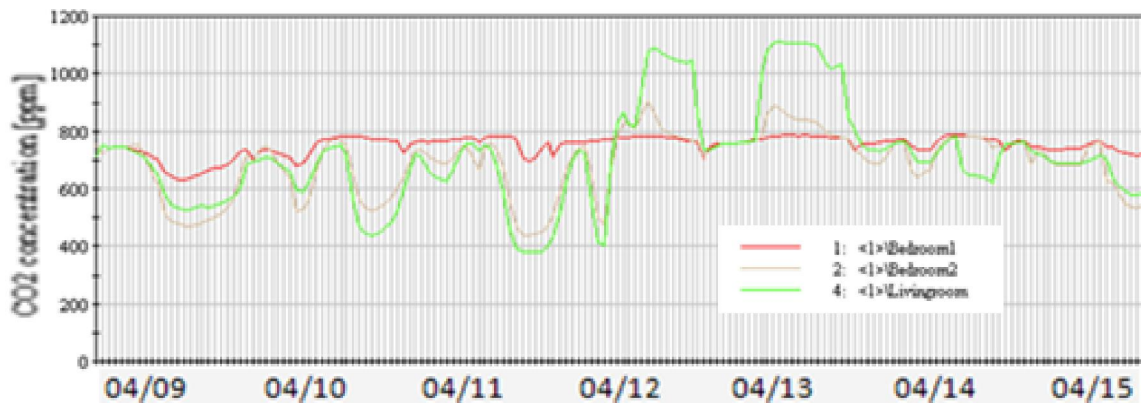
Fig. 6.9. Predicted indoor CO_2 concentration for a one-week period with the apartment with supply-airflow windows during the mild season.

The third method is based on an approach for providing a stable ventilation rate. This can be achieved by a dual-airflow window where a supply fan and an exhaust fan are installed in the window shown in Fig. 6.1b. Figure 6.10 shows the indoor CO_2 concentration for the one-week period in the mild season where dual-airflow windows were installed. The indoor CO_2 concentration was below 800 ppm for the entire period which met an acceptable level of IAQ. The reason for the low CO_2 concentration was that the supply air flow rate provided the required fresh air from outdoor space. The infiltration via the fans in the windows increased the total ventilation rate in addition to the previously existing paths in the buildings.
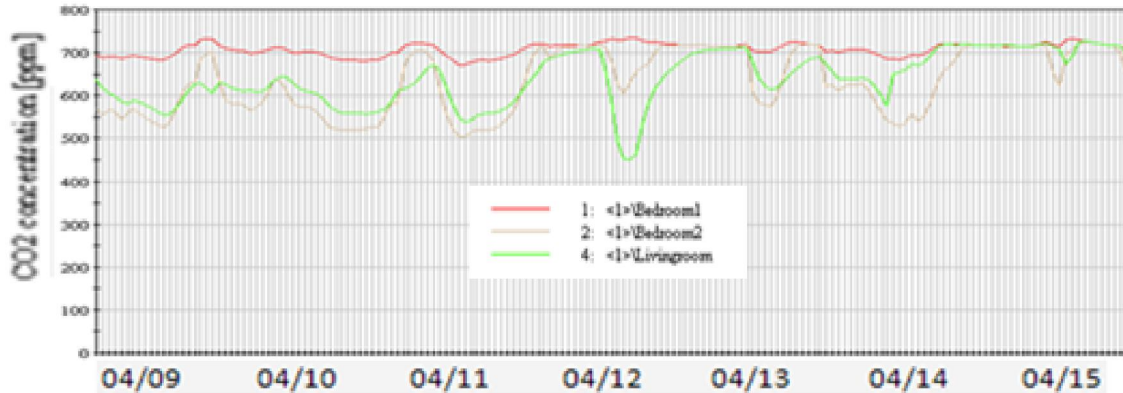
Fig. 6.10. Predicted indoor CO_2 concentration for a one-week period with the apartment with dual-airflow windows during the mild season.

6.6 Conclusions

This chapter presents a study of the IAQ in residential buildings under different ventilation approaches using CO_2 concentration as an evaluation criterion. By comparing the IAQ under natural ventilation, i.e., infiltration, in different climate zones, it was demonstrated that infiltration driven by thermal and wind pressure gradients are generally not sufficient to achieve an acceptable level of IAQ in the case of a tightly-sealed building envelop. It has also been shown that wind pressure gradients play a more important role than thermal gradients to affect indoor CO_2 concentration. It has been found that CO_2 concentration is higher in buildings with smaller indoor spaces. Buildings with larger indoor spaces are good for dispersion of the contaminant.

Since infiltration cannot reduce CO_2 concentration to below 1000 ppm, mechanical ventilation is required to meet the recommended standard for indoor air. Three types of mechanical ventilation were discussed in this chapter. The first type was exhaust fans in bathrooms and kitchens. The second type was supply-airflow windows, and, the third type was dual-airflow windows. The results indicated that exhaust-fan ventilation was affected by indoor

airflow paths. It could not maintain CO_2 concentrations below an acceptable level throughout the day. However, both supply-airflow windows and dual-airflow windows could be used for ventilation to maintain good IAQ.

References

M. V. Jokl, 1996. "Introduction of the decibel units to assess indoor air quality," *Proceedings of Buildings for Healthy Living*, Prague, 278-316.

M. V. Jokl, 1999. "Evaluation of indoor air quality using the decibel concept," *Journal of Environmental Health Research* **4**, 289-306.

M. V. Jokl, 2000. "Evaluation of indoor air quality using the decibel concept based on carbon dioxide and TVOC," *Building and Environment* **35**, 677-697.

Q. Luo, "Impacts of ventilation strategies on IAQ," *Refrigeration Air Conditioning & Electric* **2**, 14-18.

T. Leephakpreeda et al, 2001. "Occupancy-based control of indoor air ventilation: a theoretical and experimental study," *Science Asia* **27**, 279-284.

O. A. Seppanen, W. J. Fisk and M. J. Mendell, 1999. "Association of ventilation rates and CO2 concentrations with health and other responses in commercial and institutional buildings," *Indoor Air* **9**, 226–252.

J. Wei, J. Zhao, Q. Chen, 2010. "Energy performance of a dual airflow window under different climates," *Energy and Buildings* **42**, 111–122.

M. Zheng and J. Qi, 2002. "A new kind of energy saving window can be used in severe cold climate zone," *Building Energy Saving* **90**, 77-79.

7. Concluding remarks and suggestions for future work

It was known at the onset of this study that a traditional approach for sound insulation has been to seal building envelopes. However, this approach can lead to the degradation of IAQ because most buildings obtain their fresh air by natural ventilation, e.g., by infiltration or opening a window. It should also be noted that natural ventilation has been used increasingly in modern urbanized residential buildings to minimize the consumption of non-renewable energy. This approach is often used in "green" buildings. These designs rely on natural ventilation to control different kinds of environmental pollution. The potential benefits and the ventilation performance of these green features are not fully understood as yet.

To address the effects of these inter-related issues on sound insulation, two main themes were investigated separately in this initial study. The first theme was concerned with the evaluation of sound transmission through windows. The second theme specifically studied the assessments of energy efficiency and IAQ when airflow windows were used for sound insulation in residential buildings. Concluding remarks are offered at the end of chapters 2 to 6, in which the major accomplishments of each sub-tropic have been highlighted. These conclusions are not repeated here, but suggestions for future work are provided as follows.

To build on the achievements of the present study, it is recommended to develop an integrated model to assess energy efficiency, IAQ, and acoustic performance of noise insulation for buildings around airports. It is important to consolidate the existing FAA guidelines (the *Airport Improvement Program Handbook* and its associated advisory circulars) by providing additional information related to current best practices for improving IAQ and reducing energy use while maintaining sufficient noise level reductions for the comfort of residents and occupants of buildings near airports. A suite of effective models should be developed for assessing the

combined environmental performance of windows—acoustics, IAQ, and energy efficiency.

These future studies should also aim to examine the impact of energy-efficient windows and to compare them with conventional windows in terms of overall environmental performance for insulating building structures near airports. These proposed studies directly relate to several topics listed in the FAA's Research Results Digest 5 (RRD5), including (i) reducing energy consumption, and (ii) sustainability best practices. To make progress in this direction, the following research tasks may be considered for their implementations:

Task 1 Conduct full-scale field experiments to examine the environmental performance of different types of windows including energy-efficient types (e.g., dual-airflow windows). Measurements of acoustic performance, IAQ, and energy efficiency were conducted during two-week periods in the summer and winter at one or more geographical locations. These experimental results formed a database that was used in Task 3 for model validation.

Task 2 Develop integrated models/tools to analyze a few typical residential buildings near airports (with and without energy-efficient windows) in different climate regions. The integrated model should identify the combined problems of acoustics, IAQ, and energy efficiency in residential buildings in the proximity of airport. The experimental data obtained in Task 2 can be used to validate the integrated model. A successful integrated model can be used as a numerical tool for design engineers or architects in future FAA-funded noise insulation projects.

Task 3 Examine the current best practices of IAQ and energy efficiency of residential buildings in conjunction with the guidelines for sound insulation for FAA-funded noise insulation projects. Conduct cost-benefit analysis of various methods (e.g., change from mechanical to natural ventilation in buildings) for improving IAQ and energy efficiency in building structures while

149

maintaining specified noise level reduction. Based on these studies, recommend additional guidelines to improve IAQ and energy efficiency for FAA program requirements.

Task 4 In addition to the three tasks listed above, an integrated analysis of windows insulation should be conducted. A list of fundamental parameters, which are needed for future study, is provided at Appendix C for information.

Appendix A: A two-dimensional model for heat transfer used in EnergyPlus

Nomenclature

A	Window area	h	Convective heat transfer coefficient
C_p	The specific heat of air	K_j	The number of levels for each variable
D_j	The extreme difference in column j	Q	Window heating/ cooling load
E	Radiation intensity	T	temperature
ER	Relative energy saving of window load	U	The overall window heat transfer coefficient
V	The window ventilation rate	v	Window speed in the airflow window
ε	infrared emissivity for each glass layer	ρ	Air density
λ	conductive heat transfer coefficient		

Subscripts

conventional	Conventional window	*window*	Window without ventilation
dual-airflow	Dual-airflow window	*ventilation*	Window with ventilation
e	Exhausted airflow	*1*	The exterior side of the exterior glass pane
in	Indoor space	*2*	The interior side of the exterior glass pane
j	The number j zone in the vertical direction of the dual-airflow window	*3*	The exterior side of the middle glass pane
out	Outdoor environment	*4*	The interior side of the middle glass pane
s	Supplied airflow	*5*	The exterior side of the interior glass pane
solar	Solar radiation	*6*	The interior side of the interior glass pane

A.1 Conservation of heat energy in each section

The heat and mass transfer through a building exterior, e.g., windows, walls, and roofs, are calculated using the computer program, EnergyPlus. Different layers of a window are solved simultaneously at different nodal points. The program assumes the temperature along the entire length of a window to be uniform, as shown in the three-pane window in Fig. A.1a. In this example, the three-pane window has six nodes, which have six interdependent temperatures.

In the present study, a direct application of EnergyPlus without modifications for the vertical change in temperature was inappropriate because air necessarily flows vertically through the two cavities of a dual-airflow window. Hence, the temperature of a glass pane in the vertical direction is not uniform. The air temperature change in the cavities also depends on the vertical length of the window. Hence, it is proposed to divide the window into n equal sections along its vertical length as shown in Fig. A.1b.
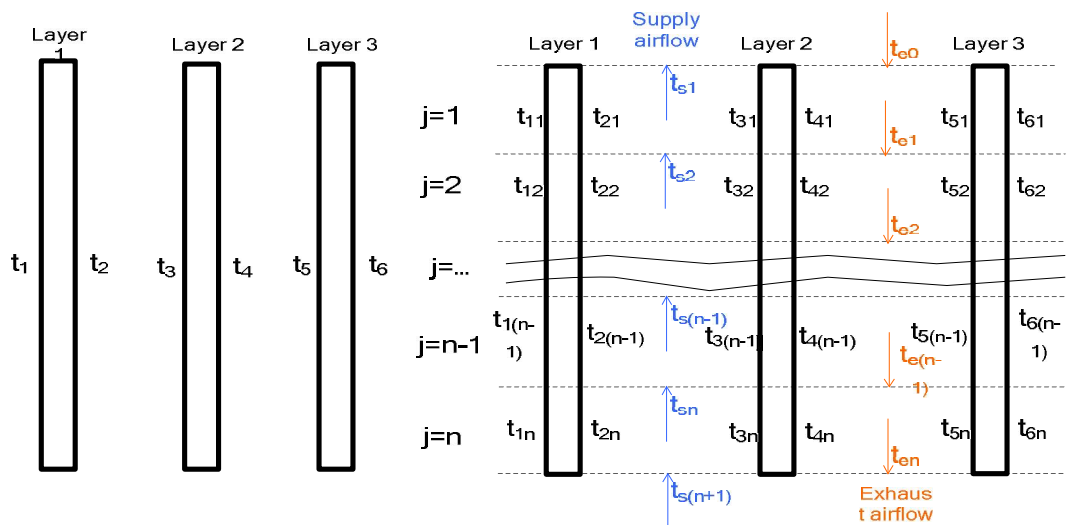
(a) A conventional three-pane window   (b) A dual-airflow window
Fig. A.1. Schematic of window network models for EnergyPlus

More specifically, the present modification of the EnergyPlus program was implemented by a new network model. The model was based on the energy balance for each individual section.

The model considers the convection, conduction, and solar radiation through the glass panes. It also takes into account the radiation exchange between the glass panes, the interior spaces, and the exterior spaces as shown in Fig. A.1a. The existing equations in EnergyPlus can be used in each section separately. The energy and mass balance between consecutive sections were only considered in the transverse direction between the two cavities. Since only a two-dimensional model is considered, the heat and mass transfer in the horizontal direction are ignored. Furthermore, the heat transfer in the vertical direction along the glass was neglected in the present study. Figure A.2b shows the parameters used in this study. A list symbols is given at the beginning of Appendix A.
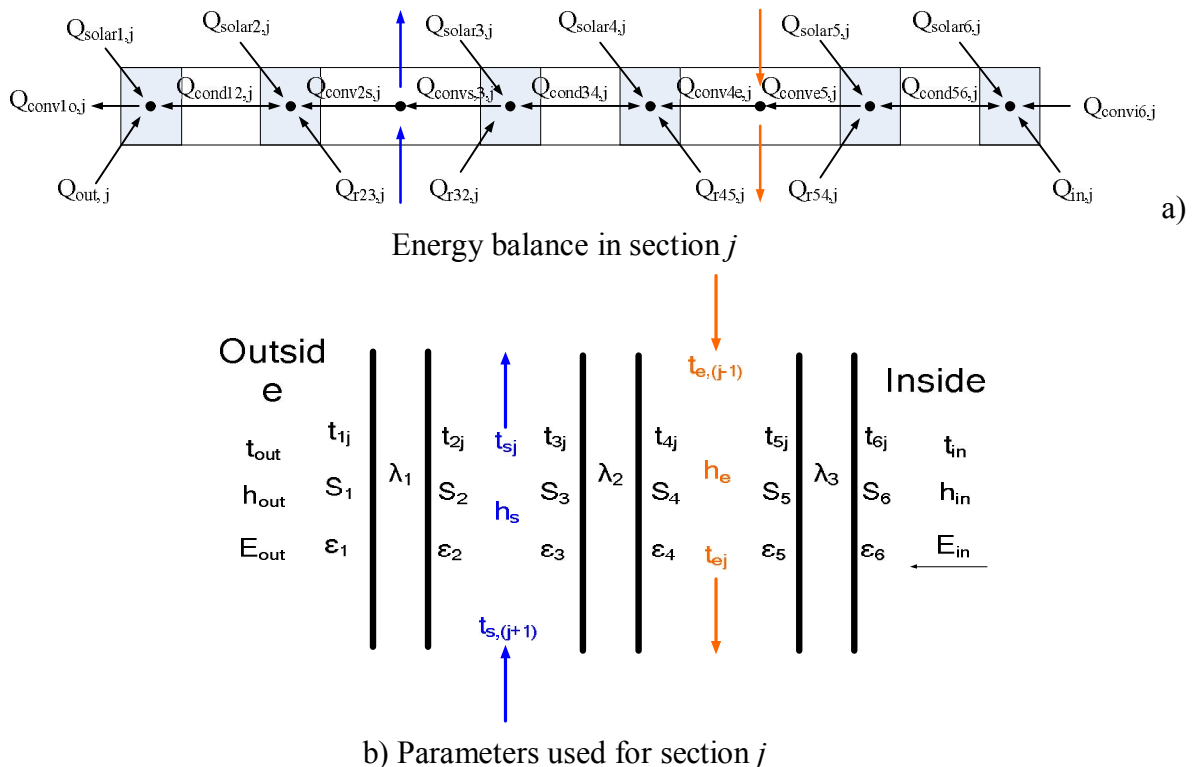
Fig. A.2. Schematic of heat flow through section j of a dual-airflow window

Fig. A.2a shows the dual-airflow window which has eight nodes in a typical section. For node 1, the energy balance equation is given as

$$E_{out}\varepsilon_1 - \varepsilon_1\sigma T_{1j}{}^4 + \lambda_1(T_{2j}-T_{1j})\frac{H}{n} + h_{out}(T_{1j}-T_{out}) + Q_{solar1} = 0 \tag{A.1}$$

Similarly, the energy balance equation for node 2 can be written as

$$\lambda_1(T_{1j}-T_{2j})\frac{H}{n} + h_s(T_{sj}-T_{2j}) + \sigma\frac{\varepsilon_2\varepsilon_3}{1-(1-\varepsilon_2)(1-\varepsilon_3)}\left(T_{3j}{}^4 - T_{2j}{}^4\right) + Q_{solar2} = 0\,. \tag{A.2}$$

For the air layer in the outer cavity (node 3), its energy balance equation can be verified to give

$$h_s(T_{sj}-T_{2j}) + h_s(T_{sj}-T_{3j}) + \rho v_s c_p(T_{sj}-T_{s,(j+1)}) = 0\,. \tag{A.3}$$

The energy equations for nodes 4 and 5, for the second glass pane, can be determined in a similar manner. They are given, respectively, as

$$h_s(T_{3j}-T_{sj}) + \lambda_2(T_{4j}-T_{3j})\frac{H}{n} + \sigma\frac{\varepsilon_2\varepsilon_3}{1-(1-\varepsilon_2)(1-\varepsilon_3)}\left(T_{2j}{}^4 - T_{3j}{}^4\right) + Q_{solar3} = 0 \tag{A.4}$$

and

$$\lambda_2(T_{3j}-T_{4j})\frac{H}{n} + h_e(T_{ej}-T_{4j}) + \sigma\frac{\varepsilon_4\varepsilon_5}{1-(1-\varepsilon_4)(1-\varepsilon_5)}\left(T_{5j}{}^4 - T_{4j}{}^4\right) + Q_{solar4} = 0 \tag{A.5}$$

The energy balance equations for the inner cavity (node 6) can be determined analogously to yield:

$$h_e(T_{5j}-T_{ej}) + \lambda_3(T_{6j}-T_{5j})\frac{H}{n} + \sigma\frac{\varepsilon_4\varepsilon_5}{1-(1-\varepsilon_4)(1-\varepsilon_5)}\left(T_{4j}{}^4 - T_{5j}{}^4\right) + Q_{solar5} = 0 \tag{A.6}$$

Finally, the energy balance equations for the third glass pane (nodes 7 and 8) can be determined as

$$h_e(T_{ej} - T_{4j}) + h_e(T_{ej} - T_{5j}) + \rho v_e c_p(T_{ej} - T_{e,(j-1)}) = 0 \qquad \text{(A.7)}$$

$$E_{in}\varepsilon_6 - \varepsilon_6 \sigma t_{6j}^{\ 4} + \lambda(T_{5j} - T_{6j})\frac{H}{n} + h_{in}(T_{in} - T_{6j}) + Q_{solar6} = 0 \qquad \text{(A.8)}$$
.

These 8 equations, (A.1) to (A.8), are written in terms of eight unknown nodal temperatures. Many of the parameters used in the equations (as shown in Fig. A.2b) are dependent on the temperature. Furthermore, the nodal temperatures are correlated with the temperature of the air along the vertical direction of the cavity. Hence, Eqs. (A.1–8) comprise a set of 8 non-linear simultaneous equations that can be solved by a straightforward iterative scheme between 2 consecutive sections.

Appendix B: Numerical simulations for the use of dual-airflow windows in other cities

This Appendix provides the energy efficiency of dual-airflow window in climate zones 2 to 6.

(1) Energy efficiency of dual-airflow window in Helena (Climate zone 6)
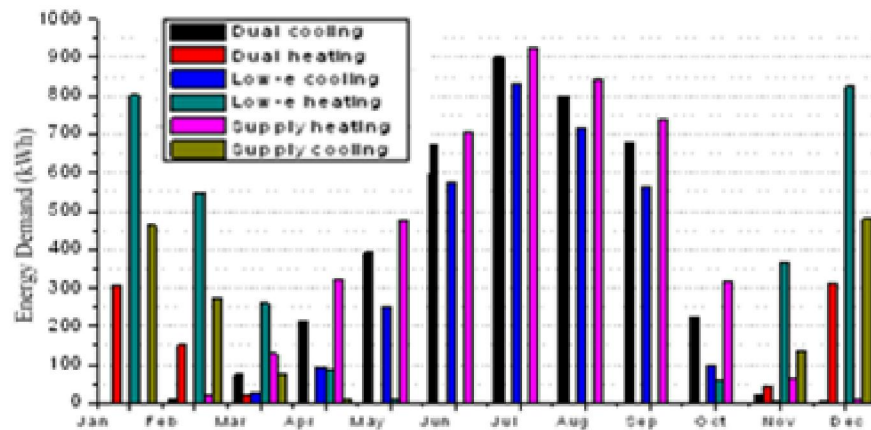
a)   Apartment
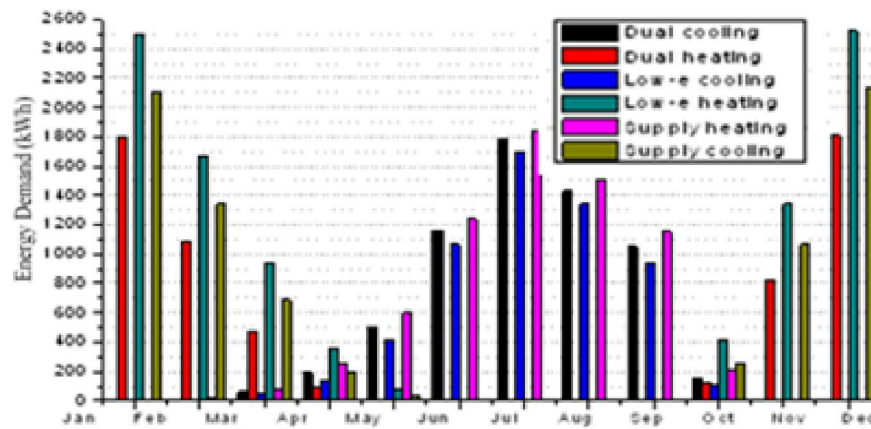
b)   Detached house

Fig. B.1. Monthly energy demand with the three types of windows in Helena
(a) an apartment, (b) a detached house.

Figure B.1 shows the monthly energy demand for an apartment and a detached house in Helena with three different types of windows. It illustrates that there is a demand for heating energy only from November to April. There is a demand for cooling energy for the entire year

except in January.

In the heating season, dual-airflow windows require the least heating energy, while conventional windows require the most. This characteristic is similar to the building energy efficiency observed in Duluth. The energy savings from the dual-airflow windows are because of their ability to recover heat. In the cooling season, the energy demand from the supply-airflow window is the highest and that from the conventional window is the lowest. This demonstrates that the energy recycled by the two airflow windows is smaller than the gain in solar heat by these two types of windows.

For the two types of buildings, the monthly energy demand is similar with that shown for Duluth. This is because Duluth and Helena are located along almost the same latitude, with comparable weather conditions. However, the ratio of the annual heating energy to the annual cooling energy is not the same. This is largely because of the difference in longitudes between these two cities, as can be seen in the climate map in Fig. 5.7.

In summary, heating energy savings from the dual-airflow window in the apartment were 71.9% when compared with the conventional window and 42.6% when compared with the supply-airflow window. The respective savings in the detached house were 36.7% and 20.5%. In the cooling season, the dual-airflow windows demanded more energy than conventional windows. Nevertheless, their use led to more savings in cooling energy than when supply-airflow windows were used.

(2) Energy efficiency of dual-airflow windows in Chicago (climate zone 5)

For Chicago, the energy efficiency of buildings with three different types of windows is summarized in Fig. B.2. The numerical results suggested that the apartment had cooling energy demand for the entire 12 month period and a higher demand for cooling energy between May

and October. From November to April, there is a heating energy demand in the apartment. During the periods having both heating and cooling loads, analyses show that outdoor temperature and solar radiation cause higher indoor temperatures during the daytime. Conversely, at night the outdoor temperature is low, and no cooling energy is needed. According to the numerical simulations, there is generally no cooling energy demand in the detached house from November to April in Chicago.

a)   Apartment
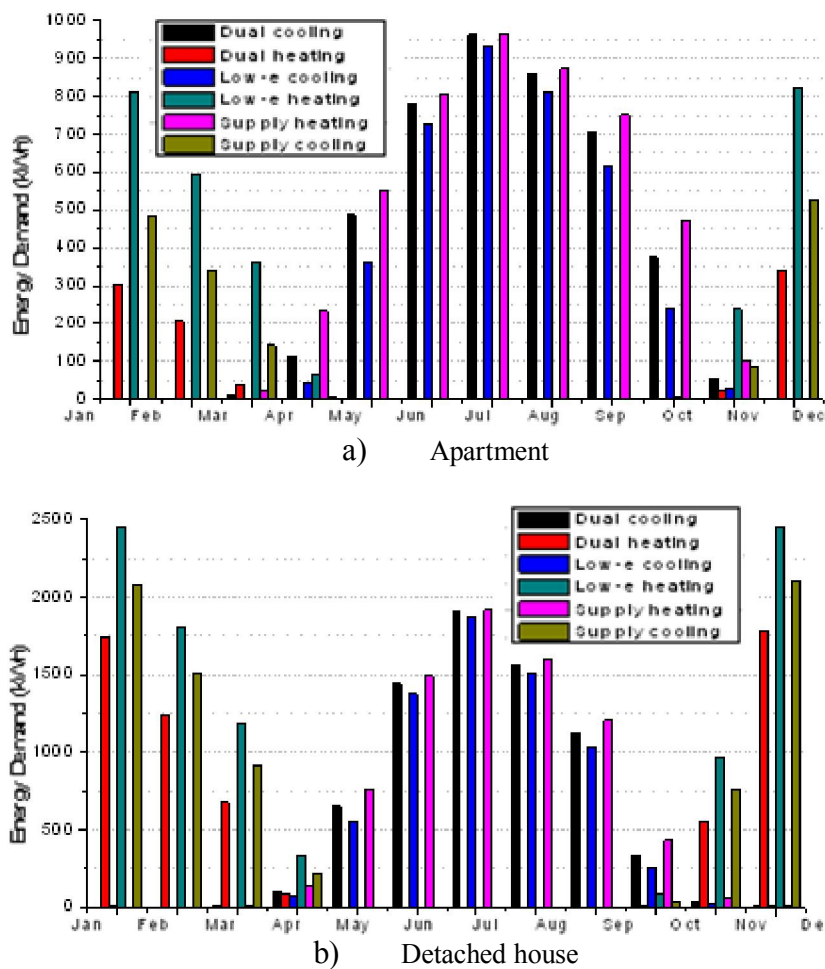
b)   Detached house

Fig. B.2 Monthly energy demand with the three types of windows in Chicago
(a) an apartment, (b) a detached house.

The difference between the energy efficiency in the apartment and in the house

demonstrates that the cooling energy demand in the apartment is caused by solar heat gain through the windows. In the detached house, the higher heat loss through the exterior walls can effectively reduce the solar heat gain through the windows. It is possible to suggest that for those cities situated in climate zone 5, a decrement in the area ratio of windows to walls can lead to a significant savings in the cooling energy demand.

In summary, the heating energy savings from dual-airflow windows, as opposed to conventional windows and supply-airflow windows, are 68.6% and 42.4%, respectively, in the heating season, for the apartment. In the detached house, the respective savings reduce to 34.3% and 19.9%, respectively. However, conventional windows perform better than the airflow windows in the cooling season.

(3) Energy efficiency of dual-airflow window in Salem (Climate zone 4)

Figure B.3 shows the monthly energy demand for the buildings with the three types of windows in Salem. For these two types of buildings, cooling energy demand played a more important part in the consumption of energy for the entire year. There was cooling energy demand for the entire 12 month period in the apartment, but there was no cooling energy demand for the detached house in November and December. The difference was because of the fact that larger exterior wall areas facilitate heat transfer between indoor and outdoor spaces. In the detached house, the heat loss through the walls was more than the heat gain through the windows in these two months.

Buildings with conventional windows consumed less cooling energy in the cooling season, and the use of heating energy was limited in the heating season. Consequently, the energy conservation ability of the dual-airflow window was smaller than that in climate zones 5, 6, and

7. For buildings in Salem, the heating energy savings in the apartment from dual-airflow windows, compared with conventional windows and supply-airflow windows, were 86% and 26%, respectively. For the detached house, the relative savings were lower at 40.8% and 23.9%, respectively. It is important to point out that the estimated figures indicate high relative energy savings, but the actual annual energy savings were less attractive because of the small heating energy demand in Salem.

a)   Apartment
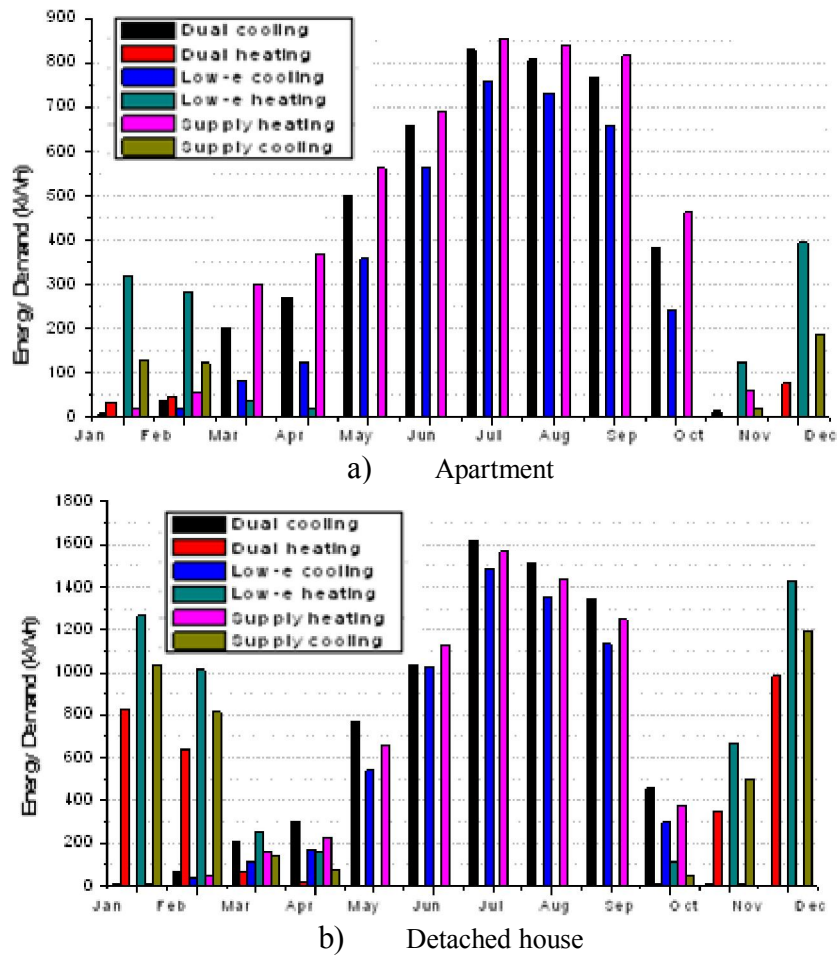
b)   Detached house
Fig. B.3. Monthly energy demand with the three types of windows in Salem
(a) an apartment, (b) a detached house.

(4) Energy efficiency of dual-airflow window in San Francisco (Climate zone 3)

Figure B.4 depicts the energy efficiency of buildings with three different types of windows in

San Francisco. Only the detached house required a small amount of heating energy in December

and January. The chart shows that conventional windows had the lowest cooling energy demand.

Therefore, the dual-airflow window is not recommended for use in this climate zone.

a) Apartment
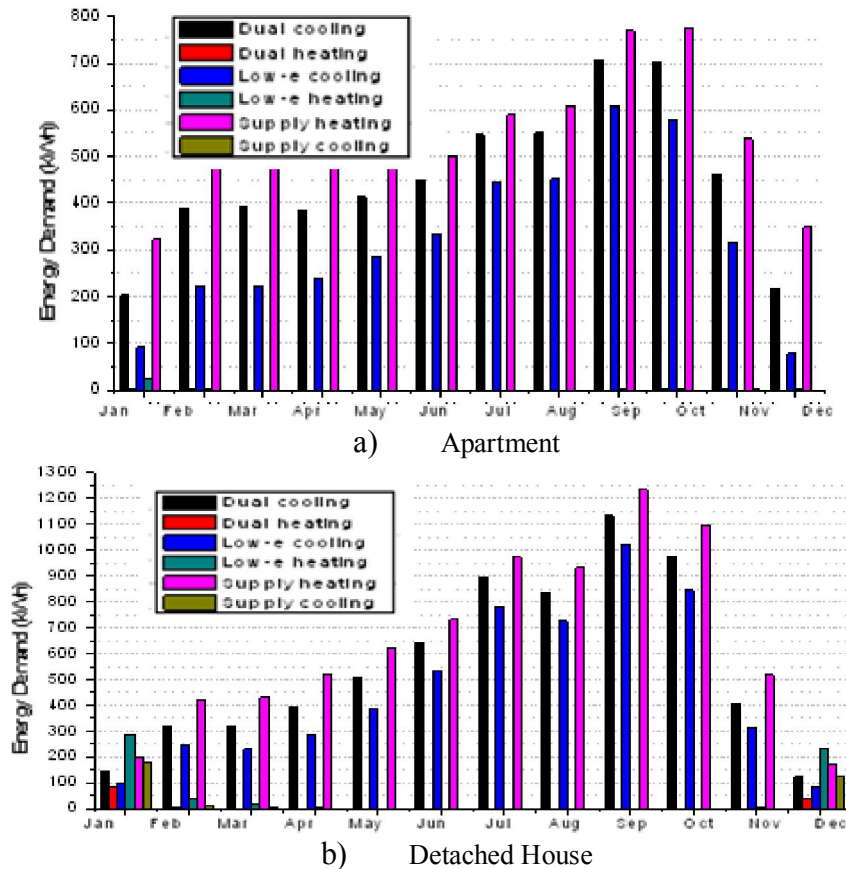
b) Detached House

Fig. B.4. Monthly energy demand with the three types of windows in San Francisco
(a) an apartment, (b) a detached house.

(5) Energy efficiency of dual-airflow window in Phoenix (Climate zone 2)

Figure B.5 shows the monthly energy demand for the buildings with the three types of windows

in Phoenix. The simulated results indicated that the building energy efficiency in Phoenix is very

similar to that in San Francisco. There was no heating energy requirement during the entire year

for the apartment or the detached house.

From May to September, the buildings with the dual-airflow windows used the least energy.

From October to April, the buildings with conventional windows used the least energy. For the

entire year, the energy savings on account of the dual-airflow window were very small, and

hence, it is not recommended for use in this climate zone.

a)   Apartment
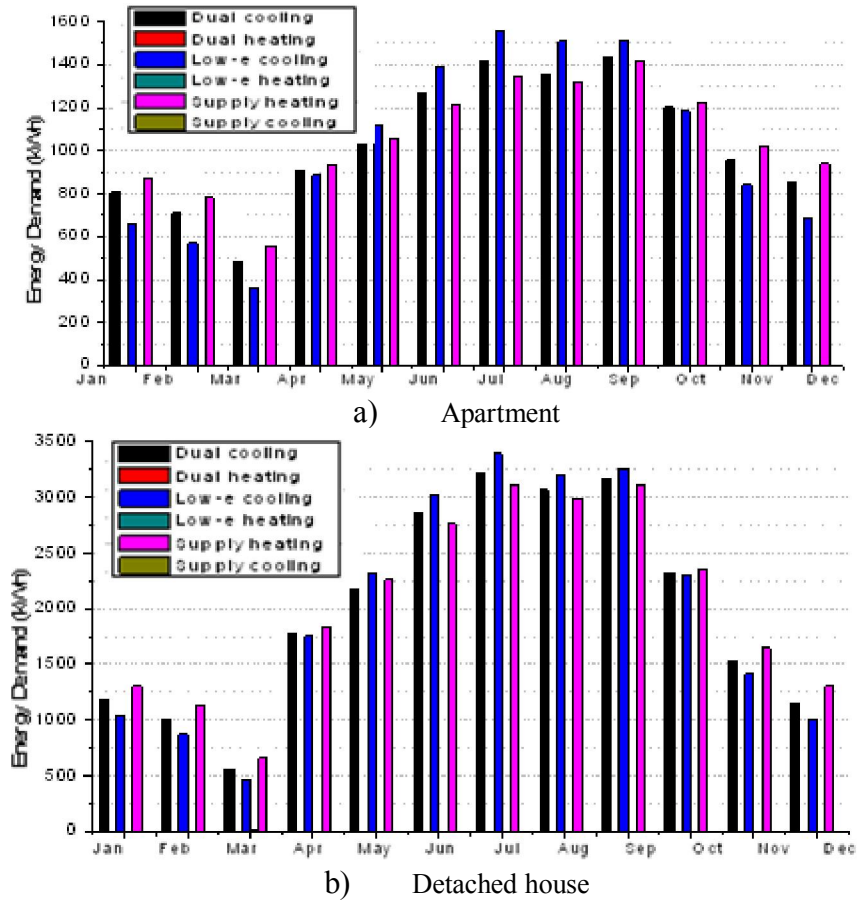
b)   Detached house

Fig. B.5. Monthly energy demand with the three types of windows in Phoenix
(a) an apartment, (b) a detached house.

Appendix C: Integrated analysis of windows in sound Insulation, energy efficiency and indoor Air Quality

A comprehensive literature is conducted to examine the impact of window/ventilation systems on the indoor environments of building. Typically, the indoor environment includes the assesmsent of acoustic comfort, thermal comfort, indoor air quality, energy utlilization and impacts on outdoor environments. To enable an integrated analysis of windows used in sound insulation, a list of physical parameters is identified for the study of

(a) environmental factors for assessing windows,

(b) the energy performance of ventilation systems for building, and

(c) objective assessments of ventilation systems including windows.

(a) Environmental factors for combined assessment of windows[1-9]

1. Sound reduction Index – currently used for assessing the acoustic performance for sound insulation.

2. Indoor Background noise level

3. Reverberant times – speech intelligibility

4. Noise isolation

5. Number of air change per hour

6. Fiber concentration

7. Indoor dust particle concentration/ Ultra fine particulate matter concentration (UPC)

8. Volatile organic compound

9. concentration of CO_2

10. Relative humidity

11. Air temperature

(b) Energy performance of ventilation systems[10,11]

1. Outdoor air supply rate

2. Window cavity width

3. Window width

4. Window height

5. Thermal conductivity

6. Glazing thickness

7. Solar heat gain coefficient of window glass pane

8. Emissivity

9. thermal conductivity of window frame

10. window frame width

11. Window orientation

12. Shading coefficient

13. Window blinds position

(c) Ventilation systems including windows[12-15]

1. concentration of pollutants (e.g. HCHO and TVOC)

2. Emission of CO_2

3. Energy consumption

4. Increase in indoor dust particle concentration

5. Increase in indoor background noise level

In addition to the integrated analysis, a separate study should also be focused on the assessment of the acoustic performance of windows.[16-24] A list of bibliography is provided as follows for future references.

Bibliography

1. M.H.F. De Salisa, D.J. Oldhama, S. Sharplesb, 2002. "Noise control strategies for naturally ventilated buildings," Building and Environment **37**, 471 – 484.

2. M. N. Halgamuge, T. K. Chan, and P. Mendis, 2009. "Ventilation Efficiency and Carbon Dioxide (CO2) Concentration," PIERS ONLINE **5**, NO. 7..

3. H. A. Aglan, 2003. "Predictive model for CO2 generation and decay in building envelopes," Journal of Applied Physics, **93**(2).

4. P.S. Hui, L.T. Wong, K.W. Mui , 2008. "Using carbon dioxide concentration to assess indoor air quality in offices," Indoor Built Environment **17,** 213–219.

5. K.C. Noh, and J. Hwang, 2010. "The Effect of Ventilation Rate and Filter Performance on Indoor Particle Concentration and Fan Power Consumption in a Residential Housing Unit," Indoor Built Environment **19**, 444–452

6. J. Hummelgaard, P. Juhl, K.O. Sæbjo, G. Clausen, J. Toftum, and G. Langkilde, 200t. "Indoor air quality and occupant satisfaction in five mechanically and four naturally ventilated open-plan office buildings," Building and Environment **42,** 4051-4058.

7. S. Cho, K. Kim, M. Park, K. Lee and J. Choi, 2009. "Ventilation Performance by the Concentration Change of HCHO and TVOC with Three Models of Two Ventilation Systems and One Natural Condition," Journal of Asian Architecture and Building Engineering, May 2009.

8. T. Paul, D. Sree and H. Aglan, 2010. "Effect of mechanically induced ventilation on the indoor air quality of building envelopes," Energy and Buildings **42**, 326–332

9. M. Hodgson, 2009. "Occupant Satisfaction with the Acoustical Environment: 'Green' Office buildings before and after treatment," PLEA2009 - 26th Conference on Passive and Low Energy Architecture, Quebec City, Canada, 22-24 June 2009.

10. J. Wei, J. Zhao and Q. Chen, 2010. "Energy performance of a dual airflow window under different climates," Energy and Buildings **42**, 111–122.

11. J. Wei, J. Zhao, Q. Chen, 2010. "Optimal design for a dual-airflow window for different climate regions in China," Energy and Buildings **42**, 2200-2205.

12. A.C.K. Lai, K.W. Mui, L.T. Wong, and L.Y. Law, 2009. "An evaluation model for indoor environmental quality (IEQ) acceptance in residential buildings," Energy and Buildings **41**, 930–936.

13. K.W. Mui, L.T. Wong, and P.S. Hui, 2009. "Indoor Environmental Quality Benchmarks for Air-conditioned Offices in the Subtropics," Indoor Built Environment **18,** 123–129

14. L.T. Wong , K.W. Mui , and P.S. Hui, 2009. "Evaluation on screening strategies for indoor air quality assessments in air-conditioned offices," Building Services Engineering Res. Technology **30,** 203–212.

15. T. Paul, D. Sree, and H. Aglan, 2010. "Effect of mechanically induced ventilation on the indoor air quality of building envelopes," Energy and Buildings **42**, 326–332.

16. J. Kang and M. W. Brocklesby, 2003. "Application of micro-perforated absorbers in developing novel window systems for optimum acoustic, ventilation and daylighting performance," Proceedings of the Institute of Acoustics (IOA) (UK) 25, 47-54.

17. J. Kang and M. W. Brocklesby, 2004. "Feasibility of applying micro-perforated absorbers in

acoustic window systems," Applied Acoustics **66**, 669-689.

18. J. Kang and M. W. Brocklesby, 2004. "Design of acoustic windows with micro-perforated absorbers," Proceedings of the 18th International Conference on Acoustics (ICA), 1223-1224.

19. J. Kang, M. W. Brocklesby, Z. Li and D. J. Oldham, 2005. "An acoustic window for sustainable buildings," The 149th meeting of the Acoustical Society of America (Vancouver, Canada, 2005).

20. J. Kang and Z. Li, 2007. "Numerical simulation of an acoustic window system using finite element method," Acta Acustica **93**, 152-163.

21. H. Huang, and J Kang, 2009. "Numerical simulation of the sound field inside a natural ventilation window," Inter-Noise 2009.

22. F. Asdrubali and C. Buratti, 2005. "Sound intensity investigation of the acoustics performances of high insulation ventilating windows integrated with rolling shutter boxes", Applied Acoustics **66**, 1072-1085.

23. F. Asdrubali, 2007. "Acoustic performances of high insulation ventilating windows integrated with rolling shutter boxes", Noise & Vibration Worldwide.

24. César Díaz , and A. Pedrero, 2009. "An experimental study on the effect of rolling shutters and shutter boxes on the airborne sound insulation of windows," Applied Acoustics **70**, 369–377.